NORTHWESTERN UNIVERSITY

Tribological Interfaces Studied by an Analytical Dislocation Model and
In-situ Transmission Electron Microscopy

A DISSERTATION

SUBMITTED TO THE GRADUATE SCHOOL

IN PARTIAL FULFILLMENT OF THE REQUIREMENTS

for the degree

DOCTOR OF PHILOSOPHY

Field of Materials Science and Engineering

By

Arno Peter Merkle

EVANSTON, ILLINOIS

June 2007

ABSTRACT

Tribological Interfaces Studied by an Analytical Dislocation Model and *In-situ*

Transmission Electron Microscopy

Arno Peter Merkle

Fundamental investigations on the origins of friction at the nanoscale were carried out using both theoretical and experimental approaches. A model was developed that analytically solves for friction by the motion of dislocations at atomically flat crystalline interfaces. It combines known concepts from dislocation drag, grain boundary theory, and contact mechanics into a single model which accurately predicts a wide range of friction phenomena, including static and kinetic friction, friction anisotropy, transfer layers and velocity dependence. In addition, values for friction coefficients calculated by inputting only basic materials constants yield reasonable agreement with comparable ultrahigh vacuum friction results.

To test the consequences of the theory, friction anisotropy measurements between single crystal NaCl and $SrTiO_3$ surfaces by pin-on-disk and nanoindentation techniques were conducted, and shown to influence friction by an upper bound of ten percent fluctuation in ambient conditions.

Lastly, *in-situ* transmission electron microscopy (TEM) techniques were employed to overcome the classic "buried interface" problem in tribological research. Direct observations of the sliding behavior between surfaces were carried out in real time by imaging and spectroscopy techniques within the TEM. Unambiguous structure-friction relationships were identified for graphite, gold and diamond-like carbon, by observing dynamic interactions between the scanning probe and samples. Direct evidence is presented for graphitic wear by flaking and transfer layer formation as well as liquid-like behavior of gold at moderate temperatures, which has implications for metallic lubricants. Diamond-like amorphous carbon films were shown to form a graphitized surface layer induced by sliding. The approaches taken in these *in-situ* friction experiments mark the beginning of an era of new direct characterization capabilities in fundamental tribological research.

Approved by

————————————————-

Professor Laurence D. Marks

Department of Materials Science and Engineering

Northwestern University, Evanston, IL 60208, USA

Acknowledgements

There are several people that have made this research possible. First, I would like to thank my thesis advisor, Laurie Marks, for daring to pursue challenging "bleeding edge" research, for having the patience to see projects through to their conclusions, for never settling or being satisfied, and for teaching me that research and the acquisition of knowledge is an ever-evolving organism, with no definite beginning or end. I would like to thank the National Science Foundation for supporting my work through the IGERT program. I also thank my IGERT co-advisor, Prof. Q. Jane Wang, for putting my research in perspective with "real" tribologists. I am indebted to my defense committee, Prof. Michael Graham, Prof. Kenneth Shull, and Prof. Eric Stach for providing insights and showing genuine interest towards my work. I thank the AFOSR for providing the funds for the TEM holder.

A significant amount of my work was performed at the Electron Microscopy Center at Argonne National Laboratory. I am especially grateful for the scientific and technical assistance from the staff, in particular Drs. Russ Cook, Bernd Kabius, and Nestor Zaluzec. I would like to also acknowledge Drs. Osman Eryilmaz, Ali Erdemir, and Jackie Johnson for providing the diamond-like carbon samples (Chapter 6), and for stimulating discussions. Many thanks to Nanofactory Instruments for manufacturing and supporting the TEM holder, and to Hysitron Inc. for giving me the opportunity to perform the friction anisotropy experiments in their laboratory.

Most of my graduate career was spent with members (past and present) of the Marks Group: Natasha, Edy, Arun, Yingmin, Chris, Ann, Courtney, Brian, Robin, the three Jims (sorry guys), and Paramita; to them I owe much gratitude for teaching me, challenging me, and adding another dimension to laboratory life. I also want to thank Braun GmbH for manufacturing the coffee maker in our office which served as the most cost-effective source of inspiration (Take note, funding agencies).

To my Northwestern friends and peers, too many to list: thanks for the memorable experiences and lasting friendships. I wish to thank my friends outside of Northwestern: Tim, Jason, Tom, Ben, Tyson, Colin, Kinsey, the Kobayashi String Quartet and countless others, for pulling me away from the books and the lab for much-needed recharging, and reminding me that I do have a cello that needs attention from time to time.

I want to thank my parents for their endless support; my father for inspiring me to become a scientist, and for supplying both samples and his "back seat driver" skills on the microscope at Argonne, and my mother for keeping my father not too occupied with my research and for being as supportive as any son could wish for. Thank you, Bodo, for countering my troubles in the lab with complaints from the business world. And, to all of my family in Germany: Vielen herzlichen Dank. I want to especially thank my new family in Argentina - Amalia, Polo, Ivana and Marcela - for treating me like their own son long before I became their only son.

And finally, I want to express my deepest gratitude to my wife, Mariana, for as many reasons as there are words in this thesis. You inspire me every day. Te amo mucho.

Table of Contents

List of Tables

List of Figures

CHAPTER 1

Introduction

1.1. Why Tribology?

The phenomena associated with surfaces in contact and relative motion form the basis for tribological research. The importance of controlling friction and wear through structure, materials selection and lubrication was realized since the time of the construction of the pyramids (Figure 1.1). It was first formulated and documented scientifically by Leonardo Da Vinci 200 years before Newton defined the laws of force and mechanics, making tribology one of the oldest fields of scientific study. Despite this, only a fragmented understanding of the fundamental mechanisms of friction exists.

In the modern world, energy losses by friction have been estimated [5, 6] to represent an economic cost of $100 billion dollars annually in the U.S. alone, and up to 4% of developed countries GDPs. Up to $21,000,000,000 (1981 U.S. dollars) could realistically be saved through efficiency improvements resulting from tribological research [6]. A cost-benefit ratio for this type of research has been estimated to be 1:50 [7]. This massive economic driving force plays a large role in the development of alternative fuels and energies, including the design of new materials with favorable friction and wear properties. There is a significant environmental component as well: highly toxic lubricants are often used for heavy machining. For this reason, safer solid lubricant coatings are being developed. Controlling friction on an industrial scale has traditionally relied on
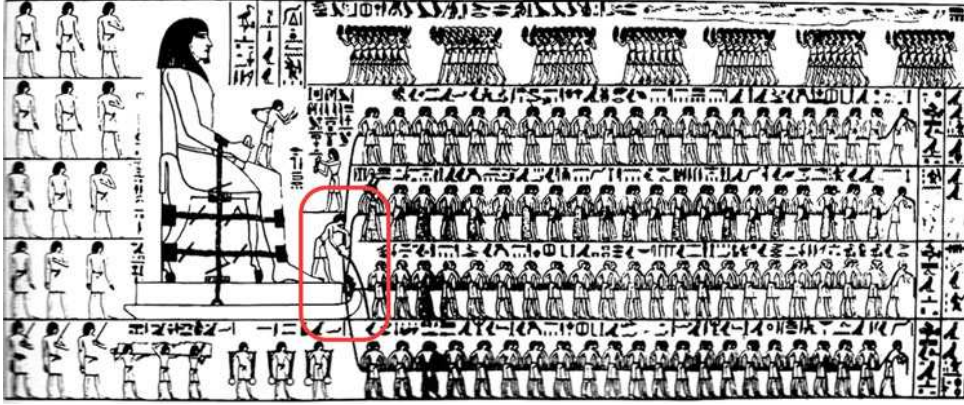
Figure 1.1. Ancient tribologist (from Ref. [1])

trial and error research. Moving away from this inefficient process, the ambitious goals of tribological research now aim to create computational models that quickly and accurately predict friction properties from starting contact conditions and basic principals of materials deformation. The fabrication of new materials with more favorable mechanical and tribological properties, particularly in the field of protective coatings, remains an active field of research.

The limits of improving tribological performance have long surpassed mechanical design and have entered an era of materials limitations, where structure, properties and processing of materials, understanding their limitations and exploiting their properties has become the primary focus. For this reason, tribology research centers worldwide have branched out from mechanical engineering departments towards their physics, materials science and chemistry colleagues.

1.2. Macroscopic Laws of Friction

The laws of friction dating back to DaVinci still see use today in basic discussions of the phenomena. Unfortunately, none of the laws attributed to Da Vinci, Amontons and

Coulomb are universally valid. In fact, nothing fundamental about the dissipative processes associated with friction may be derived from these simple expressions. Nonetheless, they are listed here for perspective:

(1) $F = \mu F_N$

(2) $F \not\propto A$

(3) $F \not\propto V$

where F is the friction force, μ the friction coefficient, F_N the normal load, A the contact area, and V the sliding velocity.

The first two macroscopic laws of friction were discovered by Da Vinci and rediscovered and published centuries later by Amontons. The first states that when a body is set in motion along a contacting surface, the dissipative friction force (antiparallel to the direction of motion) will be directly proportional to the normal force, related by a constant known as the coefficient of friction, μ. This quantity is determined by materials properties of the contacting surfaces as well as environmental conditions (humidity) and surface roughness. The second macroscopic law of friction states that friction is independent of the apparent area of contact. For example, a book sliding across a table on its flat side experiences the same friction force as if it were sliding on the binding side. This is a very non-intuitive concept, and was not formally challenged until 1950 by Bowden and Tabor, with the realization that real areas of contact consist of small touching asperities and account for a small fraction of the apparent contact area. Charles August Coulomb contributed the third macroscopic friction law, finding that friction is independent of sliding speed. Although these principals generally hold for most macroscopic contact conditions,

no fundamental theory of the origins of frictional energy dissipation can satisfactorily account for the complexity of interactions involved.

1.3. Nanotribology

Tribology is an inherently complex field of study. Sliding interfaces are affected by an enormous number of factors, the most basic of which are: load, atmospheric environment, chemical composition, crystalline structure, temperature, sliding speed, third bodies, and roughness. Each of these factors can be quite significant for macroscopic friction force measurements, but taking the analysis to the nanoscale serves to magnify their consideration. Why study the nanoscale? Because it is on the nanoscale that solid-solid interfaces form their most fundamental units of contact (at asperities). Understanding the way individual asperities interact may then lead to a richer understanding of frictional dissipation.

The most fundamental unit of solid-solid contact is the single asperity, with a typical contact area of square nanometers. It has become abundantly clear through decades of research that macroscopic tribological properties are greatly affected by the local chemical and environmental conditions near single asperity contacts. Dramatic changes in the way materials lubricate or wear depend on nanoscale interactions to the point where even submonolayers of adsorbents on a surface can dictate the tribological behavior of a contact [8]. As illustrated in Figure 1.2, a seemingly smooth surface at the macroscale will show degrees of roughness at finer scales ("asperities upon asperities upon asperities upon...") until the ultimate limit: the atomic scale. In modeling a sliding surface, one would come to vastly different conclusions if one were to model a smooth surface as opposed to a
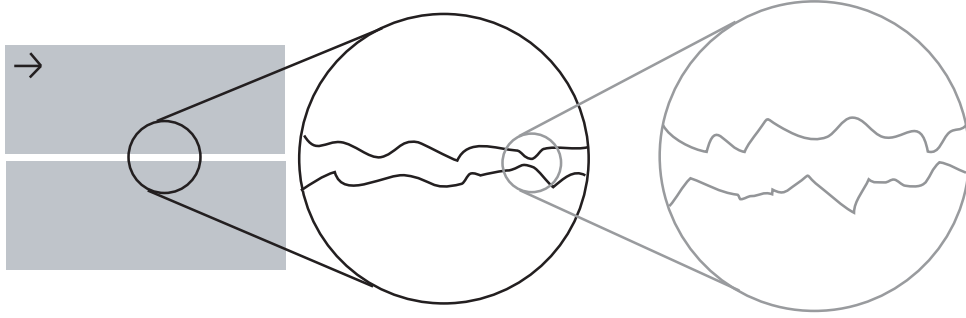
Figure 1.2. Asperities upon asperities.

nanoscopically rough surface [9]. The goal of nanotribological research in the end is to understand the molecular origins of friction so that models may be successfully generated to handle phenomena on all scales. Below is a summary of the tools, both experimental and theoretical, that have been employed in the field of nanotribology for characterizing sliding interfaces.

Extraordinary developments in experimental techniques over the past two decades have accelerated interest in researchers to study friction on the nanoscale. Here we will describe the common experimental techniques that have yielded new understanding of friction between solids at the nanoscale.

1.3.1. Scanning Probe Techniques

Scanning probe microscope (SPM) techniques are often said to have catalyzed the nanotechnology revolution of the past two decades. With the introduction of the scanning tunneling microscope (STM) in 1981, conductive samples could be characterized by measuring a weak tunneling current with a small tip. Five years later, Binnig, Quate and Gerber developed the atomic force microscope (AFM) [10]. By optical detection, the
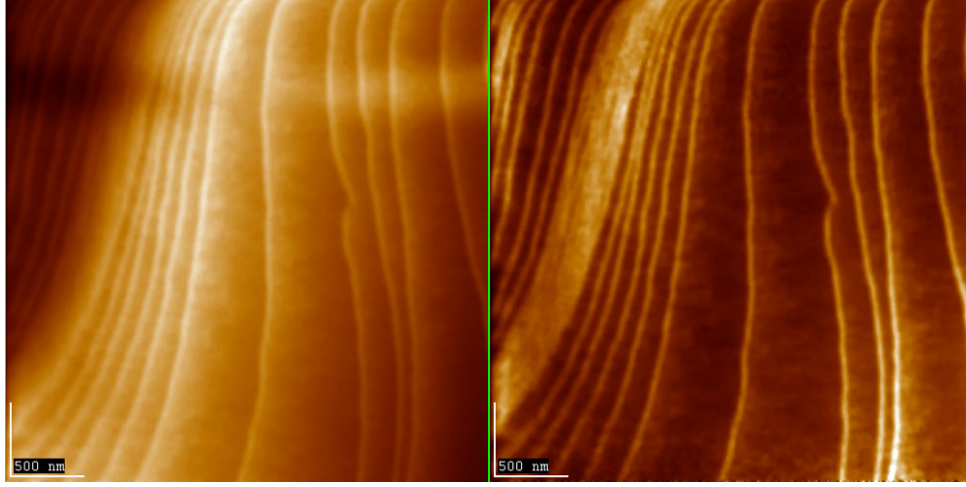
Figure 1.3. AFM topograph (left) and lateral (friction) force map (right) of a cleaved NaCl surface. Surface steps show higher friction than terrace regions.

interaction between a microfabricated cantilever and a surface's atomic potential is monitored as the probe is dragged across the surface of a material. By measuring the normal force between a small tip and sample, the AFM is capable of measuring the vertical topography of a sample's surface. Modifications were soon made to measure lateral forces by torsional deflections of the cantilever [11]. Known as friction (or lateral) force microscopy (FFM, LFM), this technique immediately gave rise to friction experiments between single asperity probes at forces on the order of a nanonewton.

Atomic-scale friction phenomena including stick-slip [11], superlubricity [2, 12, 13], anisotropy [2], and velocity dependence [14] have been demonstrated by use of scanning probe techniques. Mate et al. [11] showed that a scanning tungsten probe gave atomic-scale features when sliding across the basal plane of a graphite surface at forces below 10^{-4} N. Later studies demonstrated atomic stick-slip behavior on different substrates, including Mica [15], Cu [16], NaF [17], KF [18] and Diamond [19]. Modifications of this

technique have pushed force resolutions in the lateral dimension to tens of piconewtons [2].

1.3.2. Surface Force Apparatus

Tabor, Winterton and Israelachvili first developed the "surface forces apparatus" (SFA) to measure friction between elastic contacts between atomically smooth surfaces [20, 21]. The device operates by a simple combination of gear and piezo positioning motors, and spring force sensing devices. Coiled springs measure both lateral and normal forces directly, for micrometer sized contacts. The relationships between adhesion and friction for flat surfaces, and particularly the behavior of thin trapped liquids (lubricants), have been successfully analyzed with this technique [22].

1.3.3. Quartz Crystal Microbalance

The quartz crystal microbalance (QCM) has given researchers the ability to probe friction on a very short time scale between molecularly thin solid or liquid films. It operates by oscillating a quartz crystal at a sharp resonance frequency (typically 5-10 MHz). The adsorption of thin films to the metal electrodes lowers this resonance frequency by a given amount, which can be correlated to the amount of frictional energy dissipation. The broadening of the resonance peak will indicate whether slippage at the interface has occurred. All of this information can then be used to address fundamental questions about energy dissipation such as electronic and phononic effects.

Krim *et al.* showed that solid krypton films exhibit lower friction than liquid films, leading to a counterintuitive "slippery when dry" conclusion [23]. The results of this

experiment have been elegantly corroborated by theoretical simulations of phononic drag [24]. The effect of electronic drag on a sliding monolayer interface has also been investigated for N_2 films sliding on Pb substrates [25, 26].

1.3.4. Theoretical Methods

A basic atomic scale sliding model was developed by Tomlinson [27]. His approach attached a point mass (single atom) to an isolated slider via a spring, which was then dragged across a given potential that estimated an atomic lattice. Various extensions have been proposed [28] of which the most widely used is the Frenkel-Kontorova approach. In this model one of two materials is represented by a periodic potential, and the other by a set of atoms connected by simple springs (or more complicated functional forms) to the other material. As the two bodies slide past each other the motion of the atoms in the potential leads to the forces associated with friction.

More powerful and complete models - in principle somewhat similar - have been developed using atomistic approaches including molecular dynamics (MD) [29, 30, 31, 32, 33, 9]. This class of simulations have been used to study atomic-scale stick-slip [34], liquid-solid interfaces [35], dry sliding [36], static friction [37] and molecular films [24, 38]. Limitations of this technique include length and time scale restrictions as well as interaction potential selection. Of the more interesting developments in simulations, the use of hybrid models to characterize both atomistic and continuum mechanisms [39, 40] poses some promise. An interesting application of these mixed models is the study of nucleation and motion of dislocations, which is typically unavailable to other methods because of length scale

limitations. Time scales, however, remain a major limitation of computational techniques when studying non-equilibrium phenomena such as friction.

1.4. New Approaches to Solid Friction on the Nanoscale

With the techniques described above, both experimental and computational, a wealth of information regarding the way surfaces behave under sliding conditions at the nanoscale has become available. Tribological research on the nanoscale has become increasingly multidisciplinary, with physicists, chemists, surface scientists, and materials scientists continually joining the mix. There remains a need to communicate old ideas from separate fields to one another to improve the fundamental understanding of friction.

In this thesis, I will describe how we approached solid friction from a materials science perspective. It is the hope that a fresh view on a very old topic will spur more ideas and understanding within the community. The work contained herein can be broadly divided into three sections. The first, covered in Chapter 2, is a theoretical analysis of friction between atomically smooth single crystals. By taking a step back from complex numerical methods, I examine friction from the standpoint of the basic element of materials deformation: the dislocation. Imperfections in materials, and understanding how their structure and behavior affect properties, are the historical cornerstone of materials research. It is with this perspective, I outline a simple model for solid friction that combines elements of known dislocation drag theory, contact mechanics and the structure of interfaces (grain boundaries).

The second section (Chapter 3) is devoted to more traditional macroscopic friction experiments that sought evidence for some of the conclusions in Chapter 2. More specifically, cubic single crystals were used to perform sliding experiments to determine how friction depends on the periodicity of materials. This was accomplished by varying the misorientation angle between crystals in order to provoke an anisotropic response to the friction force.

The remaining chapters (Ch. 4-7) constitute the final section of this work, by introducing the implementation of an emerging technique that will be of tremendous use to the tribological community: *in-situ* transmission electron microscopy (TEM). The TEM has been an invaluable tool in investigating materials of all types with full quantitative characterization abilities including electron diffraction, electron and x-ray spectroscopies, and imaging down to the sub-Angstrom level. We have used a specialized holder that makes it possible to perform STM and AFM studies inside the TEM, for real-time analyses of real materials deformation mechanisms. With picometer-scale control of a sliding single asperity within the TEM, it is finally possible to visualize and chemically characterize the most basic interactions at a tribological interface. Chapters 4 through 6, analyze three different materials - graphite, gold, and amorphous carbon films - and draw real unambiguous structure-friction relationships. The final Chapter in this thesis will serve as practical guide to the operation of the *in-situ* holders, so that future students and researchers may learn from my successes and (plentiful) mistakes.

CHAPTER 2

Analytical Model for Crystalline Sliding Interfaces

2.1. Motivation for a new friction model

The laws of friction dating back to DaVinci, Coulomb and Amontons still see use to-day for basic interpretations of macroscopic phenomena [1]. Unfortunately, none of these laws are universally valid; more importantly, nothing fundamental about the dissipative processes associated with friction may be derived from these basic expressions [41], un-like, for example, Newton's laws. Nanotribological friction experiments, enabled by the development of tools with high force sensitivities on small length scales, have shown that the macroscopic friction laws generally do not hold at the nanoscale: the scale on which individual asperities touch.

The atomic origins of friction have been the subject of theoretical studies since the introduction of Tomlinson's model [27] of a ball and spring dragged over a periodic poten-tial. This model and its successors including the Frenkel-Kontorova [28] model produced a number of successful solutions for interfaces including stick slip behavior in friction [42], the formation of misfit dislocations [43, 44] and more general commensurability effects in static [45] and kinetic cases [42]. Unfortunately in most cases these models describe static friction, and do not always include the dissipative terms which describe dynamic friction. More recently, numerical methods, such as molecular dynamics have studied atomic scale friction phenomena on short time and length scales [46, 47].

Consider the *gedanken* case of forming an interface between two grains (of the same or different materials) of periodic materials by placing cut sections of the perfect lattices in contact. At the interface there will be unbalanced stresses due to the mismatch of the two lattices. In almost all cases, these are relieved by the formation of dislocations near the interface; this is true independent of whether we are talking about metals, ceramics or crystalline polymers (e.g. self-assembled monolayers). Note that these dislocations are intrinsic to the presence of the boundary, and are not introduced by any external action such as deformation. Suppose we now apply a shear stress across the interface as in a friction experiment. Relative sliding can occur via:

(1) Motion of dislocations near the interface

(2) Motion of dislocations away from the interface

(3) Rigid body translations of the two materials as in a Tomlinson model.

It is well known that in general mode (3) requires much higher stresses than either (1) or (2); plastic deformation is almost always achieved via dislocation motion. If the interface is relatively weak compared to the bulk material the low energy path will almost always be (1). The dominant dissipative forces associated with the motion of dislocations are well documented in the literature [48].

The purpose of this study is to develop a general model for friction considered in terms of the dissipative forces on interfacial dislocations. This friction model is solved analytically from first principals, combining elements of three independently well-known physical theories: interface theory, dislocation dynamics and contact mechanics. Strictly speaking, the model only applies to the unique case of a perfectly flat interface. However, since the model is analytical (not numerical) it can be used to extract general trends.

Furthermore it is quite plausible to extend the model to more experimentally realistic cases, such as when there are barriers to dislocation motion near the interface, using well-established existing information about dislocations.

We will first take a look at each of these theories independently so that the combined model may be understood from a common viewpoint. We acknowledge that large parts of these fields are well established, but it is nonetheless useful to summarize them here, realizing that despite their diverse origins, they may collectively play an important role in the study of friction at the nanoscale. General discussion is available in the literature regarding the theories of interfaces [49, 50, 51], dislocations [52, 53] and contact mechanics [54, 55, 56].

2.2. Crystalline Interfaces

2.2.1. Coincident Site Lattice (CSL)

The first step in generating our model requires an understanding of interfacial dislocations. The standard approach in defining interface structure is based upon coincident site lattice (CSL) theory developed by Bollmann [57, 58] and Grimmer [59] as a geometric model describing the coincidence, or goodness of fit of atomic lattice sites at an interface. To introduce the basics of CSL theory, imagine two parallel atomic lattices are brought into contact. The two structures are considered perfectly coincident if each lattice site directly mirrors its counterpart through the interfacial plane as illustrated schematically in Figure 2.1. This, of course, is an exceedingly rare condition, and for a given in-plane rotation (pure twist boundary) of one of the surfaces most of the lattice sites will fall out of coincidence with the opposing surface. However, some small fraction of atomic sites will
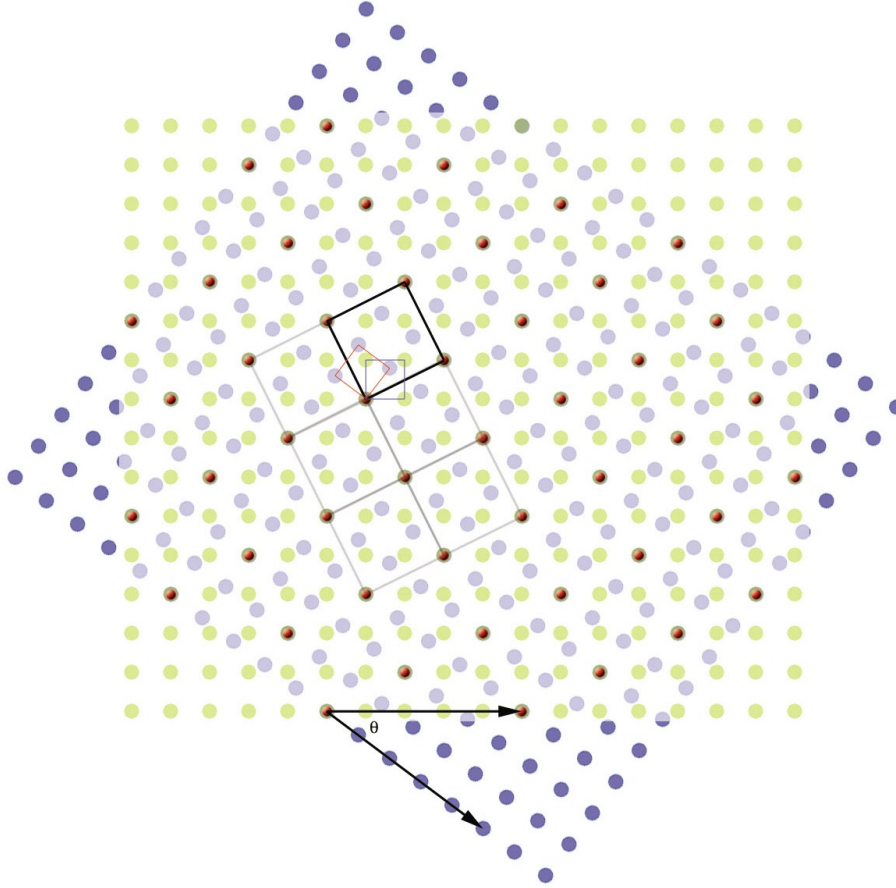
Figure 2.1. Plan view schematic of a $\Sigma 5$ CSL boundary, an in-plane rotation of two cubic lattices by $36.87°$. Red dots indicate coincident sites.

be shifted into coincidence forming a unique periodic structure, as shown in Fig. 2.1 for the $\Sigma 5$ CSL. This periodic arrangement can be mathematically described as a two-dimensional lattice, where the inverse fraction of sites in coincidence relative to the total number of real projected interfacial atomic sites is represented by its Σ value. Hence, a $\Sigma 5$ coincident site twist boundary has 1/5th the total number of interfacial atoms in coincidence and results from an in-plane misorientation of $36.87°$ (Figure 2.1).

For real non-rigid interfaces, boundary dislocations will form to accommodate lattice strain. Between dislocations, interfaces tend to form structures that match low Σ values.

Table 2.1. List of the lowest index CSL boundaries and their corresponding misorientation angles for (100) cubic twist boundaries.

Σ	θ
1	0°
5	36.87°
13	22.63°
17	28.07°
25	16.27°
37	18.93°
41	12.68°
53	31.89°

Although the exact relationship between the degree of coincidence and grain boundary energy is unknown, it is generally accepted that higher coincidence yields lower energy boundaries. In fully relaxed cases, interfaces are energetically preferred at slight misorientations inducing periodically spaced dislocations relative to exact low index boundary configurations. This corresponds to an energetic balance between regions of perfect Σ registry separated by small regions of misfit at grain boundary dislocations. A misfit boundary consists of an intersecting network of screw dislocations, as shown in Figure 2.2. In this case, Frank's formula [53] describes the dislocation separation distance L for a given offset $\Delta\theta$ from a known CSL misfit orientation, θ:

$$(2.1) \qquad L = \frac{|\mathbf{b}|}{2\sin(\Delta\theta/2)}$$

where $\Delta\theta$ is the angular increment away from a perfect Σ boundary orientation. This expression can be generalized for both twist and tilt boundaries, containing edge- and screw-type dislocations.
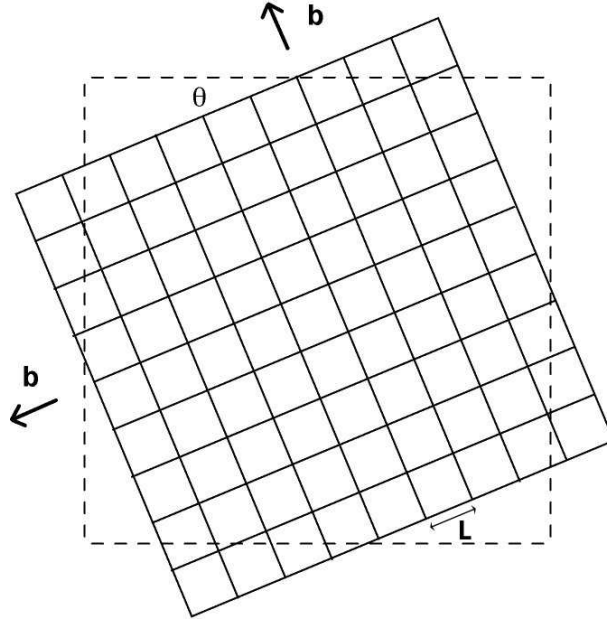
Figure 2.2. Twist grain boundary shown in plan view illustrating the intersecting misfit dislocations that give a distribution of orthogonal Burgers vectors.

2.3. Dislocation Drag

We now turn to the dissipative forces associated with moving dislocations. Early investigations of the sources of dislocation drag considered the main source to be associated with phononic dissipative processes. Originally [60], it was suggested that the motion of dislocations should follow a standard viscous force model, with drag directly proportional to velocity. However, as experimental evidence for nonlinear mobility of dislocations emerged [61, 62], it became clear that a viscous model could in no way completely describe the dynamics of dislocations. Now it is understood that several mechanisms influence the mobility of dislocations through a solid, and that competition between thermal fluctuations and dynamic radiative processes takes place [48, 61, 62].

Most phonon contributions to dislocation drag behave viscously, that is, with direct proportionality to the velocity. They can be described by a drag coefficient, B, having the following relation:

$$(2.2) \qquad\qquad \mathbf{F} = B\mathbf{v}$$

where B_{tot} is the total drag coefficient and $\mathbf{v}$ is the dislocation velocity. More acurately, this expression should read

$$(2.3) \qquad\qquad \mathbf{F_i} = \mathbf{B_{ij}} \cdot \mathbf{v_j}$$

where the drag coefficient is a tensor quantity, and contains anisotropic effects. B will be expressed as a sum of a number of viscous drag effects, which we will now explore.

2.3.1. Phonon Drag

Phonons interact with dislocations in several distinguishable ways. The first significant mechanism, known as the phonon wind, arises from an aberrational effect associated with a phonon distribution in a moving reference frame. Phonons are scattered by moving dislocations as a result of the nonlinear elastic properties of the crystal. The expression for the damping coefficient of a screw dislocation by the phonon wind [63] is

$$(2.4) \qquad\qquad B_w = \frac{1 + \left(3 + \frac{n}{2\mu}\right)^2}{\pi^2} \frac{h}{b^3} \left(\frac{bk\Theta}{3\hbar c_t}\right)^5 f\left(\frac{T}{\Theta}\right)$$

where μ is the shear modulus, b is the magnitude of the Burgers vector, k is the Boltzmann constant, ct is the shear wave velocity, n is a Murnaghan coefficient, and Θ is the Debye temperature. f(x) is a more complex function of temperature, and is expressed for screw dislocations as

$$(2.5) \qquad f(x) = x^5 \int_0^{1/x} dt \frac{t^5 e^t}{(e^t - 1)^2}$$

In the limiting case of T$\gg\Theta$, Bw becomes

$$(2.6) \qquad B_w = \frac{b}{\pi^2 c_t} \left(\frac{3kT}{b_3} \right) \left[\frac{1 + \left(3 + \frac{n}{2\mu}\right)^2}{36} \left(\frac{bk\Theta}{3\hbar c_t} \right)^4 \right].$$

Since a dislocation within a crystal contains its own degrees of freedom, it may vibrate in the thermal motion of the lattice and consequently radiate elastic waves. This is known as the flutter effect [64], and is expressed by

$$(2.7) \qquad B_{fl} = \frac{\hbar k_D^3}{\pi^2} f \left(\frac{T}{\Theta} \right)$$

where k_D is the upper limit to the Debye spectrum, and f is yet another complex function [64] of temperature. For a description of this temperature term, we direct the reader to a work by Alshits [64]. The flutter effect is a re-radiation of phonons oscillating in a thermal lattice field and will dominate over the phonon wind (nonlinear scattering) mechanism at low temperatures and in materials with a low degree of anharmonicity.

2.3.2. Electron Drag

Electrons also interact with moving dislocations, leading to a drag force that opposes motion. An expression for the electronic damping of dislocations was solved by Holstein [65] to be

$$(2.8) \qquad\qquad B_e \cong \frac{bN_e\epsilon_F}{10v_F}$$

where N_e is the number of conduction electrons, ϵ_F is the Fermi energy, and v_F is the Fermi velocity. Typically, this value is not significant at room temperature where phonon effects dominate. However, where phonon modes are frozen out at low temperature and where the free electron density is sufficiently high, this term can be on the same order as the total phonon contribution [48]. However, it remains a somewhat complex process, since low temperatures necessitate the consideration of the superconducting transition, an entirely separate phenomenon. The effect on mobility of dislocations traveling through bulk solids by superconductivity has been observed experimentally [66, 67, 68, 69, 70] and predicted theoretically [71], and we expect it to behave similarly in the case of solid friction.

2.3.3. Radiation Friction

The phonon wind, flutter and electronic drag mechanisms compose the principal viscous drag contributors to dislocations moving through a solid. A separate mechanism, radiation friction, plays a dominant role at low velocities, where friction studies are most relevant. The discreetness of the atomic lattice means that the strain field associated

with a moving dislocation oscillates with time, and elastic waves radiate from the configurational oscillations of the dislocation core. Even at absolute zero, when all other dissipative channels are eliminated, this effect remains strong. Alshits solved a stabilized form [72] by including the previously determined viscous drag terms into the form

$$(2.9) \qquad\qquad F = \sigma_p b coth \left[\frac{b\sigma_p}{B_{tot} v_d} \right]$$

where σ_p is the Peierls stress and B_{tot} is the viscous drag coefficient. B_{tot} can be broken down linearly into its individual components (phononic and electronic):

$$(2.10) \qquad\qquad B_{tot} = B_e + B_w + B_{fl}$$

Consistent with the phenomenon of static friction, the total radiation drag stress approaches a finite value, σ_p, in the limit of zero velocity.

2.4. Contact Mechanics

The dissipative forces described in the previous section only apply over the true contact area, a standard problem in contact mechanics [55]. Here we summarize the models in brief.

2.4.1. Hertzian Contact

The Hertzian (nonadhesive) contact area, A, between a plane and a sphere follows a load, F_N, dependence

$$(2.11) \qquad A = \pi \left(\frac{RF_N}{E'} \right)^{2/3}$$

where R is the radius of the sphere, and E is the effective modulus given by

$$(2.12) \qquad \frac{1}{E'} = \frac{4}{3} \left(\frac{1 - \nu_1^2}{E_1} + \frac{1 - \nu_2^2}{E_2} \right),$$

where E_1 and E_2 and ν_1 and ν_2 are the Youngs modulus and Poissons ratios of the two materials, respectively. This formulation assumes a nonadhesive interaction, and therefore underestimates the contact area for small contacts.

2.4.2. JKR, DMT, and Maugis-Dugdale Theory

Johnson, Kendall and Roberts (JKR), and Derjaguin, Müller and Toporov (DMT) theories extend Hertzian contact formulations to account for adhesion for short-range and long-range interactions, respectively. JKR theory, applicable for compliant materials, treats the contact as Hertzian plus a crack tip stress at the edge of the contact, replacing the normal load, F_N, with $F_N + 3\pi wR + [6\pi wRF_N + (3\pi wR)^2]^{1/2}$, where w is the work of adhesion per unit area. DMT, considering the case of hard materials and small contacts, simply adds the work of adhesion over the herzian contact area to the normal force: $F_N + 2\pi wR$. The inclusion of an attractive force to the normal load yields a finite contact area at zero load for both cases. However, the functional relationship between contact

area and load of each approach is rather different, and does yield qualitatively different results. For example, the contact area tends to zero at pull-off for DMT, while JKR's solution remains finite. Also, the magnitude of the pull-off force is quite different. A more robust solution was developed by Maugis that uses a square well potential ("Dugdale") to more accurately describe the interaction potential between surfaces. A parameter, λ, is defined as

$$(2.13) \qquad \lambda = 2\sigma_0 \left(\frac{R}{\pi \gamma E'^2} \right)^{1/3},$$

where σ_0 is defined as a constant adhesive stess acting over an interaction range. The Maugis parameter, λ, defines an interpolation between the limiting cases of JKR and DMT contacts, and has been used to successfully fit a number of solid-solid friction experiments. Johnson and Greenwood have summarized the applicability of this transition parameter [73].

2.5. Analytical Model Development

Now that we have established the fundamental theories related to the contact of crystalline bodies, we turn to the specific development of the proposed model for interfacial solid friction. Consider an interface between two materials in terms of an array of misfit dislocations of Burgers vector **b** with a nearest-neighbor separation of L. The separation, L, is determined by the periodicity and relative orientation of the two contacting surfaces.

If the two bodies are in relative motion with a velocity, V, the dislocation velocity, v_d, will be:

$$(2.14) \qquad \mathbf{v_d} = \frac{L}{b^2}\left(\mathbf{b} \cdot \mathbf{V}\right).$$

This proportionality arises from the geometric condition that requires a single screw dislocation to be punched out one interdislocation length after an orthogonal surface displacement of one Burgers vector (Figure 2.3). The motion of a dislocation with Burgers vector, $\mathbf{b}$, and line vector, ξ, will follow the Peach-Koehler relation: $F = (\mathbf{b} \cdot \sigma) \times \xi$, where σ is the applied shear stress, and will move in a direction normal to the Burgers vector. For the case of pure misfit dislocations in a cubic twist boundary, the Burgers vector distribution describing their magnitude and orientation will be in-plane and orthogonal to one another. Because of this distribution, a cosine (dot product) dependence on the drag force results from changing the sliding direction. Only dislocations with Burgers vector components in the direction of sliding experience a drag force.

The expression for the velocity of interfacial dislocations (Eq. 2.14) is substituted into the radiation dragging term (Eq. 2.9). Frank's equation (Eq. 2.1) for the dislocation spacing, L, is also substituted into Eq. 2.9; converting back to the retarding force that needs to be overcome for continuing motion at the macroscopic level (accounting for the arrangement of dislocations in a twist boundary) gives

$$(2.15) \qquad F_{macro} = \frac{N_d \gamma \sigma_p b}{2} \coth \left[\frac{2 b \sigma_p \sin(\Delta\theta/2)}{B_{tot} V}\right]$$
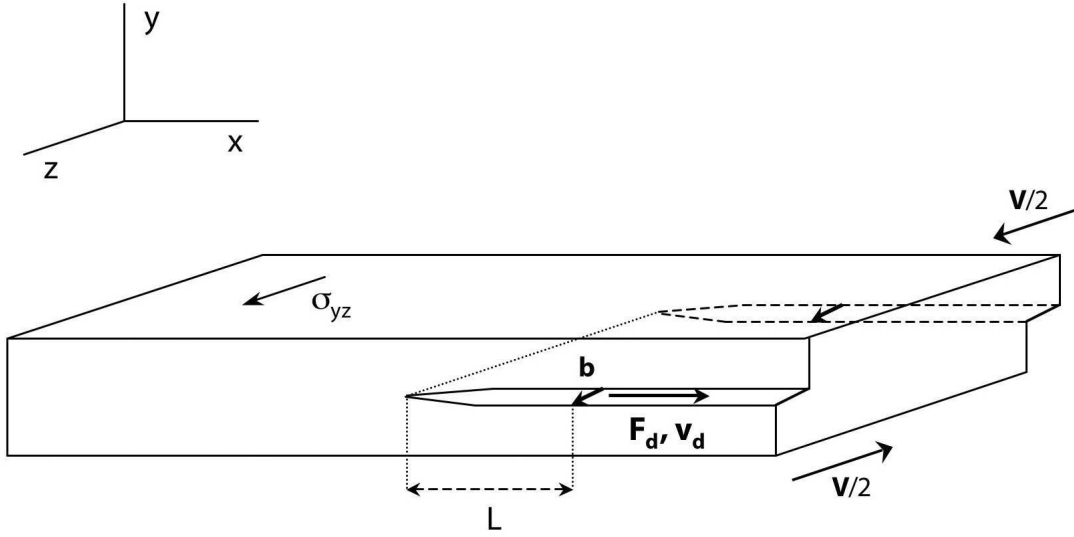
Figure 2.3. Forces on a screw dislocation in response to a shear.

where $\gamma = \sin(\theta) + \cos(\theta)$, N_d is the number of dislocations in the contact area, Θ is the absolute in-plane misorientation angle and $\Delta\theta$ is the angular displacement from a given coincident site orientation (Σ boundary). γ represents the orthogonal distribution of Burgers vectors in a lattice for a pure cubic twist boundary, and may readily be generalized for tilt or more complicated boundaries. Tilt boundaries containing edge dislocations have not been calculated here, but will follow the same model formulation. It necessitates a geometric transformation accounting for the dislocation distribution (Frank's formula) and a reevaluation of the viscous and radiation drag terms. The viscous terms for edge-type dislocation drag are known and will change slightly in magnitude and temperature dependence; the more significant consideration requires an analysis of the core structure of the edge dislocation for radiation drag. We are currently unaware of a closed form analytical solution of this type.

One last step is needed to account for the true area of contact. In the analysis above we have considered perfect contact between the two bodies, but it is known that in reality a small number of asperities are in contact. The most basic definition for the friction coefficient can be written as

(2.16)
$$\mu = \frac{F_{macro}}{F_N}$$

where the normal load F_N, will determine the dislocation array length A. The friction coefficient is only meaningful if specific geometric and materials parameters are known for the contact, since friction can vary significantly with load. Variation in calculated values for μ (static or kinetic) will result from the selection of different contact models, e.g. Hertzian, JKR, DMT, or through the choice of specific materials dependent factors as compliance and adhesion. For this reason, Eq. 2.16 is left in this general form, where F_{macro} depends on the dislocation density and the contact area as given by a chosen contact model.

2.6. Model Results

2.6.1. Friction Forces vs. UHV Data

An important step in validating the present model is examining whether calculated friction forces match experimental data. Values are calculated for the macroscopic friction coefficient based on a limited number of available UHV friction studies. It must be stressed that the calculated values for μ are not universally valid, rather they represent specific values calculated for the experimental conditions (load, tip shape, sliding velocity, environment, material) given in the referenced studies and fundamental materials constants. Upper and

lower limits for the dislocation spacing, L, were taken from experimental results of TEM studies of manufactured twist grain boundaries [74, 75, 76]. Table 2.6.1 lists the values for μ as calculated by our analytical model and as reported in UHV friction experiments [77, 78, 79]. The experimental friction values fall within the models calculated range; not only is there good absolute agreement, but relative changes in measured coefficients of friction between different metals are also accounted for. Friction was seen to increase from Fe (lowest) to Ni (highest), something that is directly predicted by the analytical calculations. Although the range of values in Table 2.6.1 vary by two to three orders of magnitude - something which is rarely seen experimentally - they represent upper and lower bounds of ideal single crystalline contacts. To this end, even the most careful UHV friction experiment will inevitably measure friction between somewhat non-perfect crystals, including a variety of imperfections, such as surface steps, kinks or reconstructions.

The calculated values in Table 2.6.1 contain a dependence of friction with load. However, one of the most common macroscopic observations is that friction varies little as a function of normal load. In order to account for this, an accurate multi-asperity model is needed for incorporation into the calculations [80, 81]. A complete topographic analysis of the surface would allow for the statistical analysis (autocorrelation, roughness, skewness, kurtosis) of asperity heights leading to a more load-independent calculation of friction forces for multi-asperity contacts.

Some uncertainty exists in the literature whether friction is directly proportional to contact area. First Amontons said it was untrue, only to be corrected by Bowden and Tabor by explaining the real area of contact was a small fraction of the apparent area of contact. Several studies have assumed direct proportionality between the friction force

Table 2.2. Friction coefficient calculations compared with UHV friction data from Fe(100), Cu(111), and Ni(100).

Σ	L [nm]	$|b_{hkl}|$ [Å]	v_d [m/s]	F_N [mN]	T [K]	μ_{exp}	μ_{calc}	REF
Fe(100)		2.87		100-150	300	**5.8 ±1.1**		[79]
1	5		1.05E-04	"	"		**92.82-106.3**	
1	25		5.23E-04	"	"		**11.14-17.00**	
5	5	1/10<310>	1.05E-03	"	"		**9.28-10.62**	
5	25	"	5.23E-03	"	"		**1.11-1.69**	
25	5	1/25<430>	2.61E-03	"	"		**3.71-4.25**	
25	25	"	1.31E-02	"	"		**0.45-0.67**	
Cu(111)		2.55		25-50	100	**7.8 ±1.8**		[77]
1	5		3.92E-04	"	"		**275.1-346.6**	
1	25		1.96E-03	"	"		**11.0-13.86**	
5	5	1/10<310>	3.92E-03	"	"		**27.51-34.67**	
5	25	"	1.96E-02	"	"		**1.10-1.39**	
25	5	1/25<430>	9.80E-03	"	"		**11.0-13.86**	
25	25	"	4.90E-02	"	"		**0.44-0.55**	
Ni(100)		3.52		40	300	**8.6 ±2.5**		[78]
1	5		2.84E-04	"	"		**495.7**	
1	25		1.42E-03	"	"		**31.72**	
5	5	1/10<310>	2.84E-03	"	"		**49.57**	
5	25	"	1.42E-02	"	"		**3.172**	
25	5	1/25<430>	7.10E-03	"	"		**19.83**	
25	25	"	3.55E-02	"	"		**1.269**	

and contact area by an interfacial shear strength, τ_0 [82, 83]. However, challenges to this idea have come from both theory [37] and experiment [84, 85]. A dislocation-friction model offers an alternative explanation. It is entirely consistent to satisfy both conditions (constant or changing friction force), while holding the real contact area constant, since the dislocation structure is intrinsic to the interface and is a function of crystallographic mismatch. Recent atomistic simulations indicate that small atomic structure modifications (atomic scale roughness) to a scanning tip can induce a profound variation in friction behavior [9, 86], much in the same subtle way that dislocation structure is shown to greatly affect friction as calculated here.

2.6.2. Friction vs. Velocity

The velocity dependence of the friction force (equation 2.15) yields two types of dislocation drag behavior, as shown Figure 2.4. The radiation drag regime tends to a constant value (Peierls barrier) as sliding velocity goes to zero, or an effective static friction value. As velocity increases, a transition to viscous sliding occurs. The location of this knee is sensitive to the Peierls stress of the interface, temperature and viscous drag components.

Figures 2.5 and 2.6 show the dependence of the macroscopic friction force (Eq. 2.15) on the dislocation velocity for the $\Sigma 1$ boundary. The calculations for Figure 2.5 use experimental parameters given by McFadden for UHV sliding of Cu single crystals [77], while Figure 2.6 demonstrates the effect of reducing the Peierls stress for Cu. The radiation friction term clearly dominates the friction force at low velocities, and the asymptotic convergence to the Peierls stress at zero velocity indicates that static friction exists for all cases where a Peierls-type barrier is present. The critical velocity knee, where viscous
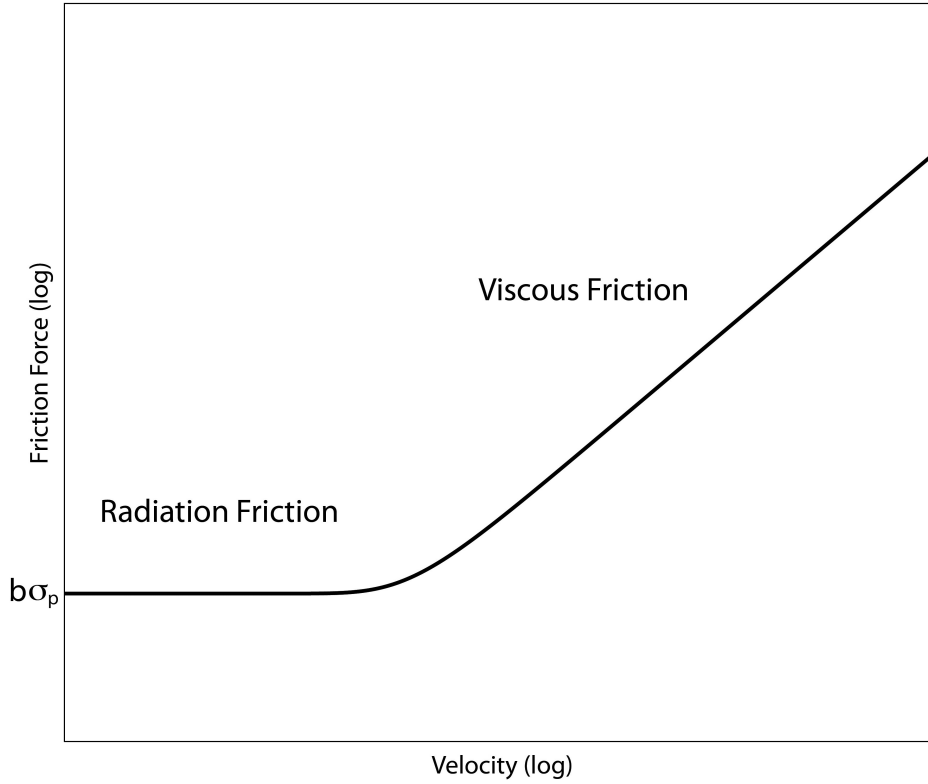
Figure 2.4. Log-log plot of the friction force vs. sliding velocity (arbitrary units) from Equation 2.15

effects begin to dominate, is strongly dependent on the Peierls resistance and the temperature and can exist in bulk metals at significant fractions of the shear wave velocity. This critical velocity is small for systems that are weakly bound (sliding monolayers), shear easily in preferred crystallographic directions (graphite, MoS_2), or contain third body lubricating layers.

It is worth noting that an exceedingly similar velocity dependence has very recently been observed for glassy polymethylmethacrylate and octadecyltrichlorosilane [87]; in terms of the model used here it corresponds to a Peierls stress of 0.02-1 Pa which we believe is a reasonable number for a polymeric system.
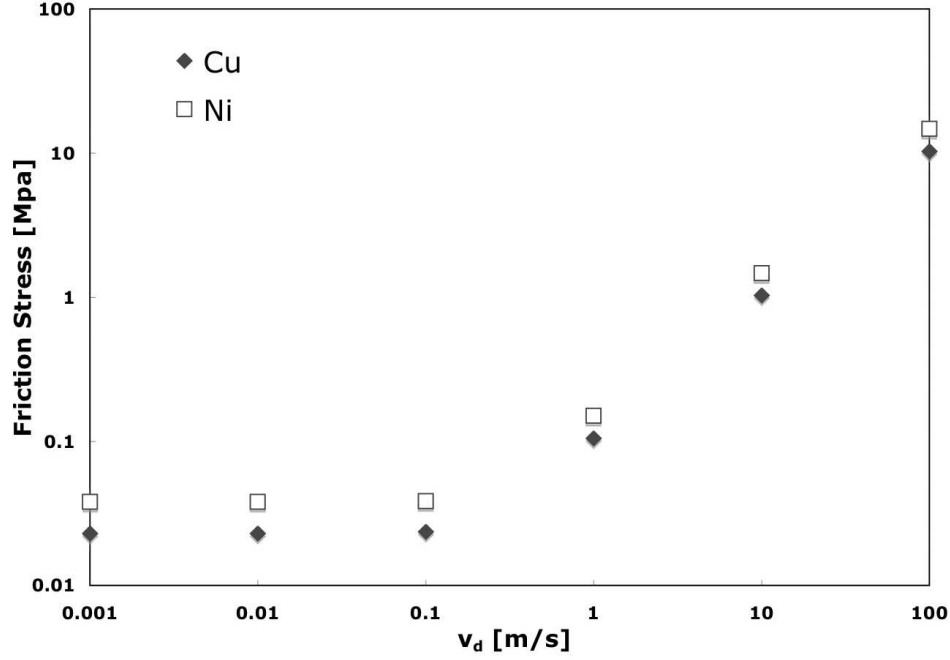
Figure 2.5. Effective friction stress per dislocation vs. dislocation velocity for Cu and Ni at experimental conditions used by McFadden.

2.6.3. Friction vs. Temperature

A graph of the temperature dependence of Eq. 2.15 is given in Figure 2.7 for the case of Cu. Although the precise temperature dependence of the Peierls stress, $\sigma_{p(T)}$, is not known, it has been experimentally observed to decrease by an order of magnitude between 4.2 K and 300 K in close packed metals [88]. Competition exists at finite temperatures between increased viscous drag contributions that increase the required stress and an activation rate increase that lowers it. Landau derived the effective velocity of a dislocation as a function of a statistical thermal surmounting of randomly spaced Peierls barriers [89]. The inclusion of this velocity correction term , where ΔH is the activation enthalpy estimated to be 0.01 eV and k is the Boltzmann constant, has a minimal effect on the radiation force
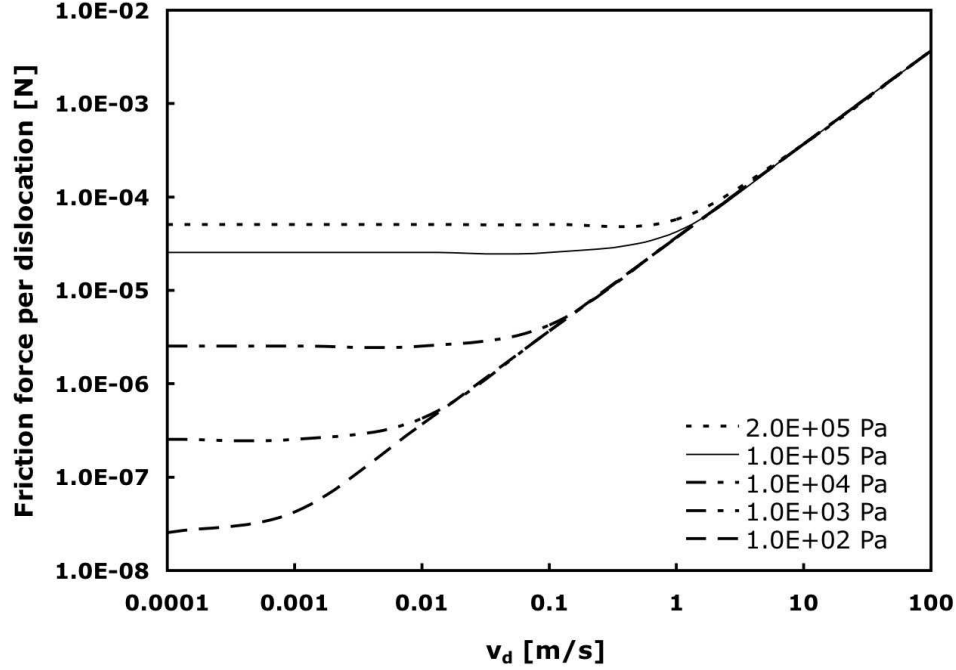
Figure 2.6. Friction force per dislocation vs. dislocation velocity for various shear stress values. Baseline is $2 \cdot 10^5$ Pa for Cu at room temperature.

term, where force is nearly constant with velocity. However, the correction is significant for the viscous dominated regime.

2.6.4. Friction Anisotropy

To further illustrate the consequences of Eq. 2.15, Fig. 2.8 shows how the friction force, F_{macro},varies as a function of misorientation angle for highly coincident boundaries. An anisotropic friction force shows increases in friction at misorientations consistent with CSL theory. The choice of CSL boundaries in Fig. 2.8 is limited to the highest density of coincident site states. The determination of a cutoff in the number of peaks is not trivial, but experimental studies on (100) twist boundaries have confirmed the existence of unique dislocation networks as high as $\Sigma 41$ [90]. At which point misorientations away from
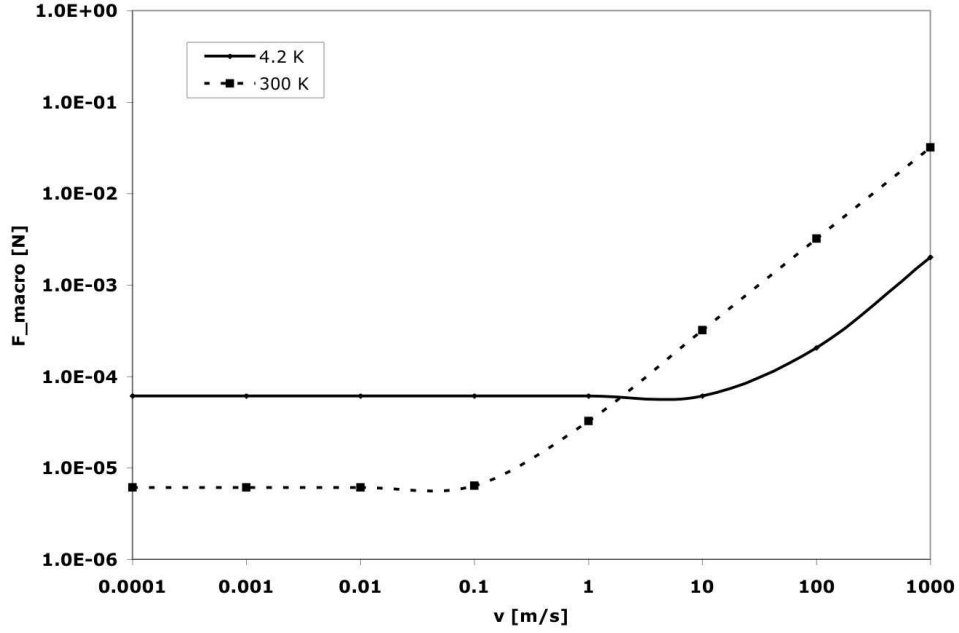
Figure 2.7. Friction force (F_{macro}) vs. dislocation velocity at room temperature and 4.2 K.

CSL boundaries will yield areas of higher coincidence remains a subtle and unanswered question.

Friction anisotropy is predicted by our model for both variations in sliding direction and misorientation (same sliding direction). For variations in sliding direction, the dislocation distribution, γ, gives rise to this dependence, in agreement with other experimental and theoretical suggestions [12, 91]. The sinusoidal dependence comes from the orthogonal distribution of an array of dislocations at a misfit boundary. More complicated dislocation structures would yield a less obvious sliding direction anisotropic dependence. Experimental evidence [12, 2, 92, 78, 93] for friction anisotropy exists for several solid-solid interfaces, but no general consensus exists as to the specific sliding conditions that yield this effect. Our model also predicts that misorientation anisotropy increases with
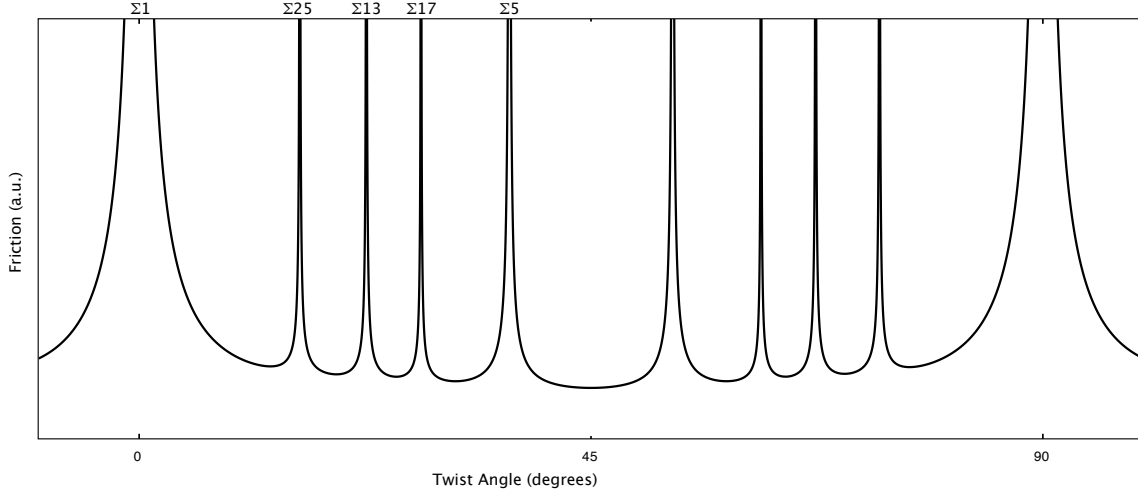
Figure 2.8. Friction force as a function of in-plane misorientation angle showing peaks at major cubic (100) CSL boundaries.

velocity, where viscous dislocation drag becomes the dominant retarding force. A tradeoff can be made for high velocity experiments by studying a system at higher temperatures or with a lower Peierls barrier resistance (sliding monolayers). A higher degree anisotropy will occur when shifting from a radiation friction dominated process to one of viscous drag.

2.7. Discussion

The model we have described gives quite reasonable numbers for friction forces between crystalline materials. Many real cases will not be dominated by just the interfacial term that we have considered, but will involve more complicated dislocation motion. Just as plastic deformation of materials at the nanoscale depends on the motion of dislocations which at a continuum level can be represented by, for instance, constituent models, we will argue that the nanoscale understanding of friction must involve dislocation motion

near the interfaces which can be built up into more continuum scale constitutive friction models.

We certainly cannot as yet explain all frictional phenomena, but there are a number of cases where there are some relatively straightforward connections between our model and existing experimental data. In addition, since dislocation models have primarily been developed for strong materials, there are some open issues when it comes to the relatively weak interfaces that one probably has in most real cases of friction. There are also some open questions, for instance when interface dislocations are moving faster than the speed of Rayleigh waves at the interface, which merit further investigation. This discussion presents a collection of tribological phenomena that can be directly understood and explained through this model, as well as some potential topics for future research.

2.7.1. Superlubricity and the Aubry Transition at Incommensurate Contacts

As pointed out some time ago by Aubry [94], for certain special, weakly bonded incommensurate interfaces dislocations dissociate and the nominal static friction coefficient goes to zero. The dynamic friction due to traveling strain fields at the interface will not vanish, so there will still be a contribution although we are not aware of any attempts to apply the established drag models to this specific case. Additionally, in the process of dissociation, a ribbon of stacking faults is created, and may lead to work hardening effects (i.e. some dissipative terms).

The concept of superlubricity, a dramatic reduction of the static friction force, has been the subject of much controversy since its definition [95]. It was shown, albeit not conclusively, in both experiments and simulations that some conditions will lead to a

decrease in the friction force by several orders of magnitude by simply changing the relative orientation of a crystalline contact [96, 13]. The scanning probe study, however, failed to directly measure a normal force, and, strictly speaking, only establishes a tunneling contact. A more careful FFM study by Dienwiebel [2, 12] has shown very low sliding friction forces between graphite flakes under extremely low loads.

The correct definition of superlubricity only accounts for dissipative elements associated with phonons. Radiation friction and electronic drag terms do not necessarily vanish upon forming an incommensurate contact. All real sliding contacts will contain some type of defect, whether it is due to finite size (edge) effects or due to larger scale lattice relaxations that give rise to misfit dislocations. The exact nature of the defect will determine its Peierls barrier that will produce a finite friction force. Even in the case of graphite, where the Peierls barrier in the basal plane has been determined to be $1 \cdot 10^{-17}$ Pa , an exceedingly small but finite friction force exists [88, 97]. This extremely small dislocation barrier in the graphite basal plane suggests that other defects or surface terminating layers play the most significant role in friction for this system. Pinning at the ends containing a dislocation line tension is likely to dominate sliding of layers in graphite. This is considered to be the stress required to multiply dislocations at Frank-Read sources. More directly, our model concludes that for an extremely low Peierls barrier, viscous phonon and electron terms will dominate at all experimentally feasible velocities. The origins of the low tribological properties of graphite must not be viewed as sudden shifts of entire basal planes over one another, but as the incremental propagation of dislocations throughout the interface [97].
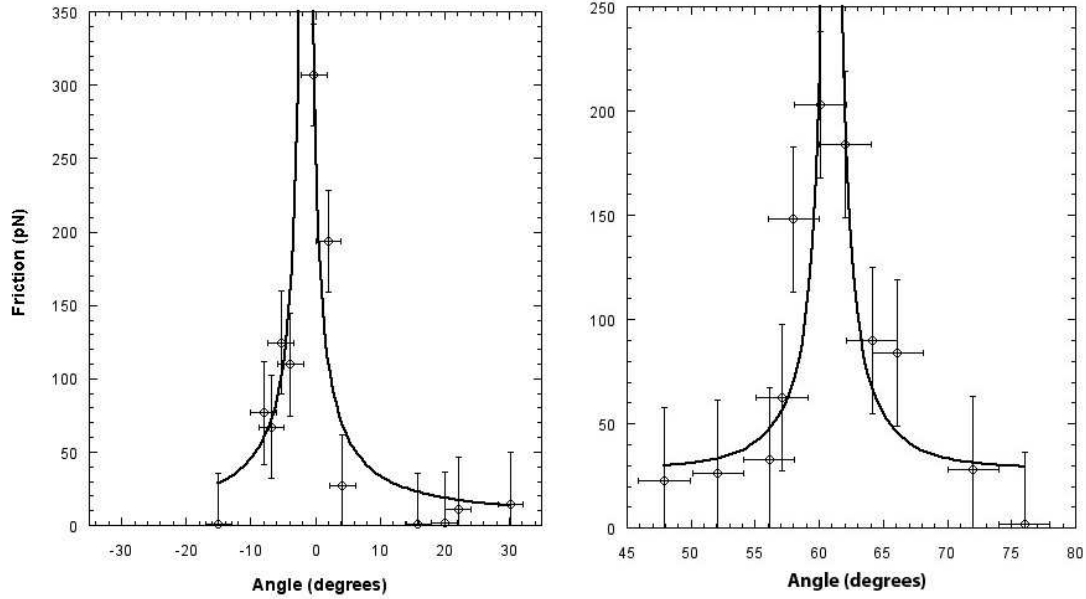
Figure 2.9. Fit to Dienwiebel friction data (graphite-graphite sliding) using the analytical expression for dislocation drag. Fit to the total viscous drag coefficient, B, yields a mean value of 0.0012 ± 0.0001 N·sec·m^{-1}.

A calculation using our model has been carried out to reproduce conditions given in the experiment by Dienwiebel (F_N=18 nN, V=20 nm/sec, R = 80 nm), with shear stress values for single-crystal graphite measured by Soule and Nezbeda [98] ($\sigma = 29$ kPa). We arrive at a $\Sigma 1$ friction range of $\mu = 0.001$ - 0.026 for dislocation spacing limits of 5 and 25 nm. The value reported for Dienwiebel's FFM experiment in the case of commensurate (near $\Sigma 1$) contact, was $\mu = 0.017$, clearly consistent with the calculated results.

It is worth mentioning that for hexagonal CSL orientations there are in other special twist orientations (see Figure 2.10) between 0° and 60°, including $\Sigma 7$ at 38.21°, $\Sigma 13$ at 27.79°, $\Sigma 19$ at 46.82°, and $\Sigma 21$ at 21.78°. Although much weaker than the commensurate six-fold symmetry, we expect that these peaks could be experimentally resolved. Dissociated dislocations [99] at these orientations will lead to a friction value at least an order of
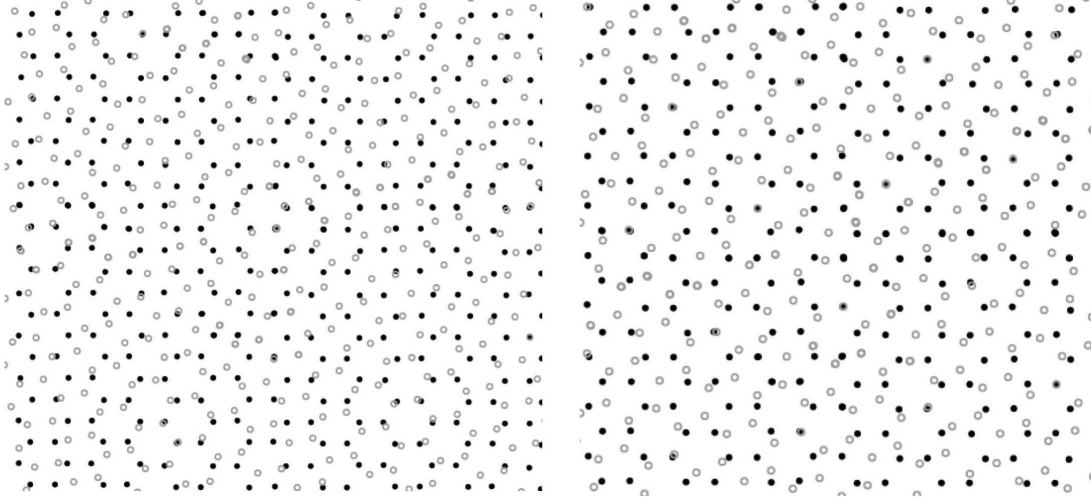
Figure 2.10. Hexagonal CSL showing a 6° misorientation (a) forming a hexagonal network of misfit cores and the Σ7 boundary (38.21°) (b).

magnitude weaker than commensurate contact. The measurements by Dienwiebel et al. show a slight bump at the Σ21 orientation, but the expected friction value is within the associated experimental error. A significant peak is resolved at 50 ±2°, and could reasonably represent the Σ19 boundary. It would be worthwhile to perform this experiment with better force and angular resolution, if necessary at higher normal loads and contact areas.

We can take this analysis one step further by analyzing the experimental data of Dienwiebel to extract fundamental properties of the contact. In performing a fit (Figure 2.9) of the friction peaks at 0° and 60° to Equation 2.15 and accounting for all experimental and contact parameters including sliding velocity, partial dislocation structure and materials constants, we can give an estimate of the effective viscous drag coefficient and Peierls stress for the contact. By using a 600 $\mathring{A}$ sliding flake, fits to both peaks yield an average value of 0.0012 $\pm$ 0.0001 N·sec·m^{-1} for B. Since the sliding conditions are within the

viscous drag regime, the fits are somewhat insensitive to the value of the Peierls stress, but an order of magnitude fit places it at 1 Pa. We acknowledge that in this analysis, a simple estimate was used to account for the finite size effects of the graphite flake by solving for a fraction of a dislocation. This is not generally correct, and remains an active field of research, particularly in the investigation of dislocation-mediated deformation of nanograined materials. Experiments have shown [100] that nanoparticles forming twist boundaries with a crystalline substrate rotate to form commensurate contact in a thermally activated process, while molecular dynamics simulations [101] have indicated that for particles smaller than 5 nm this phenomenon occurs athermally. A significant amount of additional work must be carried out to complete the analysis of smaller contacts, identifying the precise structure of dislocations at nanometer-sized grain boundaries, but we believe that this order of magnitude estimate is nonetheless useful; the principals of the model do not change, only the specific dislocation structure. We note that Dienwiebels experiment represents the most sensitive and thorough set of experimental data for any system in regards to friction aniosotropy at the nanoscale. However, in order to more accurately fit the anisotropy peak widths to the present analytical model for dislocation friction, at least an order of magnitude improvement in force resolution must be made to the experimental data. This can be achieved in part by increasing the normal load, taking care not to increase to the point where the flake detaches from the tungsten tip.

A recent study by Park *et al.* [102] has shown strongly anisotropic friction forces on the surface of a decagonal Al-Ni-Co quasicrystal. This unique surface attains periodicity in one direction, while in another it is quasiperiodic, following the stacking sequence of Fibbonacci. It was found that friction increases by a factor of eight in the periodic

direction as compared to the quasiperiodic direction. We believe this experiment has convincingly isolated the issue of the role of periodicity on friction, and can be explained by the behaviour of dislocations. By maintaining a constant contact orientation, the sliding direction was changed, meaning that the initial interfacial dislocation structure was essentially unchanged. Only the motion of interfacial dislocations behaves differently. While sliding in the periodic direction, regularly spaced dislocations with Burgers vectors along the direction of motion experience a drag force. When sliding is performed in the quasiperiodic direction, the dissociated aperiodically spaced dislocations are now the only remaining contributors to drag, resulting in a greatly reduced friction force. To further prove this, sliding could be performed as a function of load. At some load the Aubry transition would be crossed, the dislocations would become localized, possibly leading to a discontinuous jump in friction.

2.7.2. Supersonic Dislocations

One area where there might be some new effects is the regime where dislocations are moving at close to or above the local speed of sound. The governing elastic equations are analogous to the equations of relativity, with the local speed of sound replacing the speed of light in vacuum, with the exception that physically realistic solutions do occur above the speed of sound. Elasticity theory for dislocation drag has solutions for supersonic motion, but at stresses that significantly exceed critical yield stresses of materials when the shear wave velocity is approached. More recent atomistic models have shown that sustained supersonic dislocation motion is possible given a supersonic starting condition [103]. At an interface, particularly a relatively weak one, the interfacial speed of sound

(corresponding to Love or Rayleigh waves) can be easily exceeded, and there might well be new physical phenomena.

2.7.3. Superconducting Transition

The effect of superconductivity on friction has recently been studied in systems of sliding monolayer films on lead substrates using a quartz crystal microbalance (QCM) [25, 26]. Dayo et al. presented evidence of a sudden decrease in friction for N_2 films sliding on Pb substrates as the superconducting transition is crossed. In an attempt to reproduce this experiment, Renner et al. observed a pinned film, with no slip occurring at any of their experimental conditions. It was concluded by the authors that slight differences in laboratory conditions (humidity and substrate preparation consistency) are to blame for the disparate results [26]. In the viewpoint of our model, both results are valid, and even predicted. In the case of the pinned film, the Peierls relief barrier is sufficiently large so that the effects of electronic drag are not measured. This can result from the presence of dislocations or steps at the interface, which can act as dislocation sources as discussed later in this work, and is within the error of sample preparation techniques. A step free interface will not include these additional barriers, enabling slip and the measurement of the friction force.

At low temperatures phonon modes are frozen out, allowing electronic drag contributions to play a more significant role. However, when the superconducting transition is crossed, the number of electrons interacting with dislocations is substantially smaller. It has been shown both theoretically [71] and experimentally [66, 68, 69, 70] that the plastic properties, namely dislocation drag, are greatly affected by crossing the superconducting

transition. Detailed mathematical expressions for the form of drag can be found in works by Kaganov and Natsik [104] and Huffman and Louat [71]. Interestingly, for the case of dry friction, these calculations demonstrate that for $v \ll v_c$ the electron drag coefficient B_e is no longer constant under the superconducting transition temperature, but follows the temperature dependence of the normal electron density. This was confirmed experimentally by Kobelev and Soifer [105] in a bulk material, and is worthy of further investigations regarding solid friction experiments at low temperatures.

2.7.4. Transfer Layers and Third Bodies

In the large majority of cases, one must allow for the existence of third body sliding in the analysis of most friction experiments. In the present context of dislocation-mediated friction, a third body can be modeled as two sliding interfaces rather than one, each interface (and the respective interface dislocations) moving at half the speed. In the high velocity regime of our model the net dissipative force will be unchanged, but in the lower velocity regimes it will be increased by a factor of two, assuming a constant density of dislocations. Of course, if the third body has a substantially lower Peierls stress then the dominant sliding mechanism will be via dislocations standing off from the interface. This well-characterized phenomenon [106, 107, 108] can be directly applied to solid friction experiments, correlating wear of a transfer layer to the stand-off distance of dislocations during sliding. Mader and Knauss have shown in both experiment and theory that dislocation standoff for the metal-oxide interface between Nb and Al_2O_3 is between 1.8 and 4.0 d(110) spacings. For materials with highly dissimilar shear moduli, it is not unreasonable to have standoff distances exceeding 20 planar spacings. In our model this

would correlate with the width of transfer layers. This we consider to be a relevant wear mechanism for solid lubricants (graphite, MoS_2).

2.7.5. Superplasticity

Grain boundary sliding refers to the displacement of individual grains past one another when a sufficient external stress is applied. This is equivalent to all the misfit dislocations at the boundary moving collectively, as against single dislocation motion. The relative motion of the grains can take place immediately at the interface, or at some small standoff distance (e.g. buffer layers) from the boundary. In bulk materials this type of deformation process leads to what is called superplasticity where plastic strain elongation can reach several hundred percent (even up to 1000%) before failure. Two basic conditions are required to achieve superplastic behavior: (1) grain sizes typically less than 10 μm and (2) high temperatures, usually at least half of the melting temperature. In nanocrystalline materials grain boundary sliding is often the dominant mode of deformation. It has been shown by internal friction experiments that twist boundaries with higher energy are more susceptible to grain boundary sliding than those with low Σ indecies [109], which is analogous to our model.

We will speculate that a similar phenomenon may be responsible for some solid lubricants at elevated temperatures; at lower temperatures, we expect superplastic effects to occur for polymers or self-assembled monolayers. These processes (in the bulk) are often thermally activated, so a careful analysis of the temperature dependence could potentially prove (or disprove) our hypothesis.
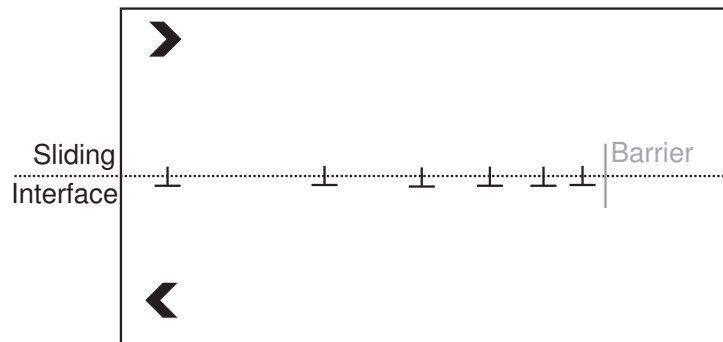
Figure 2.11. Dislocation pileup occurs when a barrier prevents the passage of a dislocation, leading to bunching of dislocations held apart by interdislocation forces.

2.7.6. Work Hardening, Pileup and Dislocation Sources

It is interesting that the dislocation model will give a form of stick-slip behavior at a more nanoscale level, as against at the atomic level. Orderly motion of dislocations as we have assumed (for simplicity) rarely occurs in practice, instead one often gets what are called dislocation tangles or pile-up (Figure 2.11) due to the effects of barriers in the material. For the case of friction this would be anything from surface steps to surface impurities. As the dislocations become entangled, the density of dislocations increases and the stress to move them becomes higher, what is called cold work; this is a bulk phenomenon, but we see no reason why it should not also occur at an interface. The higher stress level required to move the dislocations can lead to a different path for sliding to become activated, in effect a stick-slip process. It is reasonable to expect the edges of contact to contain dislocation barriers or sources. These edge effects dictate how dislocations move and interact throughout the bulk contact area. Changing the area-to-circumference ratio will result in an additional perturbation from the friction-area relationship.
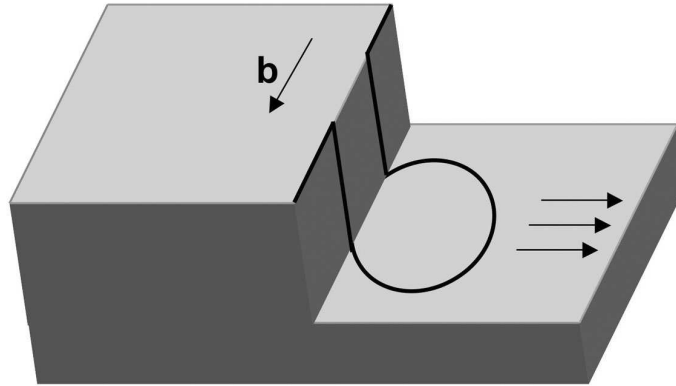
Figure 2.12.   Koehler dislocation source

Since intrinsic grain boundary dislocations can be pushed out of an interface by applying a shear stress (in this case, sliding), sources for additional dislocations must exist to maintain a dynamic friction force. Steps on a crystal surface can act as sources of dislocations, via the Koehler mechanism [110]. Similar to a Frank-Read source [111], this process of moving a screw dislocation to an intersecting plane (cross-slip) can lead to the multiplication of dislocations as drawn schematically in Figure 2.12. Pile-up of dislocations will result, preventing further motion in the slip plane. The angular distribution of Burgers vectors is changed by this process, altering the anisotropic behavior of the retarding force.

2.7.7. Nonmetallic Friction

Covalent materials typically have Peierls stress values many times higher than for metals. Experimentally, however, lower friction forces are measured for nonmetals than for metals in almost every case. Buffer layers and dislocation standoff explain this discrepancy. The formation of native oxide layers or passivation layers at surfaces changes the magnitude

in which interfacial dislocations interact to produce a drag force. Small standoff distances from an interface, on the order of Angstroms, may cause a decrease in the drag stress, since the dislocation now rests in the softer material. Also, native passivation layers are typically amorphous, which can more easily lead to incommensurate contact conditions, known to decrease friction [42, 45, 2, 92, 24].

2.8. Conclusions

We have developed an analytical friction model by combining theories of interfaces, dislocations, and contact mechanics. Using no adjustable parameters, only basic materials constants and given experimental conditions, we demonstrate agreement between magnitudes of calculated friction values and experimental UHV friction data indicating that dislocation motion is an important mechanism in the analysis of crystalline sliding contacts. The model directly addresses temperature, velocity and anisotropic dependence, showing that friction behaves analogously to how dislocations are affected by these factors. A number of tribological phenomena may be understood through this model, including superconducting friction, supersonic dislocation motion, buffer layers and dislocation stand-off as an atomic wear mechanism, superlubricity and the formation of work-hardened tribolayers from dislocation pile-up at Koehler sources. Ample room remains to exploit the suggested phenomena through experiments at temperature and velocity extremes and for crystalline friction.

2.9. Future Work

Despite accounting for a wide range of materials and finding substantial agreement with tribological phenomena, all the mechanisms associated with dislocation motion have

not been presented here. Here we list extensions to this work that merits attention in the future:

- The effect of dislocation motion at high temperatures over time may be accounted for by creep models.

- The effect of very fast dislocations can be incorporated in a more detailed manner, where exotic dislocation motion may lead to new friction phenomena.

- A more robust solution for radiation friction requires an analysis of edge dislocations, making it possible to extend the analysis to any mixed type of interface including tilt and twist components. This requires solving a closed form analytical relationship for radiation friction of edge dislocations.

- Friction calculations for a heterogeneous interface would be useful especially in comparison to experiments where the preparation of a heterogeneous interface is not always possible.

- Many of the model's predictions may be tested on self-assembled monolayers where Peierls barriers are low enough that the transition from radiation friction to viscous drag friction may be monitored as functions of anisotropy, temperature and velocity.

- A system on which to test the velocity dependence of the model is needed. This requires an enormous range in velocities, spanning several orders of magnitude. Identifying the transition from radiation friction to viscous sliding would be key evidence in support of this model.

- This model may be extended in detail to include the effect of third bodies, by modeling them as another material. This would introduce additional layers of

dislocations, for which the interdislocation interactions would need to be worked out. Two sliding interfaces would likely need to be considered.

- Interdislocation forces have not been considered to first approximation in the model here. When pileup occurs at step or other barriers, these forces need to be considered.

This work is viewed as a first step in implementing real materials deformation analyses to computational models in tribology. Since fundamental materials properties are now the limiting factor in the performance of sliding systems, it is most appropriate that interdisciplinary ideas such as the ones presented here are cross-fertilized to benefit the tribological community.

CHAPTER 3

Friction Anisotropy of Cubic Single Crystals

3.1. Friction Anisotropy

Numerous studies have shown that friction forces between single crystals vary as a function of sliding direction or misorientation. However, a complete explanation of the origins of friction anisotropy is lacking. Which plays a more dominant role: surface lattice commensurability or subsurface plastic slip? Strong evidence exists in the literature for both. The real answer is (as always): it depends. Here we will summarize some work that has been reported for crystalline sliding interfaces.

Enomoto and Tabor showed that for a diamond pin sliding over a diamond (100) substrate in ambient conditions, friction is greater in the $< 100 >$ direction than it is along $< 110 >$ [112]. This effect was seen to increase with load, and disappeared at lower loads, where plastic deformation was no longer observed. They concluded that frictional anisotropy was largely due to subsurface damage. Likewise, Ko and Gellman demonstrated that friction between Ni(100) surfaces in UHV was smaller at $\pi/4$ lattice misorientations, for both atomically clean surfaces and surfaces with 4 monolayers of ethanol [78]. At 28 monolayers of ethanol, this effect was no longer detected. They concluded that lattice commensurability could not be the only source of friction anisotropy

when plastic deformation occurs. Mancinelli and Gellman later corroborated these findings with Pd(100) surfaces, detecting anisotropy with as much as 12 monolayers of octane on the surface [113].

Several anisotropy studies have also been performed on flat hexagonal crystals (graphite, mica, molybdenum disulfide). McGuiggan and Israelachvili showed with a surface force apparatus (SFA) that friction and adhesion forces vary with the crystallographic symmetry of flat mica surfaces in water and aqueous KCl, but not in air [114]. The interaction potential between the misoriented surface lattices was believed to be responsible. Hirano *et al.* found in a pin-on-disk study that friction between single-crystal mica surfaces varies as a function of misorientation (twist) angle and follows the hexagonal symmetry of the mica lattice [92]. Maximum forces were measured at coincident orientations, while minima occurred at 30° from commensurate. This effect was seen when adsorbed water or other airborne species had desorbed after heating the interface to 130°C . Graphite surfaces were recently investigated at ultra-low loads by Dienwiebel *et al.* on a home-built AFM tribometer [2, 12]. They, too, observed high friction at commensurate orientations, separated by 60° . Extremely low friction forces at incommensurate orientations were considered by the authors to be evidence of superlubricity. In a pin-on-disk study on Si (111) surfaces, sliding direction was shown to affect the friction force by more than 50 %, with $\pi/3$ periodicity [115]. Sheehan and Lieber characterized sliding between two dissimilar crystalline materials by AFM. Their study identified an order of magnitude difference in the energy per unit area required to slide MoO_3 nanocrystals on a flat MoS_2 surface, when sliding in different directions [116].

Loads and contact radii in the above-mentioned experiments range from nanonewtons and tens of nanometers to newtons and hundreds of micrometers. Some cases show no effect on changing the sliding direction or misorientation angle, while some conditions lead to an anisotropic increase by 1-2 orders of magnitude at commensurate orientations.

Numerical simulations of sliding crystalline surfaces have also been carried out. Diestler *et al.* have shown that the static friction force varies by up to two orders of magnitude as a function of sliding direction for a simulated one-atom tip sliding across a hexagonal close-packed surface [117]. Larger, more realistic contacts have been studied by molecular dynamics (MD), and have indicated that incommensurate orientations can only give rise to finite static friction values by the inclusion of third bodies [32]. Another MD study by Qi *et al.* simulated Ko and Gellman's Ni(100) interfaces and determined that small amounts of roughness (0.8 $\mathring{A}$) lead to agreement with the experimental anisotropy results [93]. For perfectly flat crystals, however, the difference between incommensurate and commensurate sliding increased dramatically, as predicted by a number of analytic theories [28, 33, 94]. No interfacial dislocations were observed, but the short time and length scales at which these MD simulations act would make this unlikely.

Taking what we have learned from the analytical model developed in Chapter 2, we would like to probe anisotropic friction in a new way. Anisotropic friction forces may arise from commensurability and subsurface slip effect, but we believe there may be more information observable between major commensurate orientations. Specifically, we seek to identify changes in friction at major CSL orientations, where commensurability is finite, but not as large as perfect registry. Few investigations have systematically studied

anisotropy with the angular resolution required to resolve low index CSL boundaries. Figure 2.8 and Frank's formula suggest that the width of these peaks may be on the order of one degree. This, however, is a function of the contact size and velocity dependence of the friction mechanism. Here we will investigate the anisotropic friction properties of macroscopic contacts between (100) cubic single crystals with an angular resolution of one degree or less. The experiments are performed on a pin-on-disk apparatus and nanoindenter, in ambient conditions, and not by AFM. Although AFM techniques allow one to measure elastic friction forces, the tip material is often uncontrolled for the purposes of a crystalline solid-solid friction experiment. Most if not all commercially fabricated AFM probes have an amorphous tip composition (silicon, silicon nitride). Thus, creating a well-defined crystalline interface becomes problematic with the use of AFM probes. An exception to this has been the highly contested work by Hirano *et al.* , reporting the first experimental observation of superlubricity, where a oriented crystalline tungsten STM probe was used [96]. Finite size effects of a crystalline contact are a major consideration, since interfacial dislocation structure and motion is not well defined under these conditions. For the purposes of the present investigation, it is required that each counter face be of the same crystalline structure and orientation.

3.2. (100) Friction Anisotropy Measurements

3.2.1. NaCl

Sodium chloride single crystals were cleaved along the (100) planes, exposing a fresh surface with reasonably large flat areas between surface steps. Typical surface roughness of samples prepared in this way was on the order of 1 nm RMS (Figure 3.1). The pin
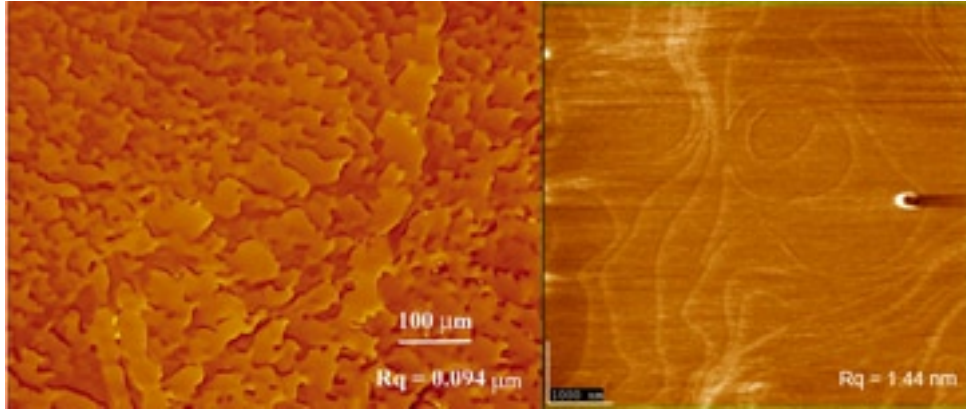
Figure 3.1. White light interferometer roughness image of the polished pin (left), and an FFM image of a typical freshly cleaved NaCl surface.

was cleaved from a smaller piece of NaCl, and polished using deionized water and a silk polishing cloth. This was necessary in order to eliminate edge effects, where a slight misalignment of two flat surfaces could cause an edge of the smaller surface to dig into the flat, creating an entirely different sliding condition. The pin material was polished to a radius of curvature of approximately 1 cm, and was measured by white light interferometry to have a surface roughness of 94 nm RMS (Figure 3.1).

The CETR-UMT Microtribometer pin-on-disk apparatus was used to conduct the sliding experiments. The disk element of a pin-on-disk apparatus is traditionally used to initiate sliding and to determine the sliding velocity. In this case, however, a modification was made so that the rotating disk determined the misorientation angle between the crystals, while the positioning motor of the pin dictated the sliding speed and duration. The pin and sliding substrate were mounted and the twist orientation of the pin relative to the substrate was aligned optically by the crystal's macroscopic cleavage planes. The error with this alignment proceedure is estimated to be 2-3° . The relative orientation of the two (100) crystals was initially adjusted to be near the $\Sigma 5$ boundary orientation

(36.87°). A sweep through and angular range of 10° about this orientation was performed twice - once counter-clockwise, once clockwise. This resulted in two independent sets of data for each orientation. All friction measurements were performed at a load of 120 mN and sliding velocity of 20 μ/sec, giving a Hertzian contact pressure of approximately 50 MPa. Seven sliding passes were performed at each orientation in a consecutive line making sure that a fresh sliding surface was exposed to the pin for each pass. Steady state kinetic friction forces were recorded for each sliding event and averaged per orientation. The relative humidity was 20-25% for the duration of the tests.

Two peaks in the friction force were observed both for the clockwise and counter-clockwise directions (Figure 3.2). The spacing between peaks was consistent, and if we assign the leftmost peak to the $\Sigma5$ (36.87°) orientation, we can identify the peak on the right as the $\Sigma53$ (31.89°) orientation. The measured spacing of $5° \pm 0.5°$ agrees with the expected spacing of 4.98° . The next smallest major sigma configuration for (100) cubic twist boundaries occurs at 28.07° ($\Sigma17$), 8.8° fewer than $\Sigma5$.

The variation in friction force is relatively smooth, but only corresponds to a change of 10-15 %. This, however is well within experimental error of the measurements. This is by no means conclusive evidence, but the results do suggest that more experimentation would be helpful. Unfortunately, a comprehensive anisotropy study sweeping through a larger angular range was not performed, due to the occurence of technical problems with the sensor (noise and environmental control). Also, the NaCl surface is very sensitive to humidity, and somewhat rougher on the pin surface than we would like. For these reasons, a new cubic system was chosen, and is described in the following section.
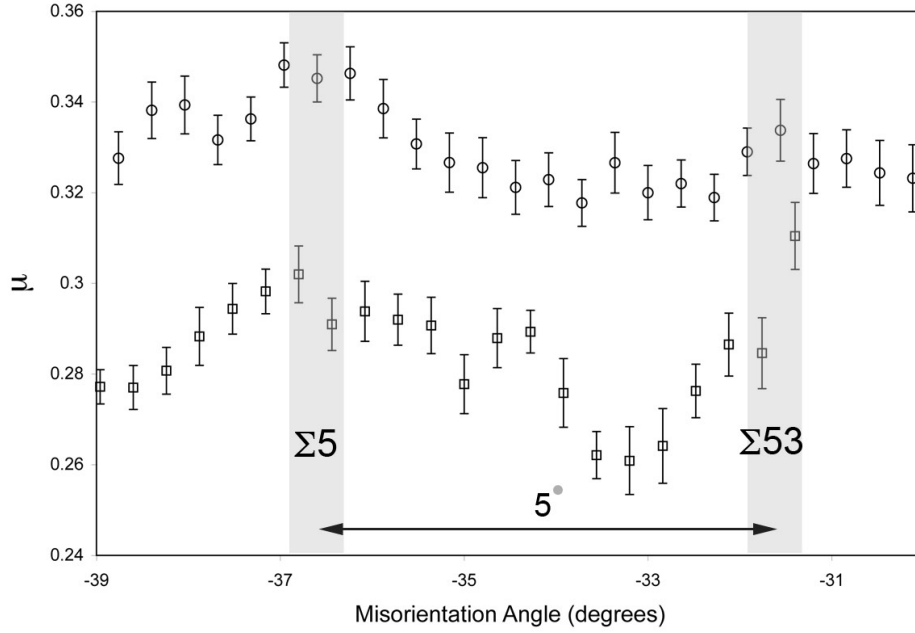
Figure 3.2. Friction as a function of misorientation angle for (100) NaCl single crystals. The two plots represent independent sets of measurements at the same orientation.

3.2.2. SrTiO₃

Further anisotropy experiments were conducted at Hysitron Inc. (Eden Prairie, Minnesota, USA) on highly polished $SrTiO_3$ single crystal surfaces oriented in the (100) direction, using the Hysitron's UBI-1 Nanomechanical Test Instrument equipped with a three-plate capacitive force transducer. Both the substrate and sliding pin were of the same material, orientation and roughness. In order to satisfy the geometric and weight requirements of the UBI-1 system, the crystal was machined to an equilateral flat with sides of 50 μm, leaving the epipolished surface unaltered. This geometry reduced the chance of edge artifacts being introduced in the form of burrs or chips. AFM and profilometry
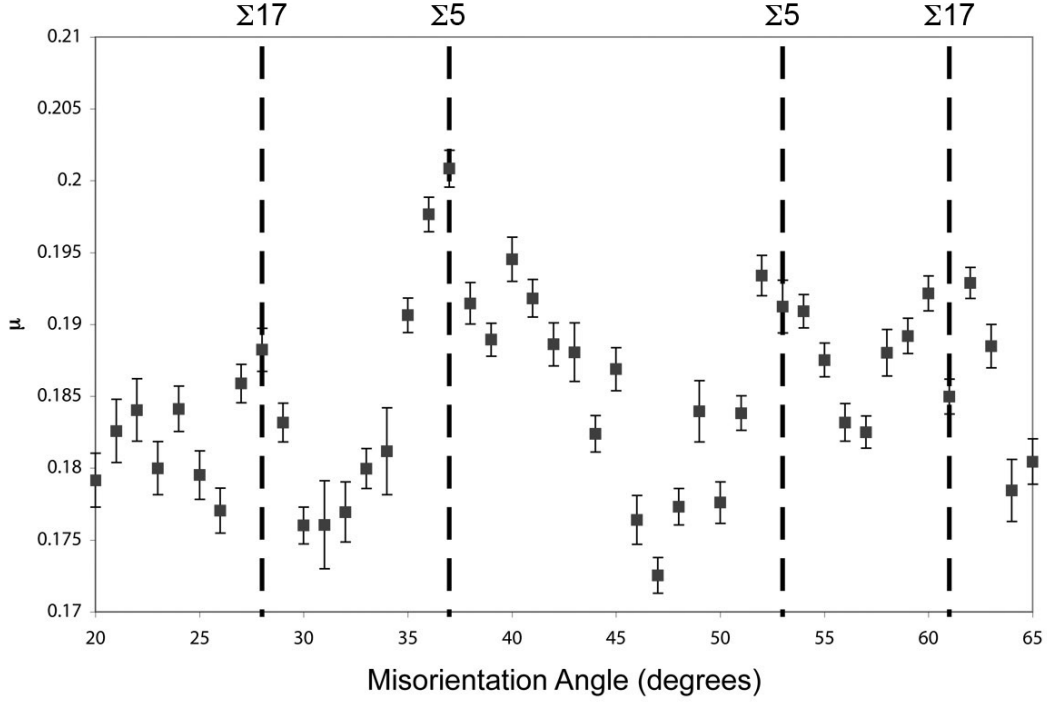
Figure 3.3. Friction as a function of misorientation angle (arbitrary) between single crystals of SrTiO$_3$ (100).

roughness measurements determined the RMS roughness to be 3 $\mathring{A}$ for both the tip and the sliding substrate.

The sample was mounted on a 360° rotation stage to easily allow for the twist angle to be changed between the tip and sample. Friction forces were measured at a constant velocity and sliding direction (1 μm/s over 10 μm) as a function of an in-plane twist misorientation of the two crystals through 100 degrees. Measurements were conducted at room temperature with a constant relative humidity of 18%.

Average friction values were tabulated for each orientation, and are plotted in Figures 3.3 and 3.4. Figure 3.4 shows a strong Σ1 peak, representing an increase of 45% over the incomensurate region to its immediate left or right. The spacing between resolved peaks
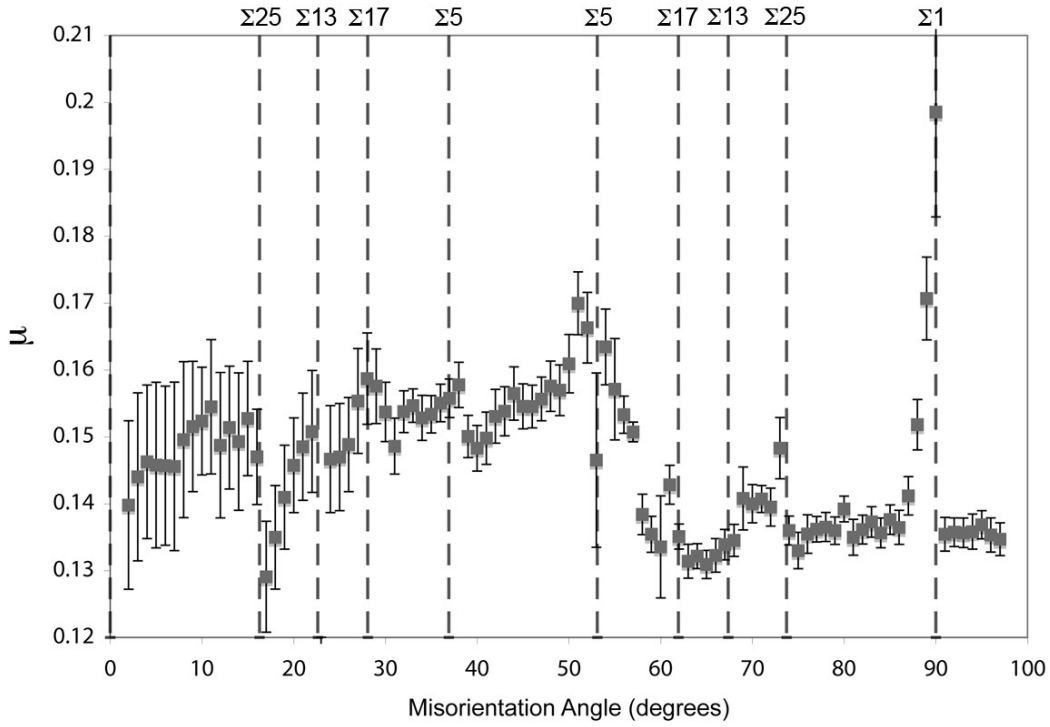
Figure 3.4. Friction as a function of misorientation angle (arbitrary) between single crystals of SrTiO$_3$ (100).

can be compared to spacings between major CSL (100) twist boundary configurations. Figures 3.3 and 3.4 superimpose the expected positions of the major CSL boundaries, where minor anisotropic effects are expected if commensurability and/or interfacial dislocations are significant contributors under these sliding conditions. Although not all major boundary peaks are resolved, a number of peaks do appear consistent with the expected distribution of major sigma boundaries (Table 2.2.1). While the behavior is subtle, and by no means definitive, this data can give us an idea of the upper bound to anisotropy resulting from grain boundary-like interactions.

3.3. Discussion

The friction data shows some interesting variation with the relative orientation of cubic single crystalline tribo-contacts. A number of the expected intermediary CSL boundary orientations exhibit indications of a local rise in friction, but these features are often dominated by global trends, likely the result of third bodies, and surface roughness. This makes it necessary for us to consider the relative contributions of different friction mechanisms at a crystalline sliding interface. Energy dissipation may result from commensurability effects, subsurface slip, third bodies (adsorbed species, transfer layers) or more complex plastic deformation mechanisms. If the variations in friction we have detected in both the NaCl and $SrTiO_3$ anisotropy experiments are due to surface lattice commensurability, we then have a means to place bounds on this effect. The variation in magnitude from maximum to minimum for $SrTiO_3$ was 15-25%, with the exception of the $\Sigma 1$ peak observed in Figure 3.3. For NaCl, the valley-to-peak variation was, 10-15%. All of our measurements, taken in ambient conditions (RH < 25%) can most accurately be compared to Ko and Gellman's and Mancinelli and Gellman's results [78, 113] for Ni and Pd interfaces with 28 monolayers of ethanol or 40 monolayers of octane passivation. Their data at these passivation levels failed to show any evidence of anisotropy, claiming the crystalline metal surfaces were no longer aware of each other's periodicity. However, the experimental error in their experiments are quite high ($\pm$ 30-40%) - a practical compromise of having to design an operable tribometer in UHV. With our experiments, we have improved the angular and force resolution, while sacrificing control of surface adsorbants.

The results of Enomoto and Tabor on diamond show a high amount of anisotropy, giving $\sim 60\%$ peak-to-valley variation for high loads with an 18 μm stylus. The contact

pressures in this case greatly exceed ours - ~ 20 GPa compared to our sub-GPa elastic tests. A basic Hertzian estimate of their contact conditions lead to the conclusion that no anisotropy is observed under ~ 15 GPa. This clearly agrees with the idea that surface adsorbants can dominate anisotropic friction effects unless high enough pressures are achieved to reduce their thickness. Table 3.3 summarizes the findings of a number of anisotropy experiments, as a function of contact pressure (as a simplified Hertzian area), environmental conditions and the error associated with friction measurements, both static and kinetic.

While the results of our study show anisotropic friction variation to within 10%, it is unlikely that any real dislocation motion occurs at room temperature in $SrTiO_3$. However, the data do succeed in providing an upper limit to anisotropic forces due to lattice commensurability in ambient conditions.

3.4. Conclusions

Highly suggestive anisotropic behavior was observed between cubic single crystals (NaCl and $SrTiO_3$) at fine angular resolutions corresponding to major twist CSL boundary orientations. This is an indication that surface lattice commensurability plays a role in determining friction properties at elastic contacts to within a range of 10-15% variation in the friction force. More significantly, this supports the idea of a richer anisotropic behavior between sliding single crystals, and is consistent with the predicted behavior of moving dislocations at twist grain boundaries. This result, we believe to be due to the fact that we have operated at low enough pressures to stay largely in the elastic regime, where surface commensurability is expected to dominate over subsurface plastic slip. Although

Table 3.1. Comparison of anisotropic friction studies for contact pressure (p), environmental conditions and crystal structures. NaCl and SrTiO$_3$ refer to the results in this study.

	p (GPa)	Environment	Anisotropy?	μ_{peak}/μ_{valley}	Error ($\sim \%$)	Ref.
Diamond	11	ambient	no	–	3.6	[112]
	13.9	ambient	no	–	5	
	14	ambient	yes	1.26	3	
	17.5	ambient	yes	1.30	7	
	17.5	ambient	yes	1.42	4	
	22	ambient	yes	1.53	7	
Graphite	2.46	ambient	yes	16	10 (peak) 100 (valley)	[2]
Ni	0.054	4 ML ethanol	yes	2.50	31	[78]
		28 ML ethanol	no	–	35	
STO	*	18 RH	*	1.17	1	
NaCl	0.03	ambient	*	1.1-1.15	1.8	
Mica		20°C	no	–	5	[92]
		130°C	yes	3.4	11	

greater distinction between anisotropic peaks have been observed elsewhere, none have attempted to show it at as fine an angular resolution for cubic single crystals as in the present study. In order to isolate the major commensurate peaks, this experiment should be performed at higher temperatures, lower pressures (UHV), at higher loads, or a combination thereof. Nonetheless, the results here are encouraging, and further emphasize the complexity of friction processes, namely the dependence on adsorbed species in ambient environments. Operating above 100 °C will de-sorb an amount of water or other hydrocarbon species otherwise present on the surface at ambient temperatures. This reduction in surface contamination was seen to greatly affect the anisotropic friction response in some experiments, notably by Hirano *et al.* [92].

3.5. Future Work

Macroscopic friction experiments that seek to isolate specific nanoscale deformation mechanisms are often challenging and inconsistent, since they are susceptible to an incredible number of factors, including load, temperature, surface preparation, humidity, velocity, roughness, asperity distribution and third bodies. In order to detect the variation in friction between oriented cubic single crystals as a function of twist angle, greater care must be taken with surface preparation techniques and environmental conditions. Since the mechanical properties of cubic single crystals do not easily allow for the convenient fabrication of flat surfaces such as mica or graphite, other surface defects such as surface steps must be accounted for. Surface contaminants play a significant role in either case, with much more conclusive evidence available from experiments in controlled

environments. UHV tribometers offer this additional dimension of control; however, they sacrifice friction measurement fidelity.

There is a great opportunity to repeat these experiments at higher temperatures. Performing these experiments in a dry atmosphere at a temperature above 100 °C , will de-sorb a significant amount of contamination, giving a solid-solid contact not mediated by the properties of the adsorbed lubricating layer. If performing these experiment at high temperatures presents practical experimental problems, the load may be increased incrementally until the thickness of the adsorbed layer is reduced sufficiently. At which point an increased load excites subsurface effects, with or without the presence of adsorbants, remains unknown. This can be detected if the right experimental conditions are met - something which is in principle possible with current technique, but would be exceedingly difficult and time-consuming.

CHAPTER 4

Graphitic wear observed by *in-situ* TEM

The following three chapters will describe in detail a series of *in-situ* TEM tribology studies on graphite, gold and amorphous carbon surfaces, respectively. The goals of these studies are to directly observe and characterize sliding interfaces with the intention of identifying real structure-friction relationships.

4.1. Experimental Nanotribology and the Blind Interface

Experiments in tribology have long suffered from the inability to directly observe what takes place at a sliding contact - the classic buried interface problem. Sliding interfaces have been studied in a detailed manner by atomic force microscopy (AFM), quartz crystal microbalance (QCM) and surface force apparatus (SFA) techniques, and although these methods have identified many friction phenomena on the nanoscale, many of their interpretive pitfalls result from indirect or *ex-situ* characterization of contact surfaces.

Nonetheless, many interesting friction phenomena have been discovered through the use of *ex-situ* techniques, including stick-slip behavior [11], superlubricity [2, 12, 13, 96], anisotropy [2, 92, 78, 93, 112], and velocity dependence [14]. Mate et al. [11] showed that a scanning tungsten probe gave atomic-scale features when sliding across the basal plane of a graphite surface at forces below 10^{-4} N. Later studies showed atomic stick-slip behavior on other materials, including Mica [15], Cu [16], NaF [17], and Diamond [19]. For

larger micron-sized contacts between flat mica samples, Hirano et al. demonstrated that the friction force varies strongly with the in-plane orientation (misfit) between crystalline surfaces [92]. The friction force was observed to change by a factor of four and displayed periodicity consistent with that of the hexagonal symmetry of the mica lattice. Graphite sliding interfaces were shown by Dienwiebel et al. to exhibit similar anisotropic behavior at very low loads[2, 12]. This study, in particular, forms the basis of our first *in-situ* TEM investigation of sliding interfaces.

I. Singer addressed the most pressing issue in friction and energy dissipation at the atomic scale in his 1994 review article [118]:

> *Discussions of energy dissipation during friction processes have captured the attention of engineers and scientists for over 300 years. Why then do we know so little about either dissipation or friction processes? A simple answer is that we cannot see what is taking place at the interface during sliding.*

Singer continued to describe how researchers have come one step closer to seeing what goes on at a sliding interface through the developement of experimental techniques (AFM, QCM, SFA) and theoretical simulations (MD), but points out the void in time and length scales between modeling and experiment, making correlations between dynamic processes and interface structure a rather challenging and uncertain task. It is for this reason that new approaches and new instruments are being developed that can simultaneously collect friction and chemical or structural information from a sliding interface. Examples of this type of work include *in-situ* raman spectroscopy [119, 120], x-ray photoelectron spectroscopy (XPS) [121], and electron microscopy [122] tribometers.

4.1.1. *In-situ* TEM for tribological and mechanical deformation

In-situ TEM techniques make it possible to directly observe an interface during sliding in real time without having to rely on *ex post facto* characterization techniques. Remarkable advances in understanding have been made in the materials sciences regarding the deformation of bulk materials via dislocation behavior and microstructural change (e.g. work hardening, creep, dislocation pileup and barriers, and grain boundary motion) through the use of such techniques by implementing *in-situ* heating, cooling, tensile strain, deposition, biasing, and environmental stages. Quite recently there have been significant advances made in nanomanipulation stages, where one is able to locally deform a small region of material much in the same way as conventional scanning probe (AFM, STM) and nanoindentation techniques, while maintaining the ability to directly characterize the contact in real time with the TEM. *In-situ* nanoindentation stages have been used to correlate microstructural changes with mechanical force measurements on the length scale of 100s of nanometers, including the direct observation of dislocation motion and grain boundary migration within the microscope [123]. STM-TEM stages allow one to probe individual sub-micron features electronically and mechanically, and in principal can acquire STM images which can be correlated directly with TEM images. A number of STM-TEM studies have been performed, largely on nanostructures including nanotubes and nanowires, investigating their local mechanical and electrical properties [124, 125, 126, 127].

Our work will take a somewhat different approach, by concentrating on sliding solid-solid interfaces. In doing so, we seek to translate an understanding of fundamental materials deformation to sliding interfaces where little more than a fragmented understanding of

dynamic deformation behavior exists. Forming indisputable relationships between structure and friction is the goal of this research, and through the acquisition of this knowledge, we hope to establish a more unified theory of friction based on mechanistic principals instead of empirical guesswork.

4.2. Tribological properties of graphite

Of the many allotropes of carbon (Figure 4.1), graphite is the most stable and common. Covalently bonded carbon atoms form a hexagonal sheet with a lattice constant of 2.46 $\mathring{A}$, giving rise to high in-plane conductivity. The hexagonal sheets are held together by weak van der Waals forces, forming a lamellar structure that is believed to give graphite uniquely anisotropic mechanical properties. In powder form graphite is often used as a solid lubricant, but despite graphite's good lubricating properties in ambient environments, it fails to perform well under under vacuum, leading to the realization that basal plane coupling is highly sensitive to adsorbed contaminants (water, hydrocarbons, atmospheric gases).

Recently, the effect of crystalline periodicity on the friction properties has been investigated at low load single asperity contacts through the use of a home-built scanning probe tribometer [2, 12]. Extraordinarily low friction forces of 15 ± 15 pN at normal loads between -24 nN and 30 nN were been reported at incommensurate contact orientations, and at commensurate contact geometries, friction was observed to increase by an order of magnitude. This anisotropic behavior is shown in Figure 4.2 [1]. The proposed underlying physical mechanism for this tribological behavior was that a small graphite

---

[1]Reprinted figure with permission from [M. Dienwiebel, et al., Physical Review Letters, 92 (12), 2004]. Copyright (2004) by the American Physical Society.
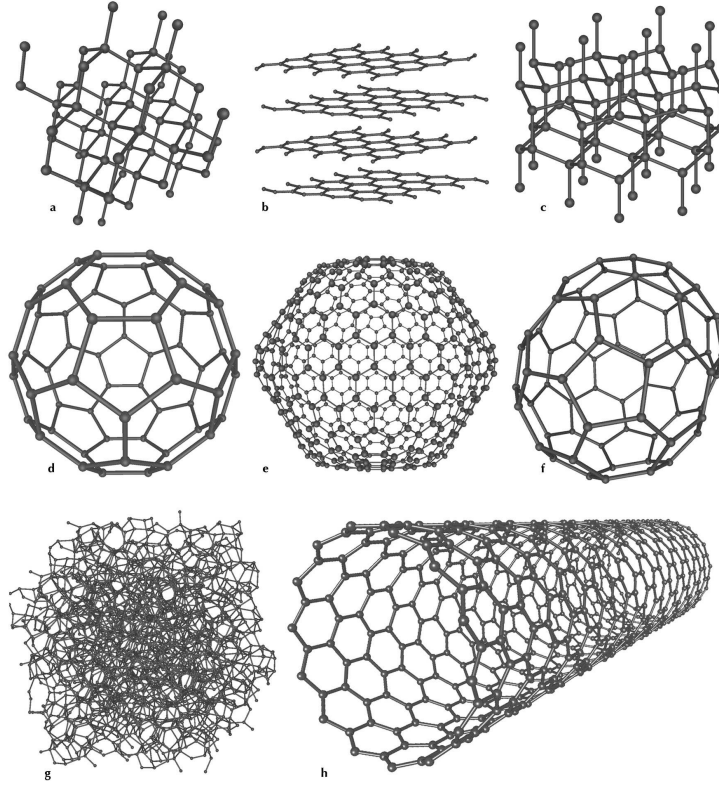
Figure 4.1. Allotropes of carbon: (a) diamond, (b) graphite, (c) lonsdaleite, (d) C60, (e) C540, (f) C70, (g) amorphous carbon, (h) carbon nanotube. (Wikipedia, GNU Free Documentation Licence 2006)

flake from the substrate attached itself to the scanning tungsten probe during sliding, creating a graphite-graphite sliding interface. Despite efforts to perform a postmortem TEM analysis, the authors were unable to confirm the presence of a graphite flake on the scanning probe.

The *in-situ* TEM holder allows us to reproduce the same interface, and image it directly in real time. In doing so, we wish to directly observe whether graphitic flaking and adherence to the tungsten probe occurs during sliding. It is the purpose of the present investigation to directly observe via *in-situ* TEM the graphite-tungsten sliding interface and characterize any observable structure-friction relationships.
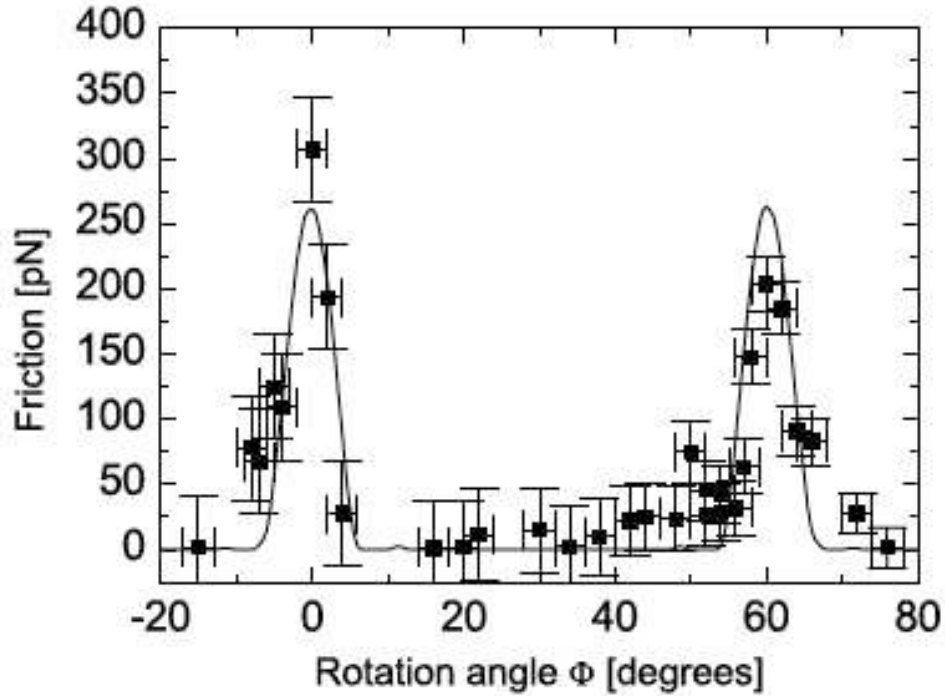
Figure 4.2. Friction anisotropy on graphite surface. Reprinted from [2].

4.3. Experimental details

Highly ordered pyrolytic graphite (HOPG) TEM samples were prepared by a sequential cleaving process to optical translucency. Cleaving was carried out with adhesive tape, which was subsequently removed from the thinned samples by introduction to a series of solutions of toluene, methanol and acetone. The samples were placed on standard copper TEM grids (200 mesh) for mounting onto the *in-situ* stage. Scanning probes were fabricated from 0.25 mm tungsten wire using a standard electropolishing technique in a 1 N NaOH solution biased between 0.1 and 4 V AC. Tip diameters were polished down to a minimum of 2 nm, with most typical radii in the 20-50 nm range. High aspect ratio tip geometries were preferred, as not to interfere with the tilted geometry of the sample.
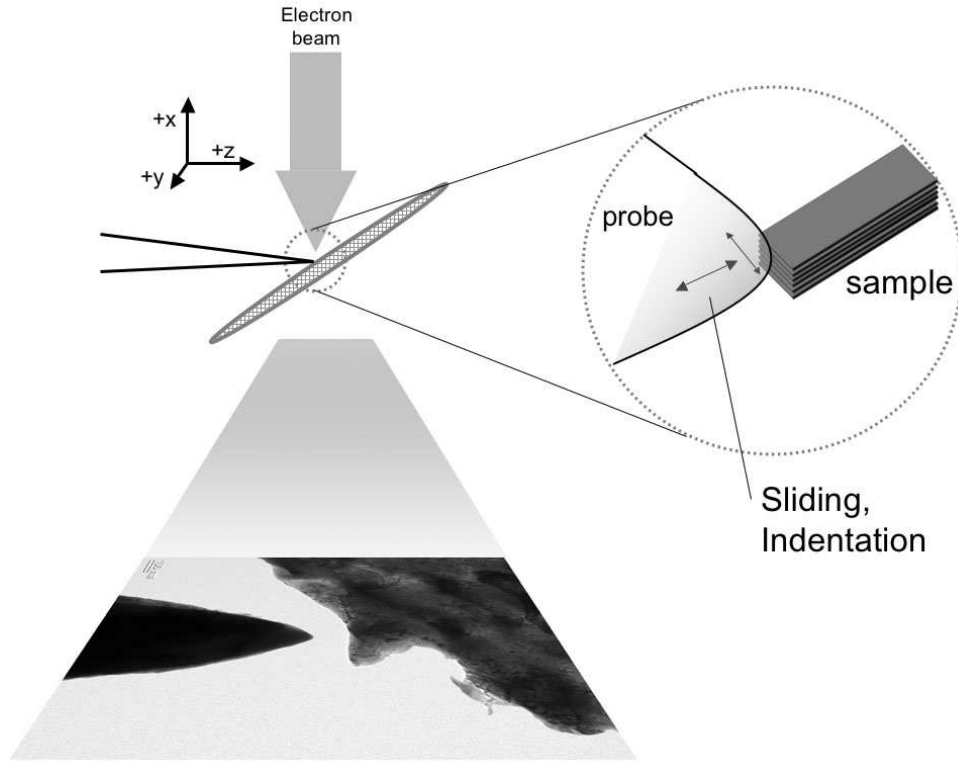
Figure 4.3. STM-TEM holder schematic for sliding on HOPG

The HS100 STM-HolderTM stage used in this study was developed by Nanofactory Instruments (Göteborg, Sweden), and designed for use with a Tecnai F20ST TEM (200kV, Schottky FEG). A simplified schematic of the side-entry holder is shown in Figure 7.1. The tungsten probe is horizontally mounted such that it is orthogonal to the electron beam (-X). The HOPG sample on a Cu grid is mounted at 30 degrees from horizontal, enabling simultaneous exposure and characterization by both the electron beam and the scanning probe. It is capable of course and fine three-dimensional control, with piezo resolutions of 0.2 in XY and 0.025 $\mathring{A}$ in Z. Coarse motion control gives a wide range of motion: $\pm$ 1-2 mm in XY and $\pm$ 1 mm in Z. In addition to nanomechanical control, the stage is capable of electrical characterization and acquiring scanning tunneling topographs. Several practical

considerations arise during operation, particularly in the process of aligning the tip with the sample. First, the axes of the TEM and STM are never perfectly matched implying that motion in Z (approaching sample) will inevitably yield some XY displacement. This is monitored on a coarse scale by modulating the tilt about the Z axis while positioning the tip in order to reduce wobble in the image, assuming the eucentric height is fixed. A finer approach requires measuring the objective lens focus setting and comparing with the Gaussian focus conditions for the scanning probe. A more detailed description of the holder geometry, operation and sample preparation techniques can be found in Chapter 7.

4.4. *In-situ* sliding results

The initial approach with the tungsten probe contacted the sample near its edge. An unavoidable consequence of the tilted sample geometry causes slippage away from the sample edge so that the sliding interface is slightly shadowed by the scanning tip. This occurs when the compliant thin sample bends in response to an applied load by the probe. Increasing the load bends the graphite film by 200 nm (in plan view along Z), and subsequent passes with the slider (100 times) showed evidence of extended wear debris a few nanometers in width, as seen in Figure 4.4. Several wear particles generated by sliding are observed near the edge of the sample. Selected area diffraction patterns have confirmed their composition is polycrystalline graphite.

Upon closer inspection of the wear tracks as seen in Figure 4.4, ordered graphitic planes were observed in the range of 5-35 basal plane spacings (2-15 nm). The planes are not all continuous, clearly showing local defects and bending. The observation of graphite
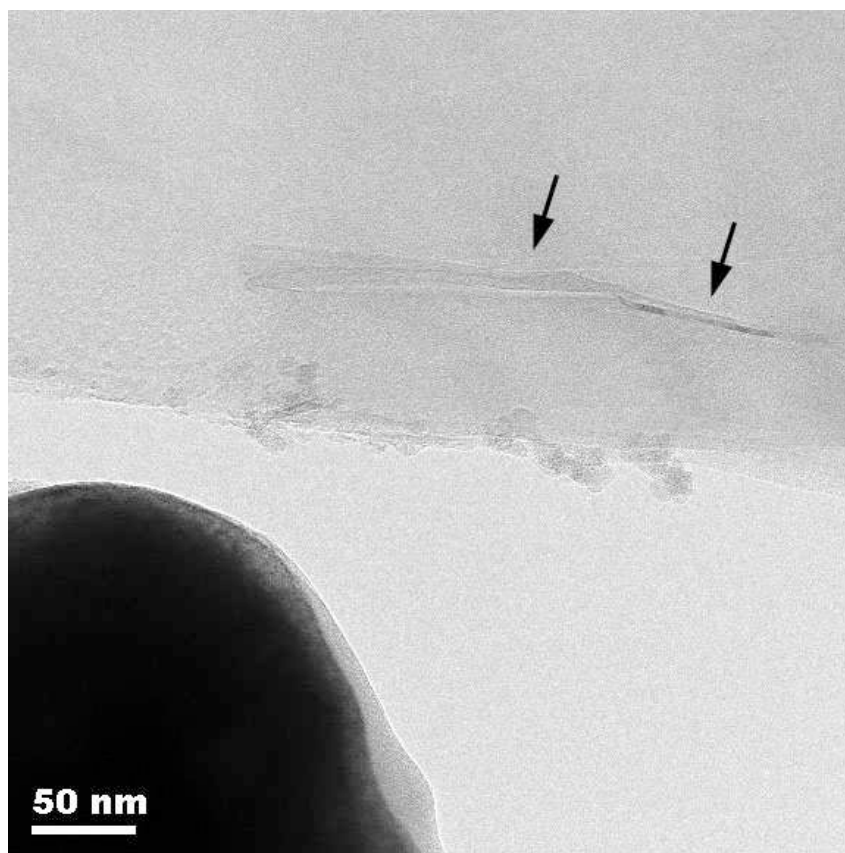
Figure 4.4.   Wear track (indicated by arrows) induced by sliding tungsten probe

planes in Figure 4.5 indicates that sliding took place directly adjacent to them, causing the sliding tip to remove material from the HOPG surface, subsequently pushing material to the side of the contact region.   Graphite flakes are left in the tips wake, of which a number are oriented parallel to the electron beam.

Immediately after sliding, the tungsten probe was inspected for evidence of material transfer, as predicted by Dienwiebel et al.   Figure 4.6 shows evidence that graphitic material is present on the surface of the tungsten tip.   These features were neither seen before sliding, nor significantly long afterwards (> 5 minutes), since beam damage is significant for small amounts of perpendicularly oriented graphite at 200 kV. A line scan
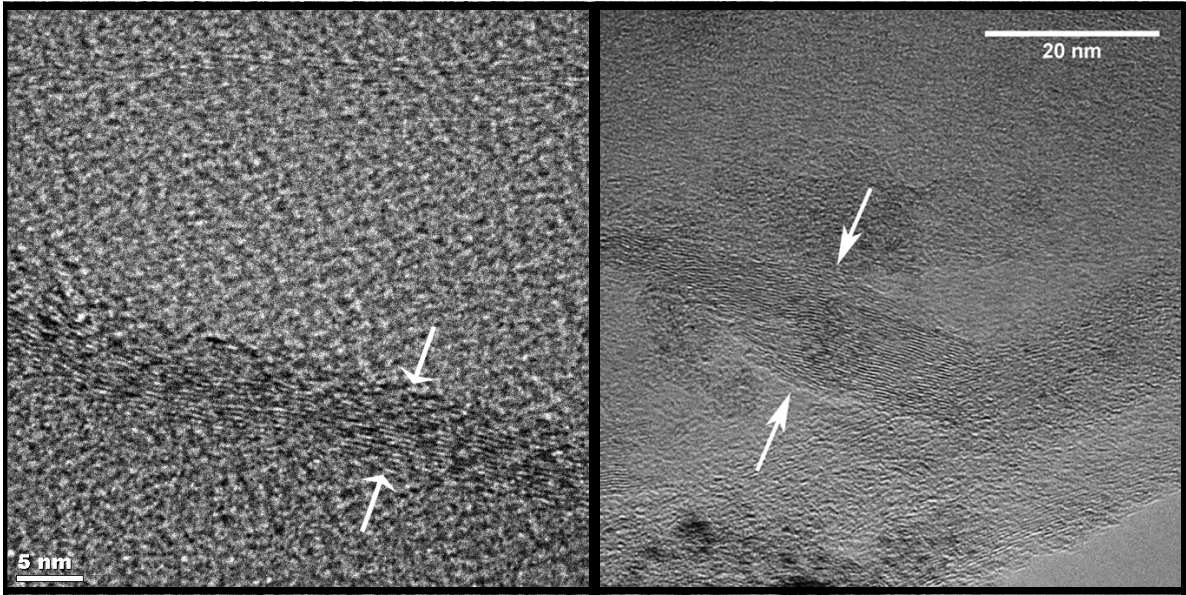
Figure 4.5. Bright field (a) and high resolution (b) image of the wear track after 100 passes with the tungsten probe.

along the transfer layer (Figure 4.6) measures the planar spacing at 3.5 $\mathring{A}$, in agreement with the known graphite basal spacing of 3.36 $\mathring{A}$. The thickness of the attached graphite flake is seven basal spacings, or 2.45 nm. This observation confirms that wear takes place by strong adhesion and transfer to the tungsten sliding probe. This establishes a graphite-graphite sliding interface demonstrating the mechanism responsible for the lubricious properties of graphite.

4.5. Discussion

The results of the *in-situ* sliding experiment give direct evidence that crystallographic structure influences the tribological behavior of graphite. Graphite clearly wears by the removal of sheets on the order of nanometers in thickness by adhering to the tungsten sliding probe. This confirms the hypothesis that low friction, as observed by Dienwiebel et
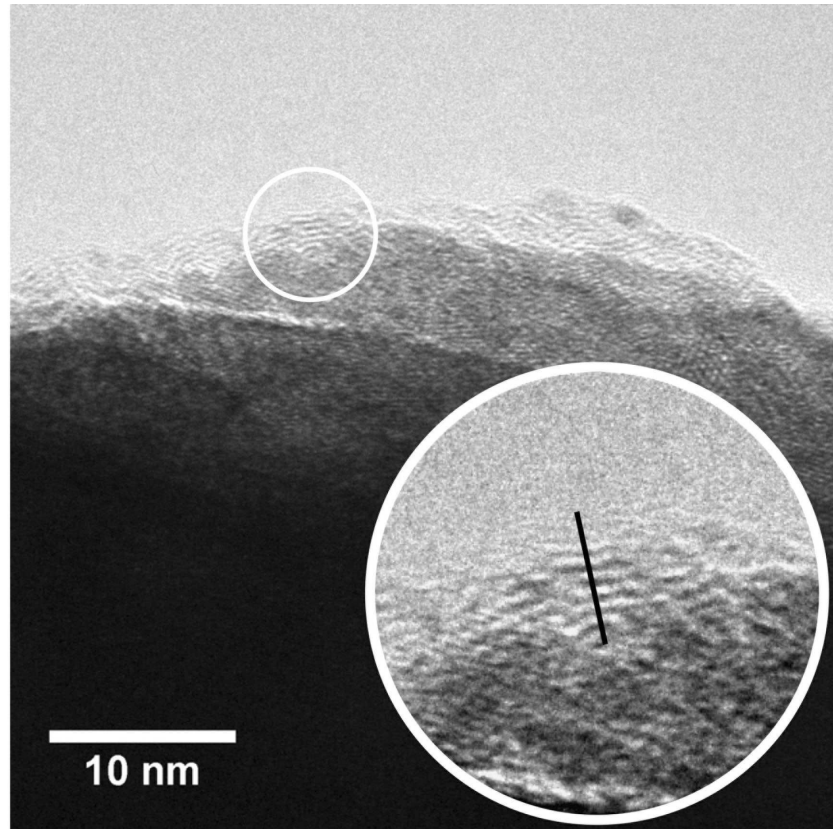
Figure 4.6. Graphite transferred to tungsten tip by sliding

al., is a measurement of friction between graphite basal surfaces. We can take this analysis a step further by analyzing the nature of the worn graphite flakes. Specifically, the defect structure may have a direct role in the graphitic wear mechanism, for it is the motion of dislocations throughout a material, be it at an interface or in the bulk, that is the principal mechanism for deformation in materials. It is well established that for heterogeneous interfaces consisting of two materials with differing shear moduli, interfacial dislocations will be displaced by some standoff distance into the softer material [108, 106, 128, 129]. This phenomenon arises from equilibrating image and adhesion forces at an interface of materials with differing elastic constants. The concept of an image force is required to

account for the continuity of elastic stresses across the interface boundary, which, in turn, may affect the strength of the interface. In the original studies on metal-ceramic interfaces $(Nb - Al_2O_3)$, a standoff distance of 1.9 (110) spacings was calculated and experimentally observed to be 4 (110) spacings [107]. For interfaces with a large shear modulus mismatch and a small crystallographic mismatch, it is not unreasonable to expect the equilibrium position of dislocations to be found greater than 20 planar spacings from the interface in the softer material [108]. Following Kamat's analysis for screw dislocations by inputting shear moduli for tungsten and graphite, we arrive at a standoff distance estimate of 15 nm (44 planar spacings). This is consistent with the observed thickness of wear flakes observed in the TEM images in this study. Once a graphite flake has been worn and attached to the tungsten probe, the graphite-graphite interface will exhibit no significant dislocation standoff, as the sliding interface is becomes the dislocation plane. A more detailed dislocation analysis would be interesting to apply to a variety of sliding interfaces. It is worth noting that this dislocation-transfer layer wear mechanism is entirely consistent with Section 2.7.4 of the analytical model developed in Chapter 2.

4.6. Conclusions

We have directly observed wear induced by a single asperity tungsten probe sliding on graphite by *in-situ* TEM nanomanipulation. Landmark atomic scale friction experiments have drawn conclusions about the sliding behavior of these materials, notably the observation of atomic scale stick-slip, friction anisotropy and superlubricity. Our *in-situ* TEM work has confirmed the transfer of graphite to a tungsten probe after sliding - direct evidence that validates the proposed friction mechanism of graphite-graphite sliding

phenomena. Wear of HOPG was observed typically removing sheets of graphite on the order of ten basal planes in thickness. We believe the role of dislocations - their structure and dynamic behavior at interfaces - is largely uncharacterized in the field of tribology. We hope the application of similar *in-situ* techniques in combination with more complete theoretical models will build on this basic understanding.

CHAPTER 5

Liquid-like Tribology of Gold

5.1. Metallic Lubrication

Metal-metal sliding contacts represent the most abundant class of materials where tribological understanding is crucial in a wide variety of applications, including automotive gears, turbine engines, sliding electrical contacts, and biological implants. Sliding between clean metal surfaces is typically associated with very high friction (from high adhesion) and large wear rates, as shown by ultrahigh vacuum experiments [79, 78, 77]. The use of lubricants therefore became the limiting factor in tribological performance between metals. However, under conditions where the use of organic-based lubricants is unfavorable (e.g. vacuum, high temperatures), metals in the form of nanoparticle additives to lubricants can be used to reduce friction losses and eliminate device failure [130, 131, 132]. Metallic additives can improve the tribological performance of a lubricant at high temperatures and pressures, where it has been hypothesized they undergo a melting transition at asperity interfaces from frictional heating at high loads [132]. In a more fundamental sense, it is of great interest to directly characterize the mechanical deformation properties of metals under sliding conditions at contact sizes on the scale of nanometers to microns, where traditional experimentation has lacked the ability to draw precise conclusions linking microstructural change with tribological properties.

Here we investigate the behavior of gold sliding contacts by *in-situ* transmission electron microscopy (TEM). *In-situ* TEM techniques have made it possible to directly measure electrical and mechanical properties of gold contacts, including atomic sized contacts exhibiting quantized conductance steps associated with atomic rearrangements [133, 134], and high resolution visualization of deformation of nm-sized gold interfaces via slip and twining [135]. While most of these studies focus on atomic scale effects at room temperature, they generally do not consider nano- to micron-sized contacts at elevated temperatures: those that bear the most relevance for metal-metal tribological interfaces. Collective effects such as dislocation motion and surface diffusion play a more significant role in determining tribological properties between metals than the peculiar mechanics of atomic-sized nanowires.

5.2. Sample preparation

Au (110) films were evaporated at 335°C in vacuum (10^{-9} Torr) on cleaved NaCl crystals, then removed by dissolving the salt in water and placed on Au TEM grids, and subsequently thinned by ion polishing. The samples were then mounted on the TEM stage at an angle of 30 degrees to the horizontal, viewed schematically in Figure 5.1. This compromise enables simultaneous inspection by the scanning probe and the electron beam. Tungsten probes were electropolished from 0.25 mm polycrystalline wire in a 2 N NaOH solution to radii between 2 and 100 nm. The STM-TEM holder was plasma-cleaned for 15 minutes immediately before insertion into the TEM column. A liquid nitrogen trap was used to minimize contamination effects.
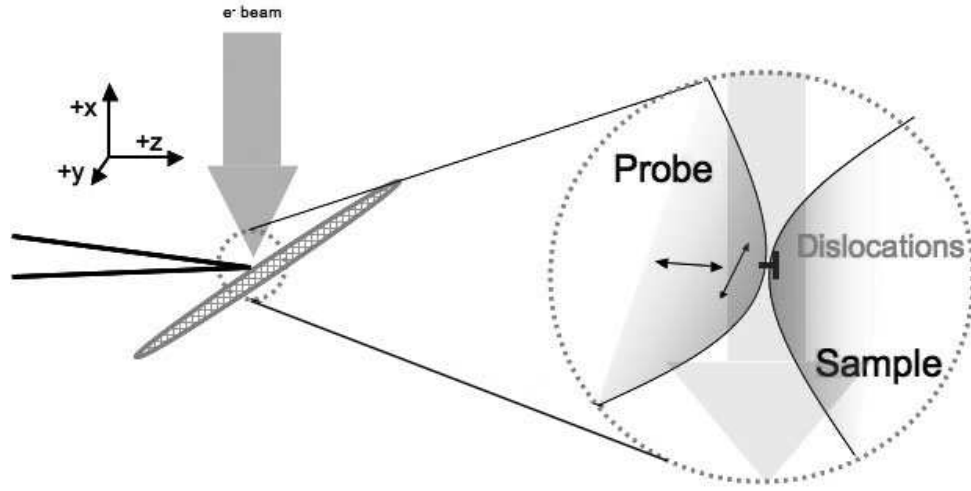
Figure 5.1. A STM-TEM schematic, showing a tilted TEM sample geometry, allows for simultaneous analysis by the tip and electron beam.

5.3. Liquid-like behavior of gold

Upon insertion into the TEM column, the tungsten probe was carefully manipulated to approach and contact the gold specimen. A series of normal approaches and lateral sliding events were carried out and captured on a TV-rate monitor in order to record the dynamic behavior of the probe-sample interaction. Typically, the force exerted by the STM probe, although not directly measured, was enough to bend the gold film by 50 nm in projection. Although the mechanical properties of thin films are not known and can be highly anisotropic, a crude estimate of bending a film was made by approximating the film as a cantilever 10 nm thick, 1 μm long, and 100 μm wide. The force required to move it in projection by 50 nm is on the order of 100 nN.

Initial contacts showed evidence of strong adhesion between the tip and sample, but subsequent sliding and indenting the surface only showed changes is contrast due to bending of the compliant thin sample. A bias pulse of 5 V for 100 msec was applied in an

attempt to clean the surface of adsorbed contaminants. This served not only to remove hydrocarbon contaminants, but locally heat the Au above the melting point, transferring an amount of Au to the W probe. After one minute, allowing the sample and probe to thermally equilibrate, and setting the probe bias to 100 mV, contact was once again established. Highly plastic liquid-like behavior was observed after repeated snap-in and pull-off sequences through the formation of sharp asperities on either side of the contact region. Rapid formation of a neck region upon contact was observed. Figure 5.2 shows a sequence of still frames from a TV-rate video capture. Sudden snap-in contact is established with the formation of a neck region. This process is begun and completed within the time of a single video frame (1/25th second). Following the initial contact, the probe was moved side to side, maintaining the plastically deformable neck contact. Contrast changes along the length of the neck are seen, indicating changes in thickness via material transfer.

Following the Wiedemann-Franz law and the related method of calculating Joule heating at small electrical contacts developed by Holm [136], we solved for the temperature at the junctions observed in situ. For a gold contact initially at room temperature, a bias of 100 mV corresponds to a maximum contact temperature of 166 °C, far below the melting point of gold (1064 °C). What we have observed is a process known as liquidlike growth, first observed in situ by Pashley *et al.* [137]. This process appears to behave in a similar way to the coalescence of liquid droplets; a very fast formation of a necking region between two particles, followed by slower, more gradual growth into a single particle, reducing the surface free energy. However, liquidlike growth, as observed for gold only depends on the

high mobility of surface atoms. Bulk diffusion is not a significant contributor since the time scale of such events at small length scales is far longer than for surface diffusion.

It is clearly evident from the TV rate images that coalescence between the tip and sample occurs within the time scale of one frame (1/25th sec). Let us estimate the time scales on which surface and bulk diffusion act for relevant length scales. Conservative values for surface diffusion rates, albeit obtained with some inconsistency, are in the neighborhood of 300 nm^2/sec. Expressions from sintering theory as reported by Pashley et al. for gold yield significant differences in the time of initial coalescence depending on the transport mechanism used. For a 100 $\mathring{A}$ radius particle, volume diffusion acts on the order of 10^{-3} seconds, where surface diffusion yields a time of 10^{-7} seconds. Scaling up to a larger particle of 1000 $\mathring{A}$ yields times of 100 seconds for volume diffusion and 10^{-3} seconds for surface diffusion. Time scales for in situ laboratory experiments become quite long once the particle size reaches 1 μm, with coalescence times of 10^3 and 10^1 seconds, for volume and surface diffusion, respectively. It should be noted that these times are unrealistically small; nanoparticles do not equilibriate this rapidly. The source of this discrepancy is unknown.

We now make a numerical estimate for the friction forces at a liquid-like viscous contact, and compare this to the dislocation model developed in Chapter 2. The dislocation model includes two terms, one that is constant with velocity (radiation friction) and the other that is linear with velocity (viscous drag). For this estimate, we include only the viscous dislocation drag contribution, as this maintains the same qualitative friction behavior as an estimate for a viscous liquid drag does. By taking the surface diffusion rate of 300 nm^2/sec for gold, we may convert this to an effective viscocity, and thereby
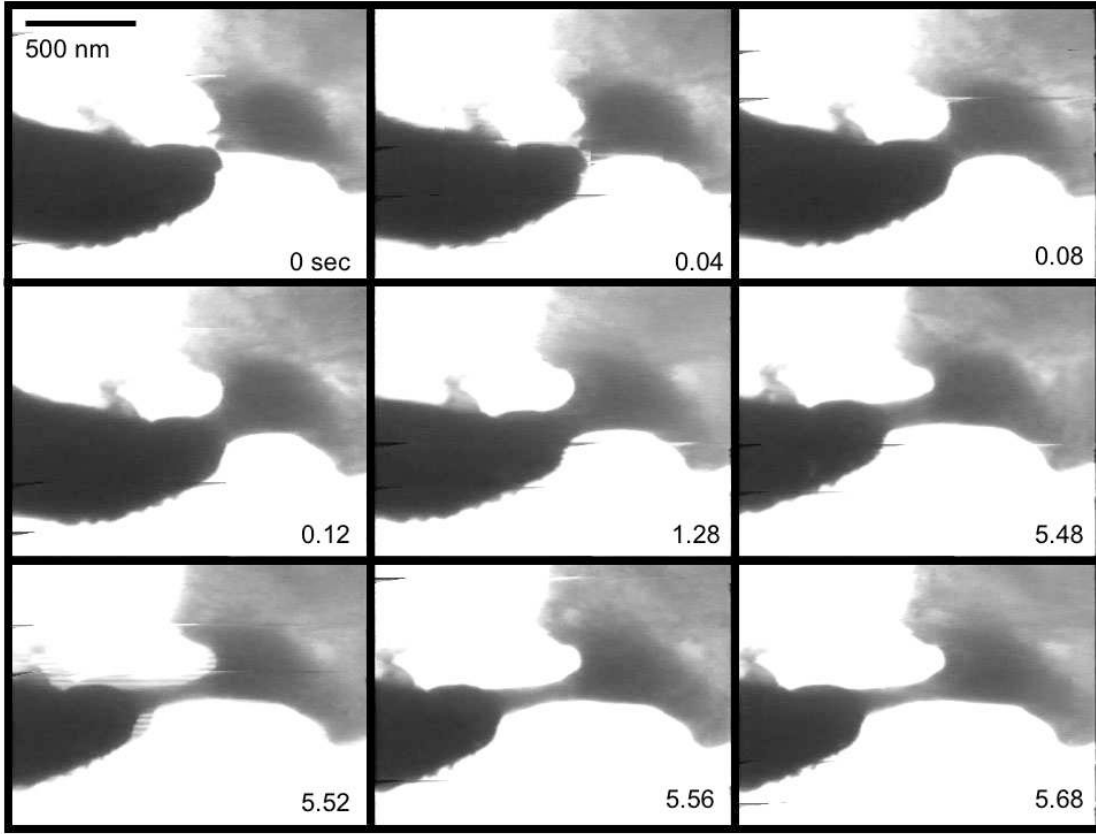
Figure 5.2. Still frames showing the interaction of the tungsten probe and gold film under 100 mV bias. Snap-in to contact is seen in the first three frames followed by a retraction of the probe showing liquid-like behavior.

produce an estimate of the friction force, using the contact area and thickness observed in the TEM. This can be achieved by approximating the contact as sliding parallel surfaces with a confined viscous liquid, as is the case in Couette flow. Of course, this is a rough estimate, and is not intended to be a detailed numerical analysis of the nanoscale dynamics. Capillary forces may quite possibly be a larger contributor to drag at this scale, but are not calculated here. Converting D (300 nm^2/sec) to a viscosity at 166°C gives a value of ν=1.61 Pa·s, which is only an order of magnitude greater than air at 166°C. For a contact area of 0.008 μm^2, the Couette drag coefficient is calculated to be

$B_{Couette} = 1 \times 10^{-11}$ N · s · m^{-1}. This value may be compared to a drag coefficient for a solid-like interface. Conveniently, we have already done this (Chapter 2). If we take the same size crystalline interface (perfectly clean, uncontaminated), we can calculate the friction force or drag coefficient based on a number of moving dislocations present and moving at the interface. Under these circumstances, to make a fair comparison between two viscous phenomena, the radiation drag mechanism is not included in the calculation. This makes only high-velocity comparisons valid, but allows us to compare the viscous drag coefficients directly. Doing so, yields a value of $B_{Dislocation} = 5 \times 10^{-4}$ N · s · m^{-1}, giving a ratio of $B_{Couette}/B_{Dislocation} = 2 \times 10^{-8}$. This is quite a massive difference, but we must remember that $B_{Couette}$ has been underestimated and $B_{Dislocation}$ overestimated, each conceivably one or two orders of magnitude. $B_{Dislocation}$ was higher than experimental findings in Chapter 2 (Table 2.6.1), since even the cleanest UHV conditions could not avoid some degree of surface roughness from sample preparation techniques. A more detailed analysis must be performed to accurately asses the liquid-like viscous drag force, as the simplified calculation here cannot accurately model the complex edge effects of the mechanical properties of liquid-solid interfaces on this small scale.

It must be emphasized that calculating friction forces on this scale from first principals has rarely, if ever, been carried out. The challenging task of finding reasonable agreement is a product of describing a simple value (a friction force) by many inter-related physical phenomena. Transforming these fundamental calculations into tangible results for friction measurements in real lubricants remains a tremendous challenge, but important steps have been made in understanding the microstructural mechanisms involved. In fact, we urge experimentalists to explore this metallic liquid-like transition on a slightly more

macroscale through ultrahigh vacuum friction experiments. Controlling the excitation of a particular mechanism (liquid-like or solid-like) rests largely in controlling the surface passivation, something that is not trivial except with UHV techniques. It would be particularly enlightening in terms of the *in-situ* results presented here to quantify the ratio of liquid- to solid-like friction forces between metals.

With the *in-situ* evidence we have obtained in this study, a good case can be made that what we have observed is in fact the liquid-like coalescence of gold dominated by surface diffusion at temperatures significantly lower than previously recorded. The tribological implications of this indicate that contact pressures between metallic tribo-surfaces need not reach levels as to create contact temperatures above the melting point of the material, but significantly lower as to excite liquid-like lubricating properties.

5.4. Ploughing and Gouging Wear

In a separate test conducted with no tip-sample bias, sliding the tungsten probe along the edge of the gold sample showed evidence of ploughing deformation a common explanation for high friction and wear rates between metals. Figure 5.3 shows a series of still bright field images from a TV rate (PAL) capture of the gold film being deformed. As the slider passes across the sample, a wear track is left plastically deformed. As far as we are aware, this is the first direct demonstration of ploughing on this length scale by in situ TEM. A bright field image of the area after deformation can be viewed in Figure 5.4.

Figure 5.5 shows an indentation series over the course of tens of minutes. Bend contours, some periodic, are observed in the gold sample as the harder tungsten tip is pressed against it. Eventually a significant degree of deformation in both the gold sample
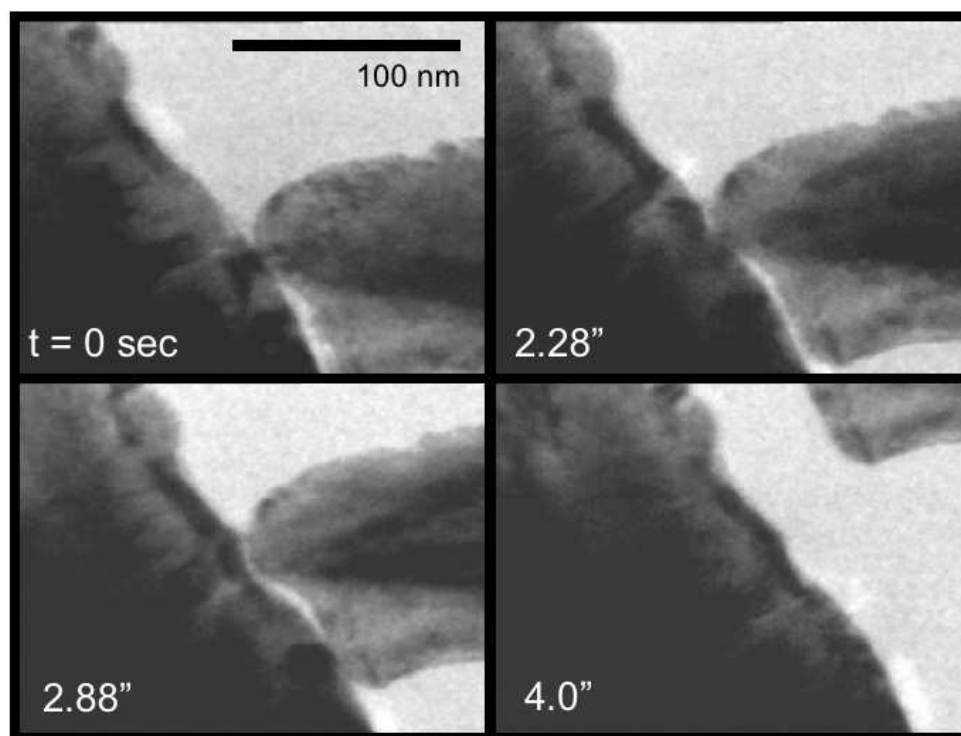
Figure 5.3. Ploughing wear of gold on the nanoscale. Series of TEM bright field images with frame times indicated.

and the tungsten tip is seen. Upon moving the tip parallel to the sample edge to induce sliding, the interface ruptures suddenly, tearing a large amount of the gold film out with the tip as seen in Figure 5.6. This large amount of adhesion and ensuing wear is consistent with high static friction phenomena between metallic surfaces, related to gouging wear effects. The contact was carried out with zero tip-sample bias and lasted 20 minutes from initial contact to pull off. The presence of 3 nm of contamination is seen in the upper left corner of Figure 5.5a. Surface contamination will decrease the surface diffusion coefficient significantly, since the surface energy is greatly reduced.
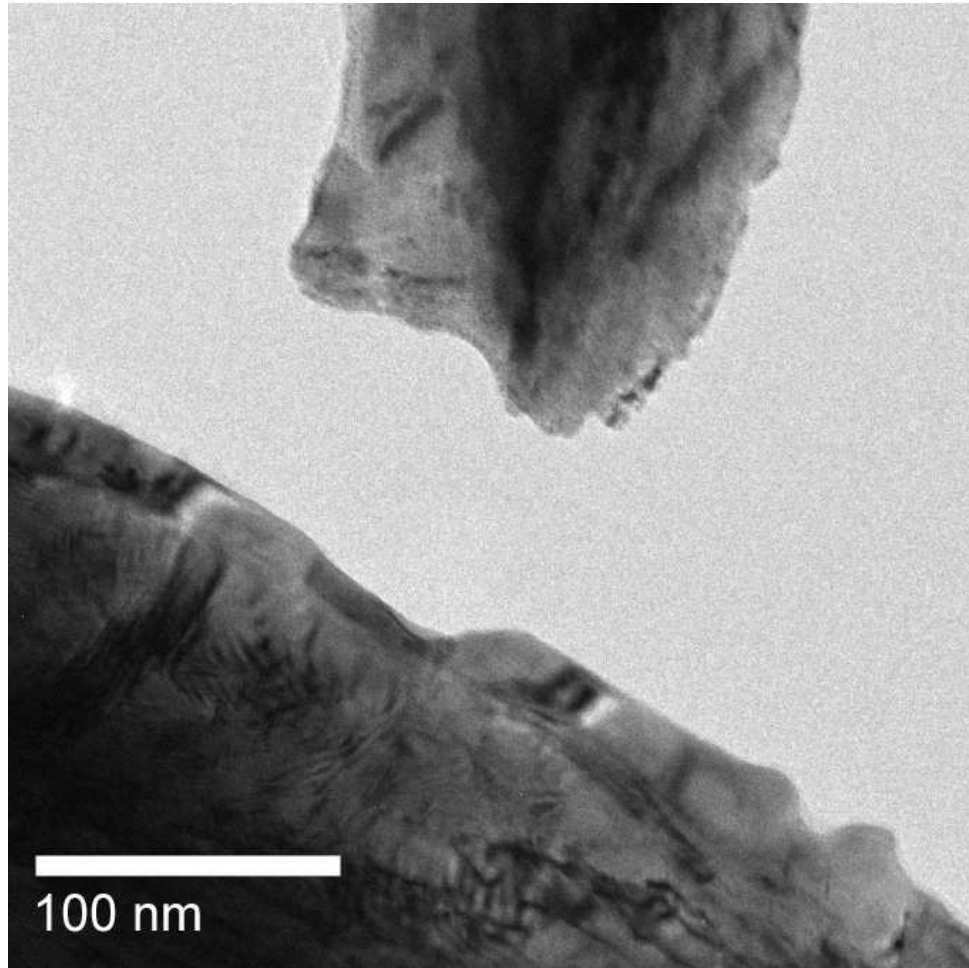
Figure 5.4. BFTEM image of the ploughing-deformed Au sample.

5.5. Dislocations

What appears to be dislocation motion was observed in a series of indents with the tungsten tip into the Au (110) sample. A defect-free region is indented, producing features extending radially outward from the contact region after contact is established. Figure 5.7 shows four images from initial contact through pull-off.
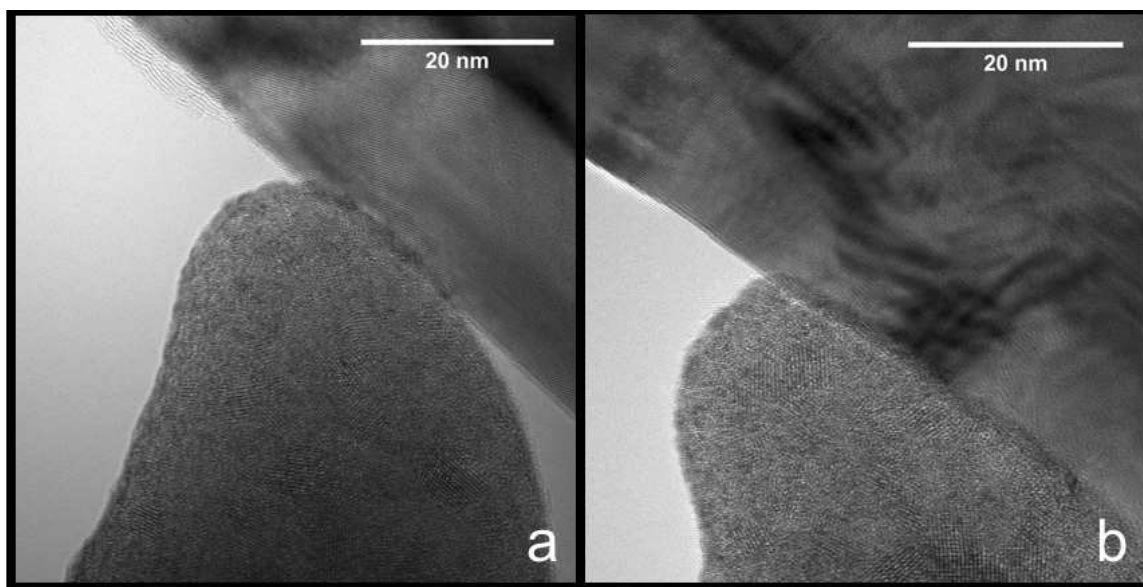
Figure 5.5. High resolution TEM image of a tungsten tip indenting a gold sample. Time between exposures: 10 minutes.

5.6. Method for Ultrafine Au Tip Fabrication

A practical benefit arose from the observation of liquidlike behavior at low temperatures. Upon retracting the probe rapidly from the sample after coalescence, we were able to fabricate very sharp gold tips. The radii of these tips were consistently kept under 5 nm. Figure 5.8 shows a tip formed by this method of pull-off after bias pulsing and reapproaching at a small potential. Electron dispersive x-ray spectroscopy (EDX) was performed (Figure 5.9) to qualitatively identify the chemical composition of the newly formed peak. By the spectra, it is apparent that Au has transferred to the W probe, and forms the sharp apex at the tip region. No tungsten is detected at the end of the tip.

Small tips are very useful in mechanically and electrically characterizing nanostructures or thin films. A highly localized gold probe is an alternative to costly carbon nanotube tips currently being offered, with the advantage of a lower aspect ration (for
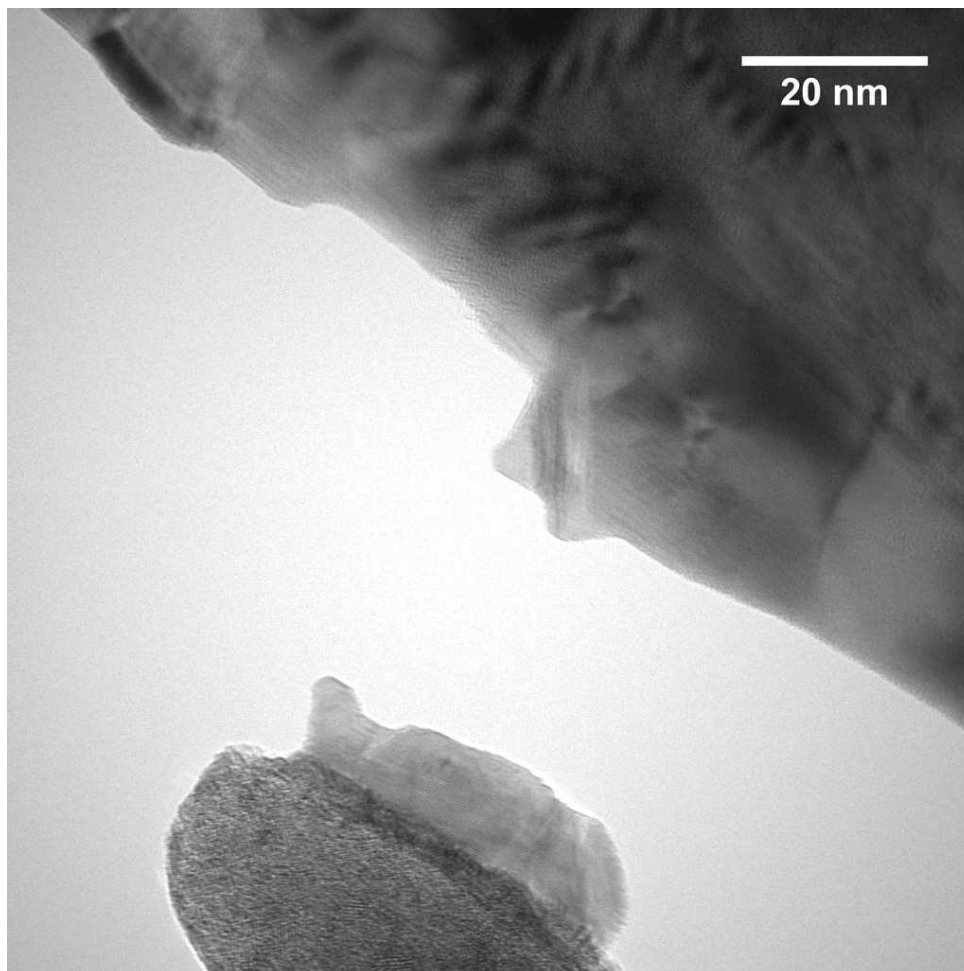
Figure 5.6. High adhesion between tip and sample give rise to gouging wear of the gold.

rigidity in probing) and a lower local tip radius than multiwall nanotubes. If a tip is damaged, it may be reconditioned *in-situ* to a sharp radius once again.

5.7. Conclusions

We have presented direct observations of nanoscale tribological phenomena between a tungsten single asperity probe and gold surfaces by *in-situ* TEM manipulation and characterization. The observation of ploughing on the nanoscale, effects of contamination,
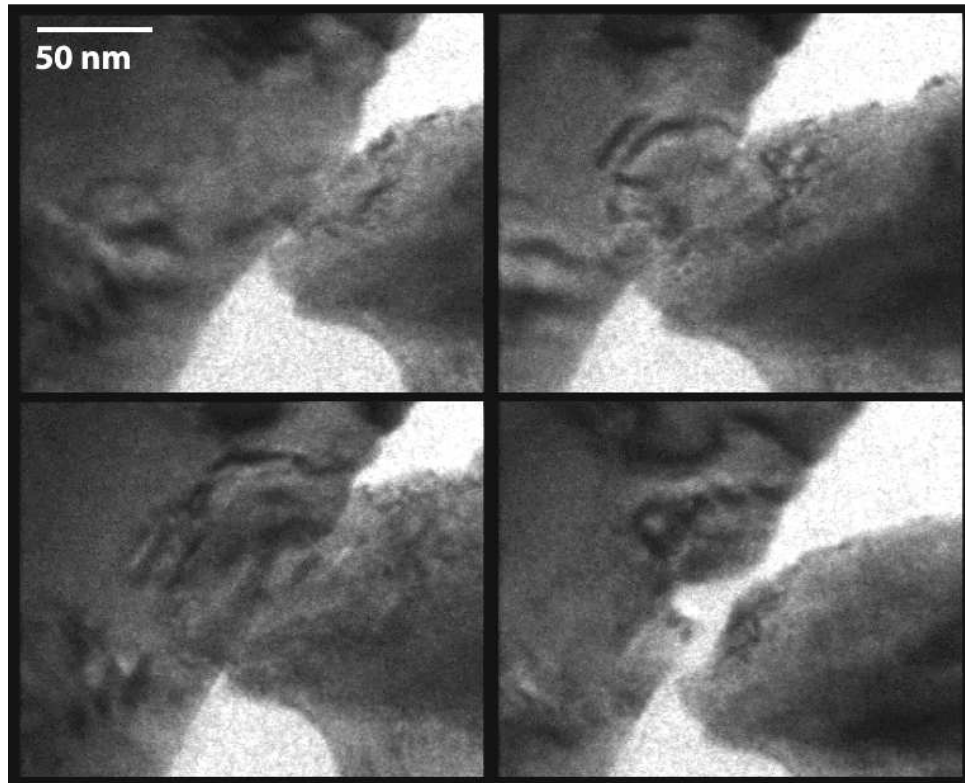
Figure 5.7. Indentation series captured by video rate camera showing deformation structure similar to the bowing of dislocations. Approximately 10 seconds between images.
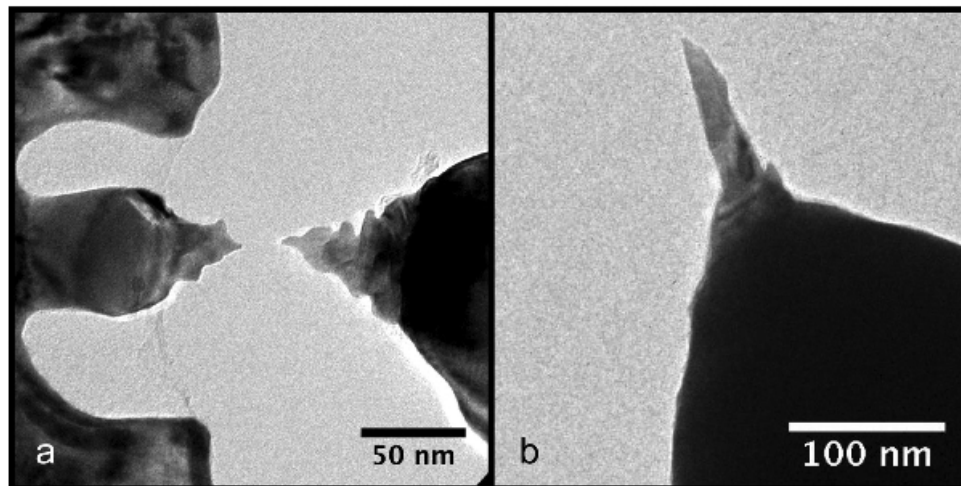
Figure 5.8. Fabrication of an ultrafine Au probe by biasing and pull-off.
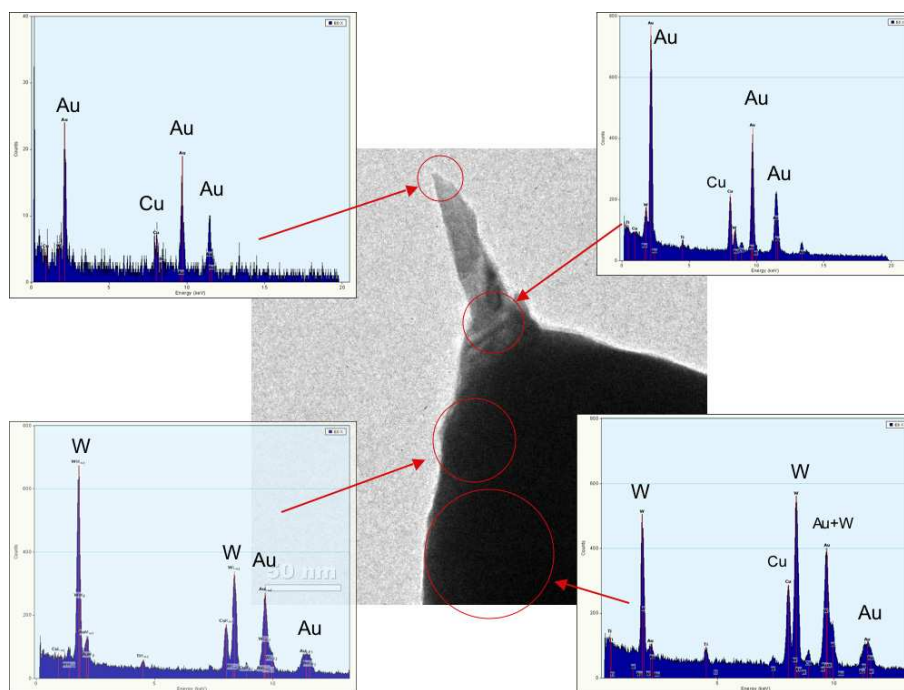
Figure 5.9. EDX spectra taken from regions of the fabricated probe showing
Au concentrated at the tip region.

and strong metal-metal adhesion were captured in real time as a scanning probe contacted
and slid across a gold sample. Direct evidence of liquidlike behavior of gold was seen at
166 °C the first such direct observation at such low temperatures. This points directly
to the applicability and significance of metals as alternatives to traditional organic based
lubricants, without the requirement of operating temperatures above the melting point
of the material. Finally, we developed a simple method for fabricating very sharp gold
probes useful in a number of electrical or mechanical testing conditions.

5.8. Future Work

Recently it has been shown that the onset of dislocation motion occurs before the usual
first displacement slip in nanoindentation experiments [123]. Minor et al. performed an

in situ TEM nanoindentation experiment on a defect free aluminum grain and observed dislocation behavior before the first pop-in displacement, barely resolvable by the force-displacement sensor (at 1.5 μN). Shear stresses close to the theoretical shear stress of the material were clearly supported by a grain full of dislocations, challenging the view that only a dislocation free zone of material is capable of supporting such high shear stresses.

In this light, there remains to be observed a wealth of dislocation behavior by *in-situ* microscopy techniques, particularly in the case of sliding interfaces. The effect of surface passivation and tribolayers can fundamentally change the way dislocations behave at sliding interfaces, yielding altered tribological properties. Linking the two, requires careful but achievable analysis by *in-situ* TEM.

CHAPTER 6

Sliding Induced Graphitization of Amorphous Carbon Films

6.1. Diamond-Like Amorphous Carbon

Of the many allotropes of carbon (Figure 4.1), diamond-like carbon (DLC) refers to a class of metastable disordered carbon with significant sp^3 hybridization. DLC films combine high hardness and strength with chemical inertness, electrical insulation, optical transparency, and low static and kinetic friction. Employed as protective coatings, these materials see a number of technological applications including automotive gears, magnetic storage disks, biological implant coatings and micro-electromechanical (MEMS) devices [138]. We seek a more detailed understanding of the bonding structure and deformation mechanisms responsible for its attractive tribological properties. First, we will briefly discuss its structure and mechanical properties.

6.1.1. Phases and Bonding

Many of the favorable properties of DLC materials are inherited from the distribution of sp^2 and sp^3 bonded carbon atoms as found in graphite and diamond, respectively. The sp^3 configuration assigns a strong sigma bond to each of carbon's four tetrahedrally directed valence electrons. In contrast, the sp^2 hybridization found in graphite exhibits three trigonally directed orbitals forming in-plane σ bonds, where the last valence electron lies normal to the σ bonded plane in a π orbital. This π bond is relatively weak,
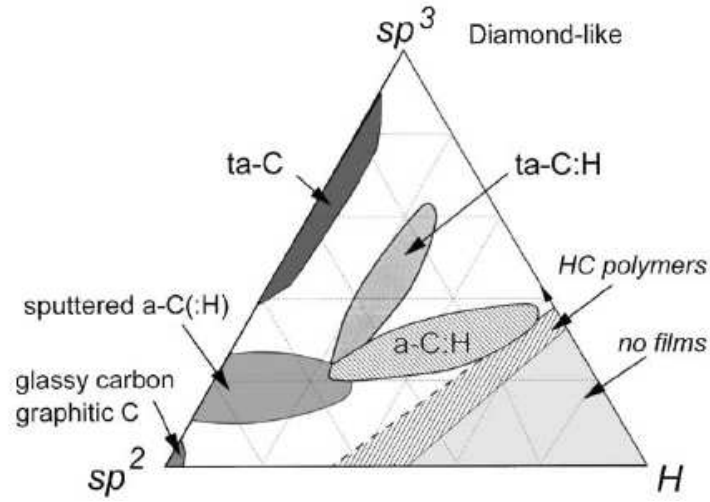
Figure 6.1. Ternary phase diagram of carbon-hydrogen alloys (from Ref. [3]).

and is considered to be responsible for the inherent low friction properties of graphite - something that is directly linked to its layered crystal structure, as found in similar lubricious solids (e.g. MoS_2, hexagonal boron nitride, WS_2). DLC may contain anywhere from <1 to $\simeq$50 atomic % hydrogen [3]. A ternary phase diagram (Robertson, 2002) (Figure 6.1) illustrates the various amorphous C-H alloys (originally Jacob and Moller). The DLC materials in this study are of the type a-C:H, and are found near the center of the triangle. Notably, diamond-like a-C:H has a smaller fraction of sp^3 bonding and a higher hydrogen content than tetrahedral amorphous carbon (ta-C). This gives ta-C extremely high hardness (second only to diamond), but makes DLC films more useful for protective tribological coatings, since DLC films have better coverage, have no grain boundaries, and may be deposited at room temperature.

6.1.2. Mechanical and Tribological Properties

High hardness and low friction and wear rates, combined with an abundance of deposition options make the use of amorphous carbon films very attractive for tribological applications. The source of their high hardness is often directly attributed to the abundance of tetrahedrally bonded carbon atoms, where hardness values reach significant fractions of diamond's hardness, up to about 20 GPa [139]. Friction values of DLC films have been reported at extremely low values. Erdemir et al. developed a technique of plasma-enhanced cemical vapor deposition (PECVD) to grow ultra-low friction hydrogenated films in a plasma of a 3-1 hydrogen-methane mixture. Films grown by this method have attained friction coefficients as low as 0.001 [140] in inert environments.

Unfortunately, not all DLC films have such attractive qualities. In fact, DLC materials probably have the largest range of wear and friction coefficients among solid lubricants [141]. Ranges of friction coefficients have been reported in the literature from $\mu = 0.001$ - >0.5. To explain this variety, it has been shown that sensitivity to humidity, hydrogen content and oxygen partial pressure has a significant effect on friction and wear rates [142]. Studies performed in UHV have indicated that water vapor pressures increased above 2% RH increase the friction coefficient of hydrogenated DLC films by an order of magnitude. Hydrogen-free DLC films tend to show low friction properties in humid environments, while hydrogenated films only possess this property in dry or inert environments. Doping hydrogenated amorphous carbon films with sulfur atoms has recently been shown to maintain low friction performance in humid environments [143].

The controlling mechanism considered responsible for achieving low friction is the formation of a carbon-rich transfer layer, which is graphitized by an activation process.

Liu *et al.* identified graphitized transfer layers attached to the surfaces of macroscopic pin-on-disk sliding contacts through *ex situ* TEM and Raman spectroscopy [144]. The accompanying reduction and stabilization of friction forces correspond to the transformation from diamond-like carbon to a graphite-like carbon by both thermal and mechanical excitation.

6.2. Experimental Procedure

The goal of the present investigation of DLC films is to unambiguously correlate structure and bonding changes with the degree of sliding by observing a single asperity sliding contact via *in-situ* TEM. In particular, we seek direct evidence for the mechanically-induced graphitization process on the nanoscale by electron energy loss spectroscopy (EELS). The formation of a graphitized tribolayer by mechanical activation is quite possibly the mechanism that gives many DLC films favorable friction properties. By observing this process directly, and not relying on postmortem analyses, we can form a more accurate understanding of this unique class of materials.

6.2.1. EELS

Electron energy loss spectroscopy detects the energy loss from inelastically scattered electrons after passing through a thin TEM sample. The characteristic energy loss for carbon can be divided in to two regions: the low loss (0 to 40 eV) and high loss (285 eV and above). We are interested in the high loss region corresponding to the carbon 1s (K edge) transitions, which are the signature of the π and σ excitations. The near edge peak at 285 eV identifies the π excitation as found in graphitic carbon, while the 290 eV peak is
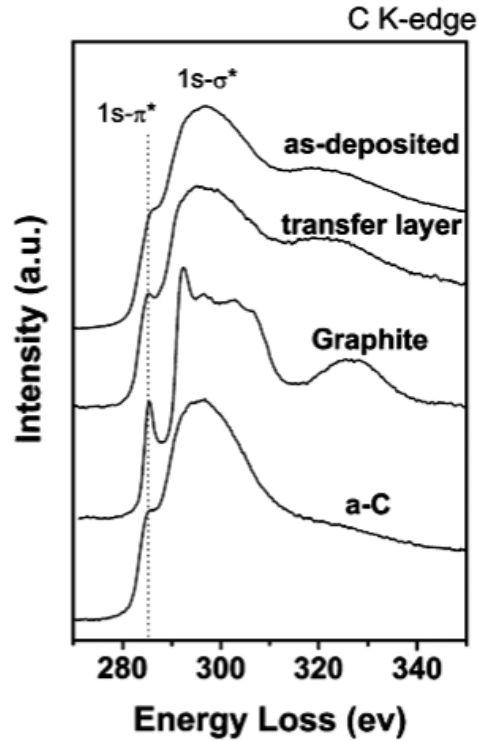
Figure 6.2. EELS spectra from Ref. [4], showing the change in the 1s-π peaks for graphite and amorphous carbon.

due to the σ excitation. Figure 6.2 shows typical near edge EELS spectra for a number of carbon phases from reference [4], where the 1s-π peak is the best indicator for determining whether graphitic material is present.

6.2.2. Sample Preparation

Samples were prepared using a plasma-enhanced chemical vapor deposition (PECVD) technique. A capacitively coupled r.f. discharge plasma was struck at 30 mTorr with a bias of -500 volts. The first film, NFC6, was produced with a gas mixture of 25% CH_4 and 75% H_2. This ratio of methane to carbon has been shown to have lower wear rates and friction forces than other mixtures [140]. A 30 nm bond layer of Si was deposited in order

to improve adhesion to the Cu grid, as most DLC films suffer from delamination problems. Following this, the carbon film was deposited at room temperature to a thickness of roughly 100 nm. The second film, NFC7, was fabricated using the same growth conditions, but in this case the gas precursor was pure methane. NFC7 exhibits poorer tribological performance (higher friction and wear) than NFC6, as determined by macroscopic pin-on-disk experiments [140].

For the sliding pin, tungsten probes were electropolished from 0.25 mm polycrystalline wire in a 2 N NaOH solution to a minimum radius of curvature on the order of tens of nanometers, following the standard method.

6.2.3. Sliding Procedure

A series of sliding passes were performed with the tungsten probe on the NFC6 sample. The sliding velocity was approximately 1 μm/sec, and EELS spectra were taken after every 50 or 100 passes. A post-column gatan image filter (GIF) was used on the Tecnai F20ST at 200 kV (Argonne National Laboratory) to perform the EELS measurements. Each measurement was made from a region of approximately 100 nm that corresponds to the center of the sliding track. TEM bright field images were then captured before and after sliding to record the microstructure of the sample. It was found that excessive sliding (> 400 passes) caused the sample to delaminate from the copper grid.

6.3. Results

NFC6 as prepared showed evidence of small crystalline objects usually concentrated at the edge of the sample, as shown in Figure 6.3. We believe this is due to the deposition
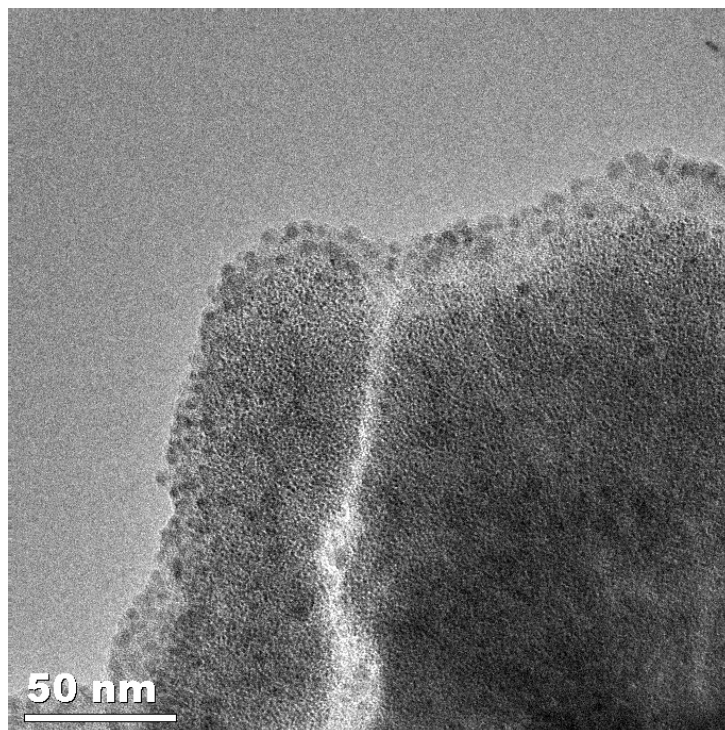
Figure 6.3. Bright field TEM image of NFC6 showing the presence of nanocrystalline islands localized at the sample edge.

process directly onto a TEM grid, as these regions of the film near the grid square may not have had sufficient physical contact to a thermal sink for cooling. This is not a result of any post-deposition processing of any sort. Figure 6.4 shows a bright field image of the NFC6 sample and tungsten tip between sliding events. The inset oval indicates the region where contact was made. The material seen at the end of the tip is carbon wear debris, and is also evident on the tungsten tip. The source of this is likely combination of contamination from the electron beam and delaminated layers from the sample. The smallest local radius of curvature of the tip was measure to be approximately 20 nm, but the contact region was shadowed and was likely somewhat larger.
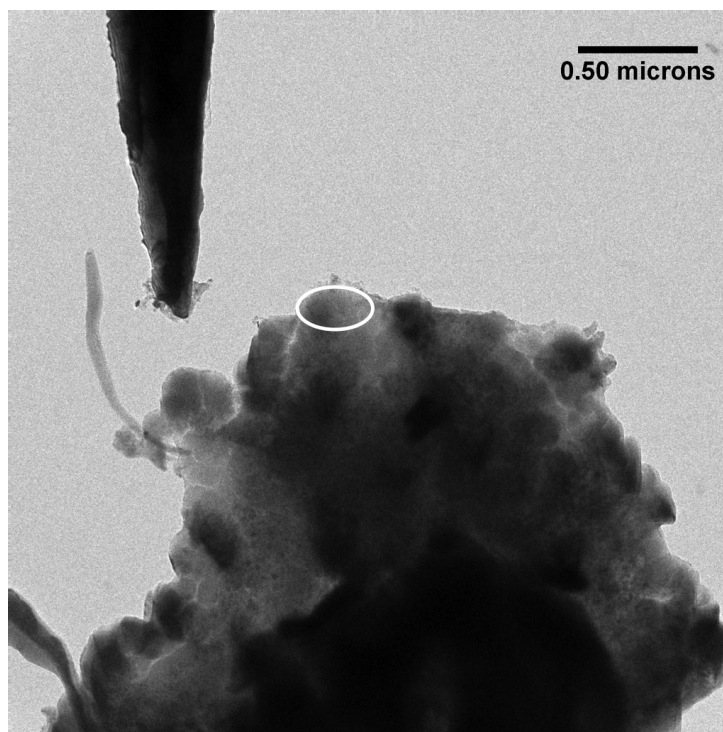
Figure 6.4. Bright field image of NFC6 indicating the sliding region after 200 passes.

The EELS spectra captured immediately after each set of 100 sliding passes show a distinct increase in the 1s-π peak (Figure 6.5), indicating that the formation of a graphitized transfer layer is occuring. Imaging of the worn surface after 300 passes shows no evidence of graphitic carbon (Figure 6.6). This is a likely result, since the graphitic carbon, if produced, would likely be in very small quantities and of a somewhat disordered nature. In order to successfully image this, the graphitic layers would have to be oriented parallel to the electron illumination for basal planes to be distinguished. An inspection of the tip after sliding shows not only worn DLC material attached to it, but indications of graphitic layering at the edge of the tip, indicated by two small arrows in Figure 6.7b. This combined with the EELS evidence strongly suggest that a graphitized tribolayer is
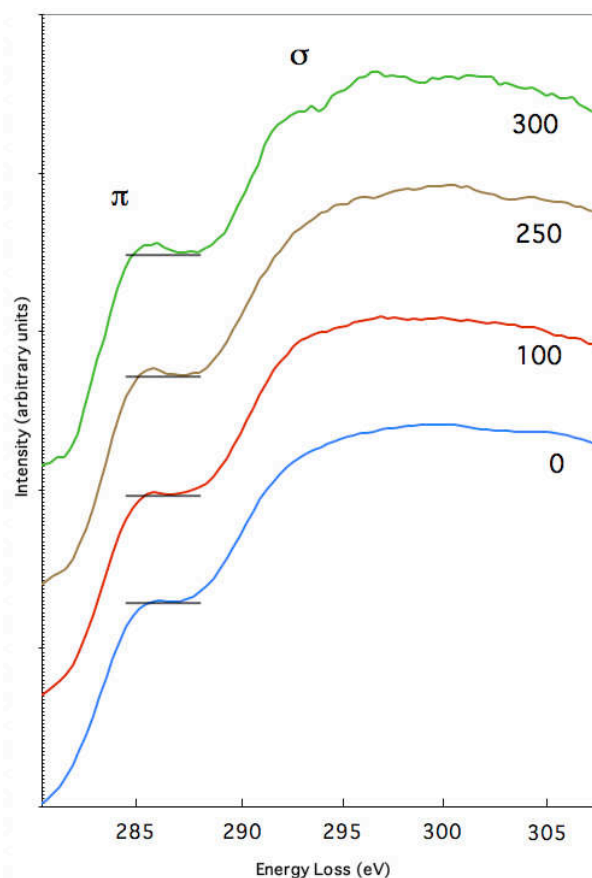
Figure 6.5. 1s near edge carbon peaks detected by EELS for NFC6 after 0, 100, 250 and 300 sliding passes with a tungsten scanning probe. An increase in the π excitation shows direct evidence of sliding-induced graphitization.

formed on 25% CH_4 - 75% H_2 DLC films (NFC6). A transformation to graphite at the sliding interface is typically accompanied by a decrease in friction in macroscopic experiments. Unfortunately, we cannot presently make any quantitative conclusions about the friction forces with the STM-holder.

NFC7 was also examined *in-situ* , and exhibited qualitatively higher friction and wear behavior. This is demonstrated in Figure 6.8, where the tungsten tip was fractured after a few hundred sliding passes. The buildup of wear particles around the tip was more
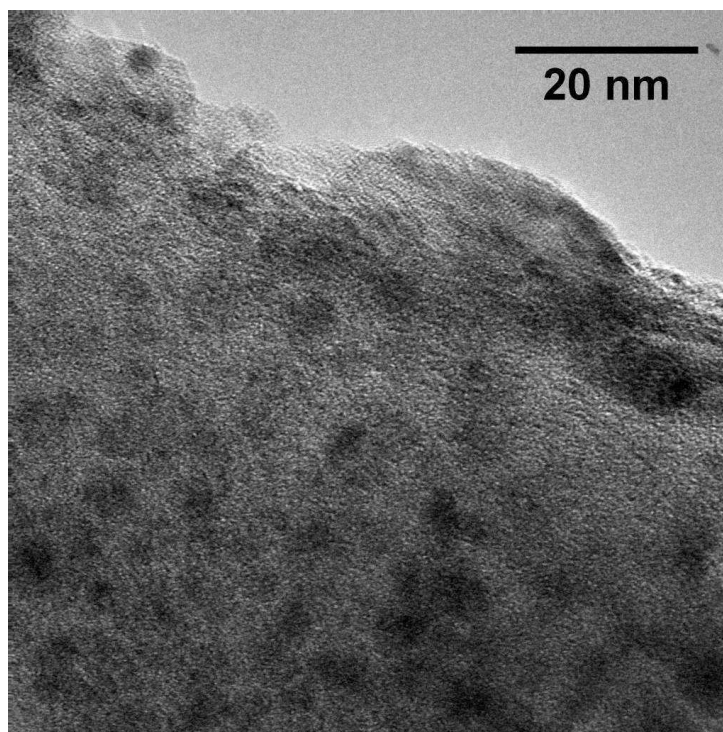
Figure 6.6. NFC6 film after 300 sliding passes.
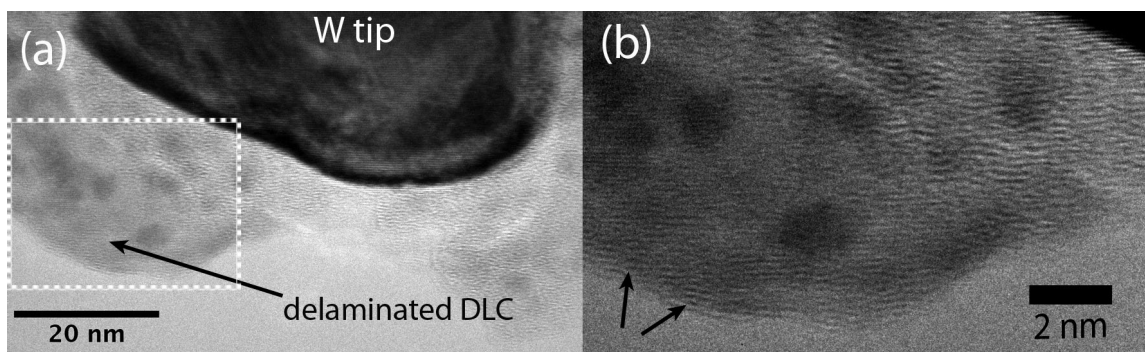
Figure 6.7. Bright field TEM of the tungsten sliding tip after several hundred scratches on NFC6.

significant than for NFC6. Figure 6.8b shows an area of the worn film after 100 sliding passes, and wear debris can be seen on the edge of the sample. It was not possible to perform a large amount of sliding before the sample detached from the copper grid. EELS
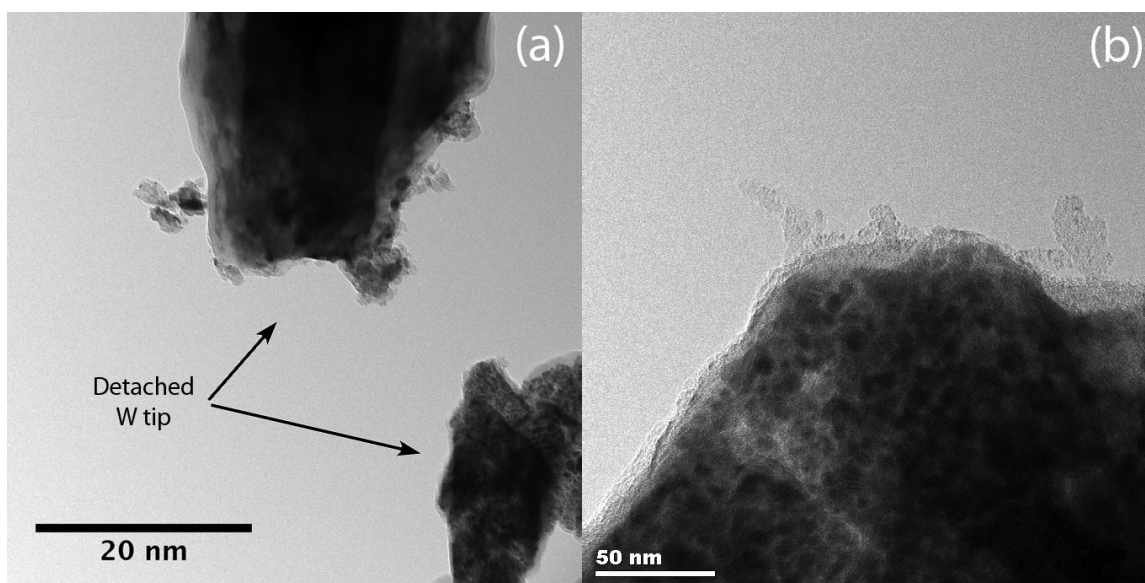
Figure 6.8. Fractured tungsten tip (a) after sliding against a DLC film (b) grown from pure methane (NFC7).

spectra were taken, after 200 sliding passes on a single region, but the noise level of the measurements prevented the carbon K-edge peaks to be adequately resolved.

6.4. Conclusions

NFC6 and NFC7 amorphous carbon films were subjected to sliding by a single asperity tungsten probe while being directly observed in the TEM. The *in-situ* EELS results (Figure 6.5) give a strong indication that a graphitized tribolayer is formed by mechanical loading (sliding). This directly supports the hypothesis that low friction properties of DLC coatings, particularly after a period of run-in, are a result of the structural change induced at asperity interfaces. No graphitization was detected on NFC7, due to experimental difficulties establishing a durable film. Qualitatively, it was observed that NFC7 was of poorer tribological performance as indicated by the rapid wear by the tungsten tip; this is in agreement with macroscopic observations on the same films. Most significantly,

we believe this study shows the first direct *in-situ* observation of grahitization of an amorphous carbon film by sliding at this length scale.

Operation of the *in-situ* STM-holder is a time-consuming and non-trivial task, and is limited in some cases by the inability to directly measure forces, and the inability of humans to have more than two arms and eyes. However, the powerful analytical capabilities of this technique, which allow a materials deformation processes to be observed dynamically, make it indispensable in detecting fundamental tribo-mechanical and tribo-chemical reactions in real time in a controlled environment.

6.5. Future Work

Having successfully demonstrated mechanically-induced graphitization of NFC6 films, it is of interest to determine what other species of low-friction amorphous carbon behave in this way. This can be achieved by the continuation of a similar EELS analysis as a function of hydrogen (gas precursor) or dopant content. It remains somewhat unclear as to the precise mechanism that gives some DLC films both low friction and low wear, but it is likely that the high hydrogen content ($\sim$40%) in NFC films is the controlling factor. Graphite, in fact, has nearly the same friction coefficients as most DLC films in humid air. The wettability of these surfaces is increased, due to the higher amounts of π bonding at the surface. This indicates that graphitized tribolayers on DLC are not the key to low friction, but likely just the opposite. Therefore, a similar *in-situ* study with a larger sampling of films with varying hydrogen contents may shed light on this issue.

Measuring or maintaining a constant normal force during the sliding in the TEM would naturally add another dimension of control to these types of experiments. By establishing a limit for the contact pressure, one can make an estimate of the mechanical energy required to induce graphitization or wear. Carrying out *in-situ* friction experiments may also be performed with a bias applied between the tip and sample, artificially heating the interface. It has been seen that at elevated temperatures, hydrogenated DLC films graphitize more readily [145], a process that can be significantly retarded with the inclusion of dopants such as silicon. A more detailed understanding of the relationship between thermal and mechanical activation at nanoscale tribological remains an unexplored area.

Sliding induced structural changes that improve the tribological properties of a material are not unique to carbon films. A recent AFM study has indicated that a composite material of amorphous molybdenum disulfide and gold shows evidence of forming a crystalline MoS_2 tribolayer after sliding[146]. The crystallization process was believed by the authors not to be a thermally activated process, considering the load and velocity conditions. However, conductive-AFM (c-AFM) was performed simultaneously during all tests at a bias of 0.012 V, which would likely serve to heat the sliding interface significantly. A similar bias was used in our investigations on gold in Chapter 5. This system presents a fine opportunity to identify the structural change associated with frictional sliding for this system via *in-situ* TEM.

CHAPTER 7

A Practical Guide to in situ STM-TEM and AFM-TEM

The day-to-day use of an in situ TEM stage brings about its fair share of quirks, difficulties, realities, and surprises along with the occasional delight. The intention of this final chapter is to catalogue in a useful way the numerous practical considerations required for using and maintaining the STM- and AFM-TEM holders. It will offer insight into sample preparation techniques, operating procedures and their accompanying pitfalls, so that future researchers need not relive the same mistakes that were learned from in this body of work. Lastly, it will address the future possibilities and extensions of the technique, with suggestions for applications in the field of tribology.

7.1. STM-TEM

7.1.1. Design and Specifications

The STM-TEM holder, drawn schematically in Figure 7.1 and picured in Figure 7.2, is designed so that an STM probe may approach and come into contact with a 3 mm disk or wire TEM sample. The wire sample holder accepts 0.35 - 0.40 mm wire, which is inserted into a platinum tube and held in place by static friction (better for soft wire). The 3 mm grid holder can replace the wire sample holder, using standard 3 mm TEM samples. The grid holder is fixed at a 30° incline, enabling simultaneous inspection by both the STM probe and electron beam. Single crystal TEM samples may in principal be used in this design, with proper handling.
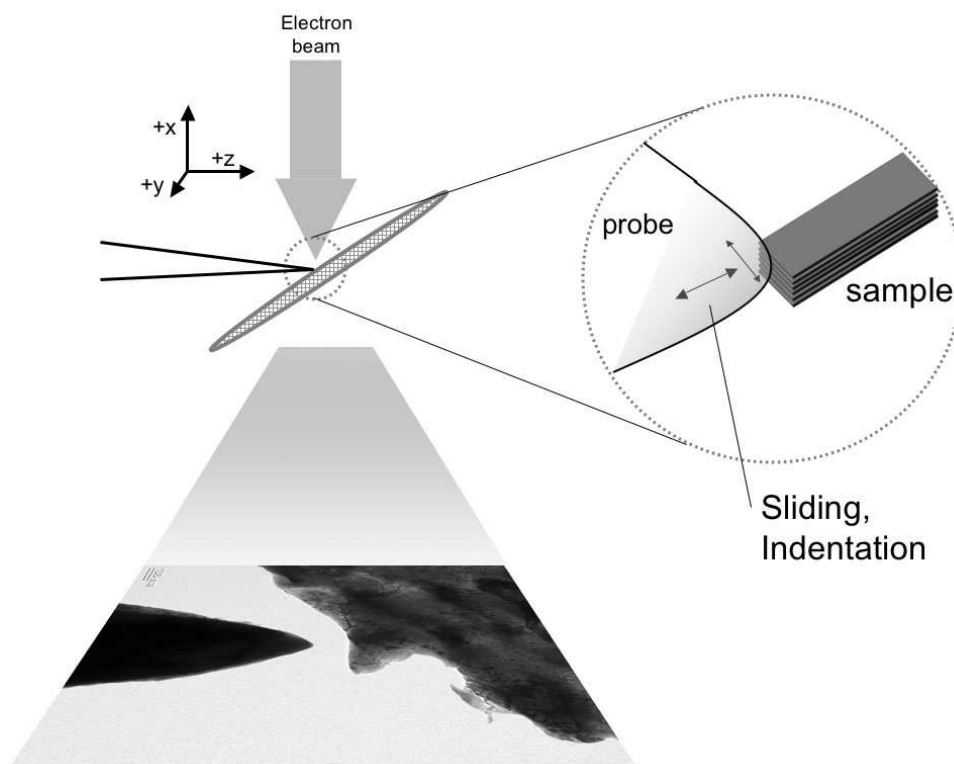
Figure 7.1.   STM-TEM holder schematic.

The holder is capable of course and fine three-dimensional control, with piezoresolutions of 0.2 in XY and 0.025 in Z. Coarse motion control gives wide ranges of motion: 12 mm in XY and 1 mm in Z. Fine motions are continuously controlled by smooth biasing of the piezo, while coarse motion is achieved by an inertial sliding mechanism that applies a short by large pulse to the piezo element, causing the hat's legs to slip along the ball. No external force should ever be applied directly to the piezo crystal, as this is the most fragile and expensive element in the device.
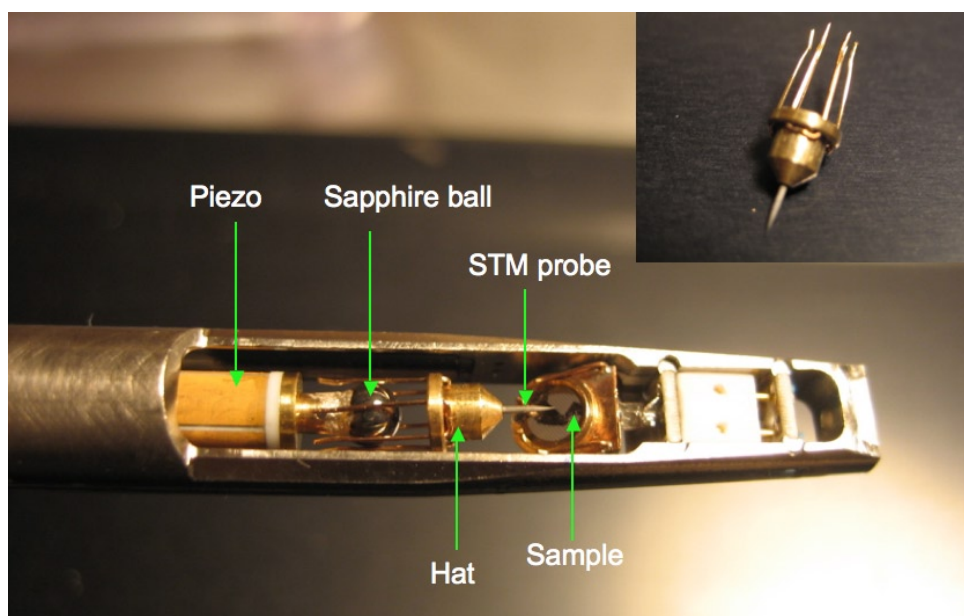
Figure 7.2. The STM-TEM holder, indicating its major components.

7.1.2. Specimen Preparation

Sample selection and preparation for the STM-TEM holder involves both the preparation of thin TEM samples and sharp probes. Chapters 4-6 mentioned the basics of sample preparation used in the experiments, but failed to convey the delicate art of sample preparation. Now we will address the details of making the ideal samples for use in the STM-TEM, beginning with the fabrication of probes.

Tungsten, silver and gold wire (0.25 mm diameter) were used in operation with the STM-TEM. The simplest method for making wire samples is a cutting an pulling technique. This only works well with soft metals, such as gold and silver. A pair of sharp handheld wire cutters are held at an angle to the wire and a sudden combination of clamping (cutting) and pulling away from the ends of the wire will produce in some cases a fairly small protruding tip, sufficient for basic STM operation. Operation in the TEM,

however is less than ideal with this method. Since the opposing sample sits at an angle to the tip, there is a reasonably high probability that the interface will be shadowed by the blunt region of the wire. Therefore, this method was only employed during ex situ operation of the holder.

Electrochemical etching (electropolishing) is a technique that can produce very sharp, spatially isolated (high aspect ratio) tips for a wide variety of materials. This is the method of choice for most serious scanning probe techniques. 0.25 mm tungsten wire (99.995% purity) was electropolished in a 1 N NaOH solution using an alternating current supply in the range of 0.1 and 5.0 V. A two-step process was carried out, in a manner identical to the fabrication of sharp atom probe microscope samples. The wire is first blanked by vertical insertion to a depth of a few millimeters into the electrolyte solution, with a well-type counter electrode on either side of the tip. The blanking process removes material quite rapidly, and prepares it for the second stage. The tip is then transferred under an optical microscope where it is barely inserted through a thin wire loop (3 mm diameter), containing a drop of electrolyte held in place by surface tension. Lower biases are then applied, with decreasing strength as the sample thins. Etching rates are inversely proportional to the local radius of the material. The wire loop serves to create a necked region near the end of the blanked tip. Once the necked region is noticeably thinner (by optical microscopy) than the regions to either side, the sample is transferred to the original blanking station. Here it is very slowly pulsed, at voltages in the range of 0.1 mV and below until the necked region is thinned to the point where the excess material falls from the sample. It is absolutely essential to cut the potential as quickly as possible once the break has been made. Further polishing at this point will only lead to blunting of
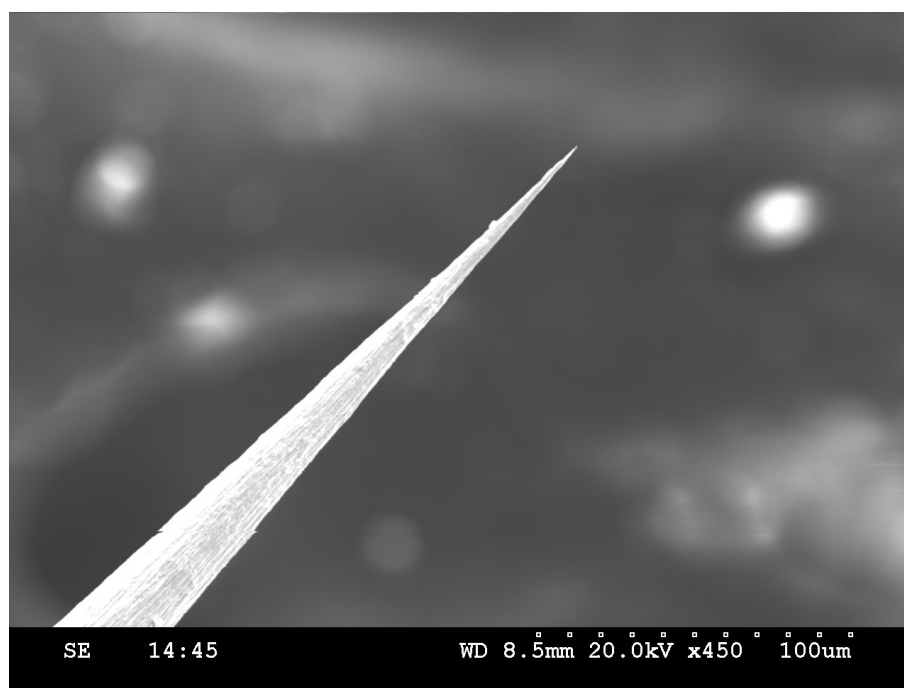
Figure 7.3. SEM image of high aspect ratio tip geometry

the tip. The sample is quickly removed from the electrolyte solution and gently rinsed in ethanol for one minute. A variety of tip shapes and sizes may result from this technique, as illustrated by SEM and TEM micrographs in Figures 7.3 and 7.4. The smallest tips that were achieved by this method, were tungsten probes with a minimum diameter of 5 nm.

The electropolishing method described above is ideal for producing high aspect ratio tips as seen in Figure 7.3. For *in-situ* STM-TEM work, we have found that these are the most useful, because the opposing sample sits not perpendicular, but at an inclined angle to the axis of the probe. It is a common experience that during STM-TEM operation the body of the probe away from the tip region contacts the sample in an unknown or shadowed area on the sample. This problem can be avoided by producing high aspect
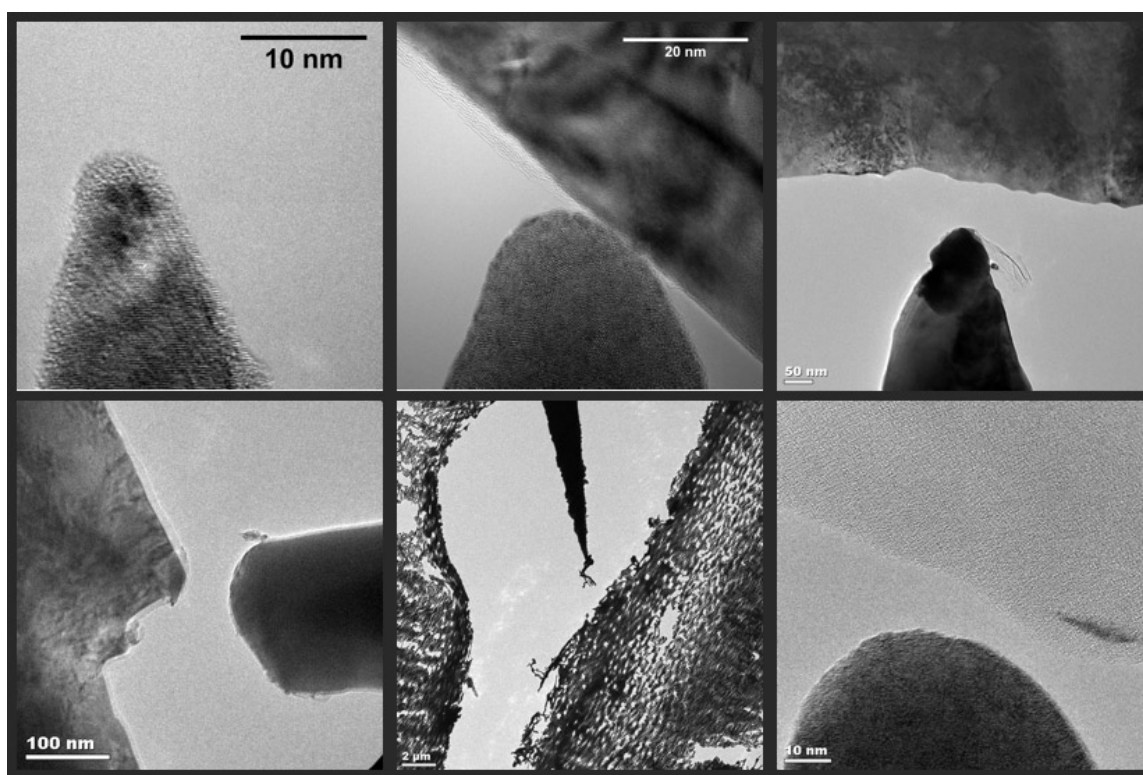
Figure 7.4. TEM micrographs of a variety of tungsten tips fabricated by standard electropolishing.

ratio tips. The tradeoff, of course, is a reduction in mechanical rigidity of the tip. It is largely for this reason that tungsten was chosen as the tip material in our studies. In the STM community, however, it is common to use a variation on this fabrication technique in order to produce low aspect ratio tips for increased mechanical stability and decreased thermal drift. Also, line-of-sight shadowing is not a concern for conventional STM. Gold tips are not suitable for the same electropolishing technique as carried out for tungsten, for reasons of mechanical stability. The method for creating low aspect ration tips is summarized as follows. The gold wire is suspended vertically in a beaker containing a concentrated hydrochloric acid solution and a platinum wire loop. The end of the wire is

covered in nail polish to prevent etching. The entire process is carried out in this position, forcing the etching to occur only in a localized region. Once the portion of wire with the nail polish attached falls from the sample, the current is cut, and the sample is removed and rinsed in alcohol. Advanced methods exist that monitor the polishing current in order to know when to interrupt the potential, but were not used. Instead, a novel method for fabricating ultrafine gold probes *in-situ* was developed.

Starting with an electropolished tungsten probe (r $\sim$ 50 nm) and a thin gold TEM sample both mounted in the STM-TEM holder, a series of short bias pulses of several volts (no more than 8V) are applied for 100 msec while in contact with the gold sample. After cleaning the interface of hydrocarbon contaminants, this will locally melt the contact region, typically coating the tip with gold. The tip is then retracted and allowed to cool for one minute. With a small bias of 100 mV applied to the tip, the cleaned region exhibits liquidlike behavior as described in Chapter 5. By exploiting gold's liquid-like properties, repeated contacts and pull-off sequences will yield the formation of very sharp asperities, with tip radii as low as 2 nm (Figure 5.8). This high resolution fabrication process benefits from greater control and repeatibility than traditional blind electropolishing techniques. The benefits of having such small tips are abundant for local electronic characterization of nanostructures. There also exists the possibility of attaching small particles to the ends of tips for study of electronic, mechanical and structural properties. One direct field of applicability is tip-enhanced raman spectroscopy (TERS).

Once the tips are fabricated, they must be inserted in to the hat, which serves as the tip's support. Version 1 of the hats have a 0.3 mm hole drilled through the axis of the hat, in which soft, ductile wire (silver or gold) can be inserted and sufficiently held in

place by slight bending of the wire after insertion. Tungsten wire, however, does not bend easily, and slides quite readily through this opening. At times when it does stay fixed, excessive inertial stick-slip motion of the tip once mounted on the holder can cause the probe to become dislodged. For this reason, version 2 of the hat has implemented two small set screws that may be tightened after a wire has been inserted. Although this is a delicate process, it improves the reliability of using stiffer, less ductile materials as tips (e.g. tungsten). An improvement of this design would be a clamp mechanism to prevent overhandling.

The STM-TEM holder is properly outfitted to handle conventional 3 mm TEM samples. The only requirement being that it is set in a ring holder mounted at 30 degrees from the ZY plane. This enables essentially all traditional TEM sample preparation methods to be used. It is worth describing the technique used in chapter 4 to prepare graphite samples, as this was slightly less conventional and may serve as a learning tool.

Highly ordered pyrolytic graphite (HOPG) TEM samples can be prepared by a sequential cleaving process to optical translucency. Cleaving is accomplished with adhesive (scotch) tape, which is used to delaminate sheets of graphite. A separate fresh piece of tape may be used to thin the flakes again until some noticeably translucent to the eye. At this point, it is necessary to remove any excess tape where graphite is not present. It is then immersed into a bath of toluene for approximately 5 minutes, allowing the backing to loosen from the glue. Once this process has begun, slowly adding methanol will help to completely remove the backing. Once this has been accomplished, possibly with the aid of tweezers, it is important to remove any floating plastic, as this will only serve as a contaminant. Acetone can then be added to dissolve the glue-graphite compound. Not
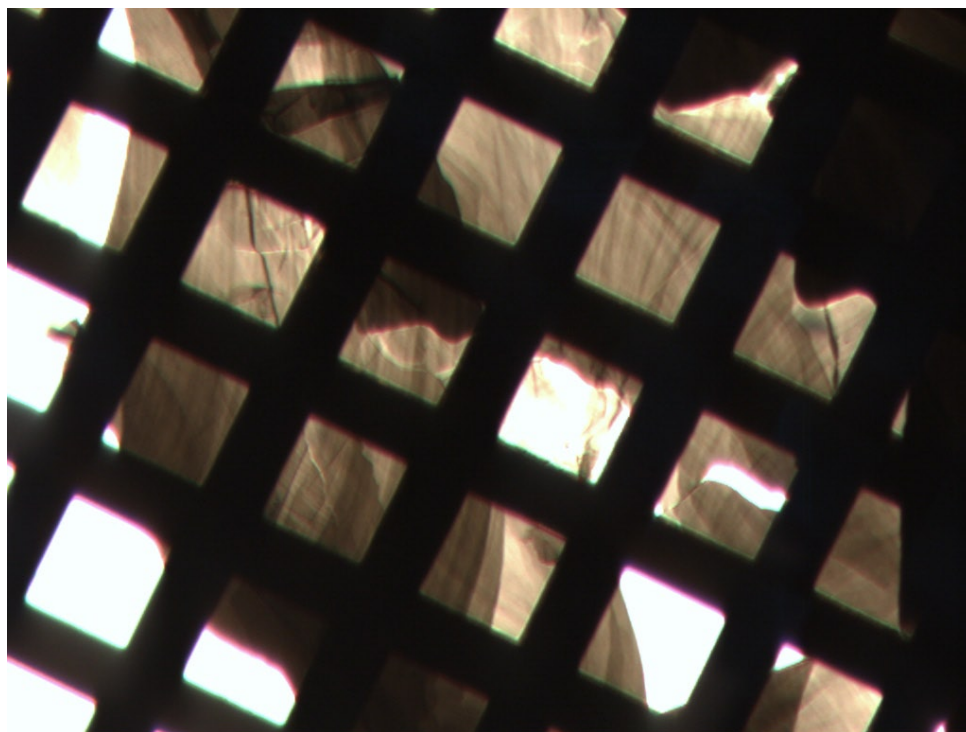
Figure 7.5. Optical micrograph of HOPG on a Cu TEM grid (200 mesh).

all the graphite will separate from the glue, but several dozen graphite particles should now be floating in solution. After decanting excess solvent and diluting with fresh acetone will remove any excess glue found on the tapes. Now the flakes may be fished from the solution using standard metal TEM grids, and set out to dry. It was found that many graphite samples had difficulty remaining attached to the grids over longer periods of time, due mostly due to charge buildup in the dry winter months. If the samples appear grey or clear under an optical microscope with transmitted light, they will be suitable for investigation in the TEM, as shown in Figure 7.5. Wire samples may be used as well; this is particularly relevant when studying elongated nanostructures (nanotubes, nanowires) [125, 124].

7.1.3. Operation

Albeit technically a functional STM system, the holder excels more as a nanomanipulation and local biasing tool. Nonetheless, it was tested *ex situ* for its STM imaging capabilities. Figure 7.6 shows a weakly resolved basal plane of graphite including significant line scan artifacts. The features agree with the hexagonal spacing of graphite and was verified as a real feature by changing the scan angle, where it appeared as well. This acquisition was achieved in constant current mode at 1 nA and a tip-sample bias of 100 mV. This image was acquired outside the TEM column, in air using a clipped silver wire as a probe. This verified the quoted resolution capabilities of the STM unit. Imaging inside the TEM was not characterized, as was not necessary for the current studies. Some attempts, however, showed significant sensitivity to the electron illumination and contamination. Thin TEM samples with a small amount of contamination will be bent substantially while the feedback mechanism is searching, often to the point of fracture.

The following will describe some basic procedures related to operating the instrument inside the TEM column.

Insertion into the TEM requires an extended pumping period, on the order of 10 minutes to ensure the hollow electrical feed-through cavities are properly evacuated. Once inside the TEM, and after connecting the control electronics, the tip and sample will likely be separated by a great distance. When mounting the tip, it is a good idea to ensure ample space between tip and sample, as the process of inserting the holder into the microscope will inevitably jostle the tip a small amount. In addition to this, when the power supply is connected and turned on, the piezo elements are reset, which may lead to a change in the position of the tip. Having located the tip and sample, the two most important
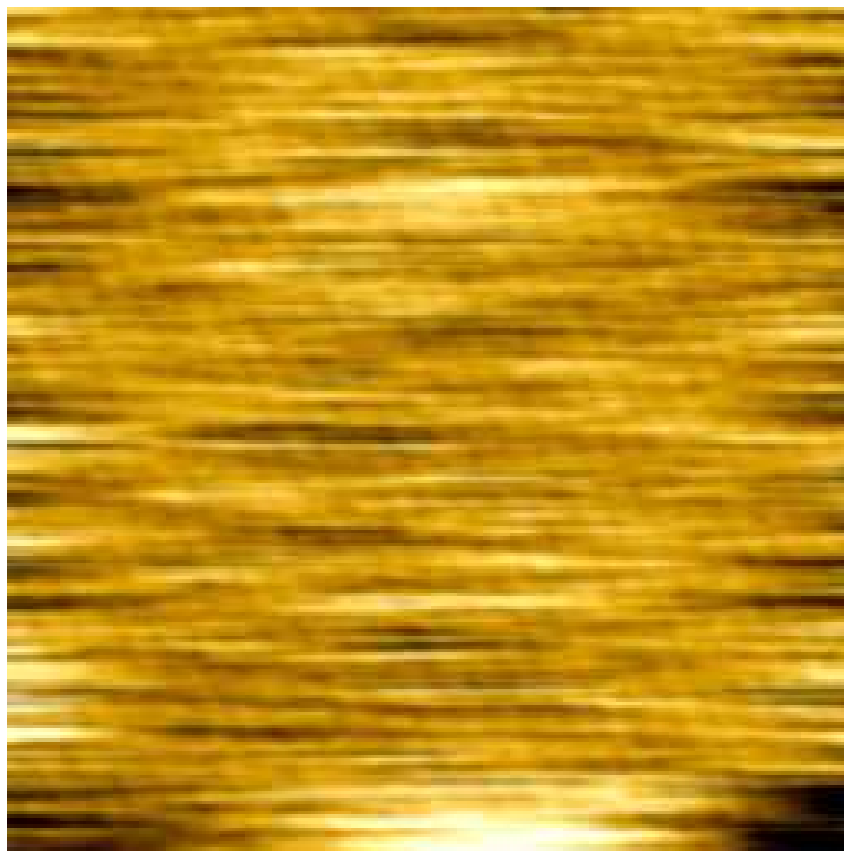
Figure 7.6.   6x6 nm STM topograph of cleaved HOPG surface in air, faintly resolving the atomic basal plane.

pieces of information to remember are (1) that if using a grid sample, you must always remember that the sample is tilted and (2) that not all movements with the inertial slider are reversible. Regarding point (1), this imposes not only tip-sample alignment issues, but presents a TEM column alignment issue. A 3 mm sample tilted at 30 degrees corresponds to a vertical variation (X direction in Figure 7.1) of 1.5 mm. This is not an insignificant vertical displacement, and will require realignment of the column even after moderate ZY displacements. This can be a great source of wasted instrument time.

After locating a region of interest on the sample and setting the eucentric height, it is necessary to move the probe to this location. This is carried out through a computer interface (NFControl, Nanofactory Instruments), which has separate controls for macroscopic (inertial) and microscopic (piezo) movements. Although somewhat robust, this method may be improved upon with the implementation of a joystick, for it is most crucial to keep one's attention on the sample and not the computer screen controls. Approaching the region of interest is best achieved while modulating the alpha tilt ("wobbler" for FEI). This gives some depth perception and, with some practice, can be a rather quick and efficient way to safely approach the sample. Once the projected wobble amplitudes are equal between tip and sample, one is typically within microns of alignment. The remainder of the vertical alignment must then be accomplished by Fresnel fringe comparison between the tip and sample, and subsequent adjustment of the piezo controls on the STM unit.

7.1.4. Pitfalls

A number of complications may arise during the operation of the STM-TEM system, which are listed here in an attempt to prepare future users.

- Noise levels, read from the digital ammeter, can spontaneously jump to tens of nA or, more severely, to the maximum pre-amplified setting of $\sim$450 nA, at the lowest setting). This can range from surprising to disastrous, when working with a delicate sample. The noise was found to be cured by the elusive "magic touch" - a flakey connection on the preamplifier, where the incoming cable connecting from the main power supply is attached. Readjusting this usually eliminates the problem. Alternatively, it was found that occasionally resetting the power supply

unit helps this disappear, although it is likely not the recommended solution from Nanofactory, and certainly not recommended when the tip and sample are in contact.

- Contamination can play a major role in observing surface interactions. It is therefore recommended to use a clean microscope, and liquid nitrogen trap whenever possible.

- Mostly isolated to version 1 hats, the inertial motion was somewhat unpredictable. The XYZ coordinates of the STM are never equivalent to XYZ of the TEM column, and can present challenges to the operator's intuition. More seriously, the retract (-Z) motion of the inertial slider often failed. This seems to have been corrected in version 2, but it remains a function of the alignment and cleanliness of the legs that surround the sapphire ball. If these are damaged or contaminated with third bodies, erratic motion may result. It is useful to keep in mind, erring on the side of safety, that one usually can approach the sample successfully, but retracting is less reliable.

7.2. AFM-TEM

The AFM-TEM holder designed by Nanofactory Instruments represents the next generation of *in-situ* holders for microstructural characterization in the TEM. Not only does it enable the characterization of tip-sample interactions, tip shape, and contact area - all of which are somewhat unknown in conventional scanning probe techniques - but it combines these with the ability to measure forces in the nanonewton range. The following discussion will discuss the implementation of this technique to measure mechanical and
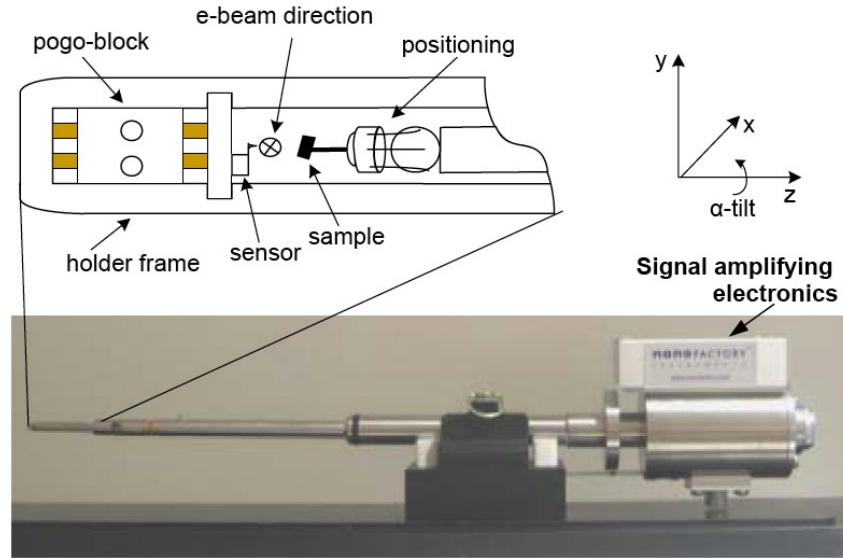
Figure 7.7. Schematic of the AFM-TEM holder design (courtesy of A. Nafari, Nanofactory Instruments).

tribological properties of materials on the nanoscale. Disclaimer: As the AFM-holder available to us is the first produced copy of its kind and remains under development, I am bound not to share all details of electronic and sensor specifications.

7.2.1. Design and Specifications

The Nanofactory AFM-TEM holder (Figure 7.7) is derived from the STM-TEM holder, with a few notable differences. In place of the sample holder on the STM-TEM, the AFM-TEM employs a microfabricated force sensor. This unit is a self-contained microfabricated device with a silicon force-sensing 'springboard' cantilever. Its dimensions are illustrated schematically in Figure 7.8. The one square millimeter device is bonded to a ceramic printed circuit board (PCB), which can be inserted and removed manually with a pair of tweezers. However, during operation of the instrument, this element is stationary, in an effort to improve the mechanical stability of the force sensing mechanism.
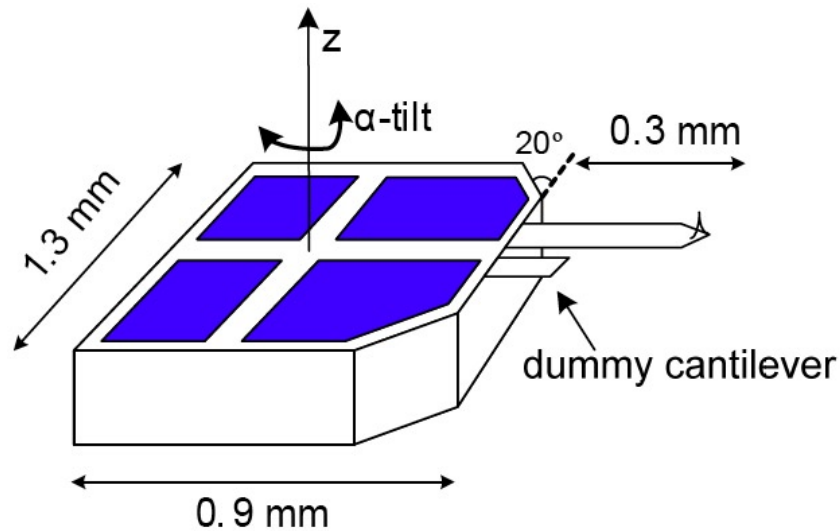
Figure 7.8. Schematic of the microfabricated TEM sensor (courtesy of A. Nafari, Nanofactory Instruments).

The sensor employs piezoresistive elements arranged in a Wheatstone bridge to enable a high degree of sensitivity with normal force resolution of 110 nN as measured over a 1 μN range (Figure 7.9). The multi-stage fabrication process involved micromachining of an n-type SOI wafer, and the silicon tip was sharpened by a thermal oxidation process. The resistive elements were doped with boron at an energy of 50 keV at a dose of $1.5 \cdot 10^{14}$ - $1.5 \cdot 10^{15}$ cm^{-2}. Optimal tip radii are approximately 100 nm, but are occasionally damaged. The thickness of the cantilevers range from 2.5-5 μm, leading to spring constants between 0.5 and 3 N/m. The uneven boron distribution during the doping process lead to problems with current leakage, which has manifested itself in higher than expected noise levels. This may also be related to the cause of drift when exposed to the electron beam.

7.2.2. Specimen Preparation

Specimen preparation is non-trivial task for this holder. Due to the geometric constraints of the force sensor, the use of a tilted 3 mm TEM grid is effectively out of the question. This leaves a few options. Wire samples are most likely to result in successful contact between sensor and sample. This leaves somewhat to be desired for tribological experimentation unless the end of the wire sample consists of nanowire or tubes, which are point contacts and most suitable for indentation experiments. For sliding experiments, samples must be fabricated that are electron transparent in one dimension (X), long in one dimension (Z), and moderately short in the other (Y), so as to reduce the possibility of crashing into the sensor or PCB. Short wedge samples (modified from Si "H" bars) may be a solution to this. A segment of a TEM grid may be used, if attached to a wire and tilted first about the Y axis and then about the Z axis. This would make it possible to investigate more than a single area on a given sample, with a range of a few hundred microns.

7.2.3. Operation

Here we will describe the basic operation of the AFM-TEM. Since the PCB contains electrical connections which are passed through the length of the holder shaft. Because of this, there is a significant volume of hollow space in the shaft of the holder (as with the STM-TEM holder), requiring somewhat longer evacuation times before use. In the case of the Tecnai F20ST, we found that a pumping time of ten minutes was sufficient before complete insertion.

The acquisition of AFM topographs is possible in scanning feedback mode, however the primary utility of the instrument is for local manual deformation and force sensing. Eventually, we see the ability to aquire AFM topographs as a powerful complement to projected TEM images, so that one is able to obtain reasonably accurate height information.

Despite its limitations, a time saving benefit to having the AFM sensor as a stationary element is that the eucentric height must only be set once. This contrasts the STM-TEM design, where the combination of a tilted sample and movable probe required a realignment whenever the stage was moved in the ZY plane. Samples must be accommodated on the inertial slider (hat), held in place by a wire or grid clamp. The inertial sliding mechanism (ball and hat configuration) is identical to the STM holder. Consequently, there may be more weight at the end of the wire from the mounted sample, the inertial sliding motion may behave somewhat erratically.

Normal force plots may be obtained as seen in Figure 7.9. A sample is moved at a constant speed towards the cantilever tip to a set maximum force or distance while the change in resistance of the cantilever is measured and converted to a force. Figure 7.9 shows a RMS noise level of ± 110 nN. Typical 'snap-out' behavior can be seen in the light gray line where the sample is being retracted. 'Snap-in' behavior is not resolved on approach for reasons of resolution and surface contamination.
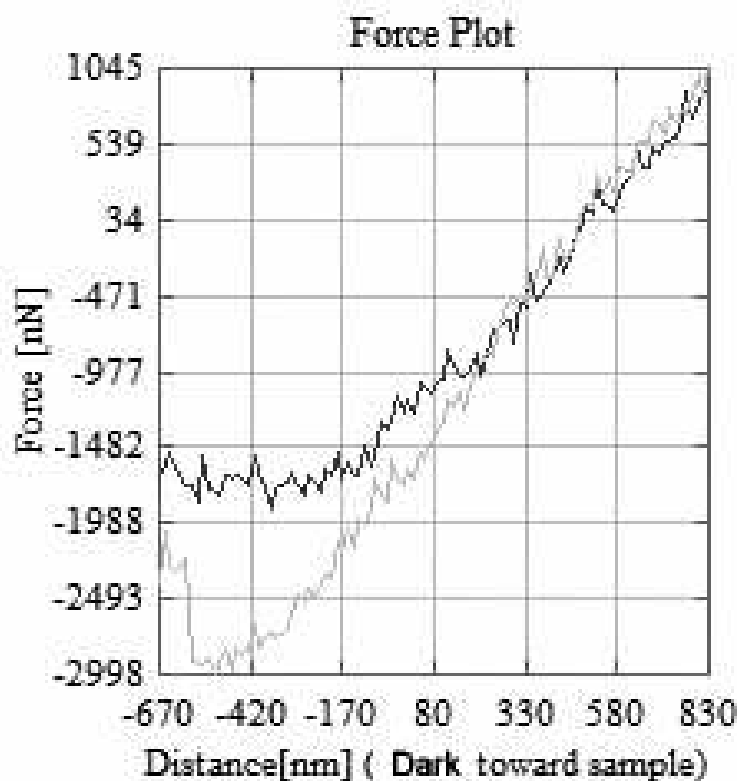
Figure 7.9. Normal force curve for approach, contact and retraction of the AFM tip from a sample

7.2.4. Pitfalls

This section will highlight some of the practical challenges in operating the AFM-TEM holder, with the hope that its limitations are properly considered and that realistic experiments may be successfully carried out with this instrument in the future. Since sample preparation has already been discussed, nothing more will be said here, but it is worth emphasizing that the second 'sample' - the AFM tip - is extremely limited in both geometry (e.g. tip radius), composition and cleanliness. It is possible to coat the cantilever with a thin film, but this goes not without significant risk, as the effects of deposition on the

entire sensor are likely not favorable. Ideally, the entire sensor minus the tip region would be shadowed by a mask during a deposition process, preferably run at room temperatures.

The silicon cantilever is susceptible to severe drift when illuminated by a converged electron beam. This has been seen to cause detrimental oscillations in the feedback loop while establishing contact. Something to consider in the fabrication of the sensors is the effect of doping on this behavior. The interaction between the beam and cantilever might be significantly reduced if the proper levels of doping are introduced during the silicon microfabrication process.

Ten sensors are to be supplied by Nanofactory with a noise level of 10 nN or better. The sensors available to us currently (3 ct.) function with a 100 nN RMS noise floor and moderately defined tip radii.

References

[1] D. Dowson. *History of tribology.* Professional Engineering Publishing, London, 2nd edition, 1998.

[2] M. Dienwiebel, G. S. Verhoeven, N. Pradeep, J. W. M. Frenken, J. A. Heimberg, and H. W. Zandbergen. Superlubricity of graphite. *Physical Review Letters*, 92(12), 2004.

[3] J. Robertson. Diamond-like amorphous carbon. *Materials Science and Engineering R-Reports*, 37(4-6):129–281, 2002.

[4] J.C. Sanchez-Lopez, A. Erdemir, C. Donnet, and T.C. Rojas. Friction-induced structural transformations of diamondlike carbon coatings under various atmospheres. *Surface and Coatings Technology*, 163-164:444–450, 2003.

[5] H. P. Jost. Tribology - origin and future. *Wear*, 136(1):1–17, 1990.

[6] ASME. Strategy for energy conservation through tribology. *ASME*, November 1977.

[7] H. P. Jost. The tasks of tribology societies on a changing world. *Opening Address, Second World Tribology Congress*, September 2001.

[8] D. H. Buckley. Use of analytical surface tools in fundamental study of wear. *Wear*, 46(1):19–53, 1978.

[9] B. Q. Luan and M. O. Robbins. The breakdown of continuum models for mechanical contacts. *Nature*, 435(7044):929–932, 2005.

[10] G. Binnig, C. F. Quate, and C. Gerber. Atomic force microscope. *Physical Review Letters*, 56(9):930–933, 1986.

[11] C. M. Mate, G. M. McClelland, R. Erlandsson, and S. Chiang. Atomic-scale friction of a tungsten tip on a graphite surface. *Physical Review Letters*, 59(17):1942–1945, 1987.

[12] M. Dienwiebel, N. Pradeep, G. S. Verhoeven, H. W. Zandbergen, and J. W. M. Frenken. Model experiments of superlubricity of graphite. *Surface Science*, 576(1-3):197–211, 2005.

[13] M. Hirano and K. Shinjo. Superlubricity and frictional anisotropy. *Wear*, 168(1-2):121–125, 1993.

[14] E. Gnecco, R. Bennewitz, T. Gyalog, C. Loppacher, M. Bammerlin, E. Meyer, and H. J. Guntherodt. Velocity dependence of atomic friction. *Physical Review Letters*, 84(6):1172–1175, 2000.

[15] J. Hu, X. D. Xiao, D. F. Ogletree, and M. Salmeron. Atomic-scale friction and wear of mica. *Surface Science*, 327(3):358–370, 1995.

[16] R. Bennewitz, T. Gyalog, M. Guggisberg, M. Bammerlin, E. Meyer, and H. J. Gntherodt. Atomic-scale stick-slip processes on cu(111). *Physical Review B*, 60(16):R11301, 1999.

[17] L. Howald, H. Haefke, R. Lüthi, E. Meyer, G. Gerth, H. Rudin, and H. J. Güntherodt. Ultrahigh-vacuum scanning force microscopy: Atomic-scale resolution at monatomic cleavage steps. *Physical Review B*, 49(8):5651, 1994.

[18] R. W. Carpick, Q. Dai, D. F. Ogletree, and M. Salmeron. Friction force microscopy investigations of potassium halide surfaces in ultrahigh vacuum: structure, friction

and surface modification. *Tribology Letters*, 5(1):91–102, 1998.

[19] G. J. Germann, S. R. Cohen, G. Neubauer, G. M. McClelland, H. Seki, and D. Coulman. Atomic scale friction of a diamond tip on diamond (100)-surface and (111)-surface. *Journal of Applied Physics*, 73(1):163–167, 1993.

[20] J.N. Israelachvili and D. Tabor. Measurement of vanderwaals dispersion forces in range 1.5 to 130 nm. *Proceedings of the Royal Society of London Series a-Mathematical and Physical Sciences*, 331(1584):19, 1972.

[21] D. Tabor and R. Winterton. Direct measurement of normal and retarded van der waals forces. *Proceedings of the Royal Society of London Series a-Mathematical and Physical Sciences*, 312(1511):435, 1969.

[22] S. Granick. Motions and relaxations of confined liquids. *Science*, 253(5026):1374–1379, 1991.

[23] J. Krim, D. H. Solina, and R. Chiarello. Nanotribology of a kr monolayer - a quartz-crystal microbalance study of atomic-scale friction. *Physical Review Letters*, 66(2):181–184, 1991.

[24] M. Cieplak, E. D. Smith, and M. O. Robbins. Molecular-origins of friction - the force on adsorbed layers. *Science*, 265(5176):1209–1212, 1994.

[25] A. Dayo, W. Alnasrallah, and J. Krim. Superconductivity-dependent sliding friction. *Physical Review Letters*, 80(8):1690–1693, 1998.

[26] R. L. Renner, P. Taborek, and J. E. Rutledge. Friction and pinning of nitrogen films on lead substrates near the superconducting transition. *Physical Review B*, 63(23), 2001. 233405.

[27] G A Tomlinson. *Philos. Mag.*, 7:905, 1929.

[28] T. Frenkel and Y. I. Kontorova. *Zh. Eksp. Teor. Fiz.*, 8, 1938.

[29] U. Landman, W. D. Luedtke, N. A. Burnham, and R. J. Colton. Atomistic mechanisms and dynamics of adhesion, nanoindentation, and fracture. *Science*, 248(4954):454–461, 1990.

[30] E. D. Smith, M. O. Robbins, and M. Cieplak. Friction on adsorbed monolayers. *Physical Review B*, 54(11):8252–8260, 1996.

[31] B. Q. Luan and M. O. Robbins. Contact of single asperities with varying adhesion: Comparing continuum mechanics to atomistic simulations. *Physical Review E*, 74(2), 2006. Part 2026111.

[32] G. He, M. H. Muser, and M. O. Robbins. Adsorbed layers and the origin of static friction. *Science*, 284(5420):1650–1652, 1999.

[33] M. O. Robbins and E. D. Smith. Connecting molecular-scale and macroscopic tribology. *Langmuir*, 12(19):4543–4547, 1996.

[34] P. A. Thompson and M. O. Robbins. Origin of stick-slip motion in boundary lubrication. *Science*, 250(4982):792–794, 1990.

[35] P. A. Thompson and S. M. Troian. A general boundary condition for liquid flow at solid surfaces. *Nature*, 389(6649):360–362, 1997.

[36] A. Buldum and S. Ciraci. Atomic-scale study of dry sliding friction. *Physical Review B*, 55(4):2606–2611, 1997.

[37] Martin H. Müser, Ludgar Wenning, and Mark O. Robbins. Simple microscopic theory of amontons's laws for static friction. *Phys. Rev. Lett.*, 86(7):1295–1298, Feb 2001.

[38] M. D. Perry and J. A. Harrison. Molecular dynamics studies of the frictional properties of hydrocarbon materials. *Langmuir*, 12(19):4552–4556, 1996.

[39] E. B. Tadmor, R. Phillips, and M. Ortiz. Mixed atomistic and continuum models of deformation in solids. *Langmuir*, 12(19):4529–4534, 1996.

[40] E. B. Tadmor, M. Ortiz, and R. Phillips. Quasicontinuum analysis of defects in solids. *Philosophical Magazine a-Physics of Condensed Matter Structure Defects and Mechanical Properties*, 73(6):1529–1563, 1996.

[41] J. P. Gao, W. D. Luedtke, D. Gourdon, M. Ruths, J. N. Israelachvili, and U. Landman. Frictional forces and amontons' law: From the molecular to the macroscopic scale. *Journal of Physical Chemistry B*, 108(11):3410–3425, 2004.

[42] M. Weiss and F. J. Elmer. Dry friction in the frenkel-kontorova-tomlinson model: dynamical properties. *Zeitschrift Fur Physik B-Condensed Matter*, 104(1):55–69, 1997.

[43] F. Frank and J. H. van der Merwe. *Proc. R. Soc. London Ser. A*, 198:205, 1949.

[44] F. Frank and J. H. van der Merwe. *Proc. R. Soc. London Ser. A*, 198:217, 1949.

[45] M. Weiss and F. J. Elmer. Dry friction in the frenkel-kontorova-tomlinson model: Static properties. *Physical Review B*, 53(11):7539–7549, 1996.

[46] J. A. Harrison, C. T. White, R. J. Colton, and D. W. Brenner. Molecular-dynamics simulations of atomic-scale friction of diamond surfaces. *Physical Review B*, 46(15):9700–9708, 1992.

[47] U. Landman and W. D. Luedtke. Nanomechanics and dynamics of tip substrate interactions. *Journal of Vacuum Science and Technology B*, 9(2):414–423, 1991. Part 2.

[48] V. I. Alshits, editor. *Dislocation Dynamics and Mechanical Properties of Crystals*, volume 31 of *Progress in Materials Science*. Elsevier Science, Amsterdam, 1992.

[49] A. P. Sutton and R. W. Balluffi. *Interfaces in Crystalline Materials*. Monographs on the Physics and Chemistry of Materials. Oxford University Press, Oxford, 1995.

[50] D. Wolf and S. Yip, editors. *Materials interfaces. Atomic-level structure and properties*. Chapman and Hall, London, 1992.

[51] J.M. Howe. *Interfaces in materials*. Wiley, New York, 1997.

[52] J. Weertman and J. R. Weertman. *Elementary Dislocation Theory*. Oxford University Press, Oxford, 2 edition, 1992.

[53] J. P. Hirth and J. Lothe. *Theory of Dislocations*. Krieger Publishing Company, Malabar, 2 edition, 1982.

[54] E. Barthel. On the description of the adhesive contact of spheres with arbitrary interaction potentials. *Journal of Colloid and Interface Science*, 200(1):7–18, 1998.

[55] K.L. Johnson, editor. *Contact Mechanics*. Cambridge University Press, Cambridge, 1985.

[56] W. N. Unertl. Implications of contact mechanics models for mechanical properties measurements using scanning force microscopy. *Journal of Vacuum Science and Technology A*, 17(4):1779–1786, 1999. Part 2.

[57] W. Bollmann. On geometry of grain and phase boundaries .i. general theory. *Philosophical Magazine*, 16(140):363, 1967.

[58] W. Bollmann. On geometry of grain and phase boundaries .2. applications of general theory. *Philosophical Magazine*, 16(140):383, 1967.

[59] H. Grimmer, W. Bollmann, and Warringt.Dh. Coincidence-site lattices and complete pattern-shift lattices in cubic-crystals. *Acta Crystallographica Section A*, A 30(MAR):197–207, 1974.

[60] G. Leibfried. *Z. Phys.*, 127:344, 1950.

[61] V. L. Indenbom and A. N. Orlov. Modern concepts of dislocation mobility. In *Proc. Conf. Dislocation Dynamics*, page 3, Kharkov, 1967.

[62] S. V. Lubenets and Startsev V. I. *Sov. Phys. Solid State*, 10:15, 1968.

[63] V. I. Alshits. Phonon-wind and dislocation damping. *Soviet Physics Solid State,Ussr*, 11(8):1947, 1970.

[64] V. I. Alshits and Y. M. Sandler. Flutter mechanism of dislocation drag. *Physica Status Solidi B-Basic Research*, 64(1):K45–K49, 1974.

[65] T. Holstein. *Physical Review*, 151:187, 1966.

[66] G. A. Alers, O. Buck, and B. R. Tittmann. Measurements of plastic flow in superconductors and electron-dislocation interaction. *Physical Review Letters*, 23(6):290, 1969.

[67] H. Kojima and T. Suzuki. Electron drag and flow stress in niobium and lead at 4.2 degrees k. *Physical Review Letters*, 21(13):896, 1968.

[68] A. Hikata and C. Elbaum. Ultrasonic attenuation in normal and superconducting lead - electronic damping of dislocations. *Physical Review Letters*, 18(18):750, 1967.

[69] B. R. Tittmann and H. E. Bommel. Amplitude-dependent ultrasonic attenuation in superconductors. *Physical Review*, 151(1):178, 1966.

[70] W. P. Mason. Effect of electron-damped dislocations on determination of superconducting energy gaps of metals. *Physical Review*, 143(1):229, 1966.

[71] G. P. Huffman and N. Louat. Interaction between electrons and moving dislocations in superconductors. *Physical Review Letters*, 24(19):1055, 1970.

[72] V. I. Alshits, A. Shtolberg, and V. L. Indenbom. Stationary kink motion in secondary peierls relief. *Physica Status Solidi B-Basic Research*, 50(1):59, 1972.

[73] K. L. Johnson and J. A. Greenwood. An adhesion map for the contact of elastic spheres. *Journal of Colloid and Interface Science*, 192(2):326–333, 1997.

[74] S. E. Babcock and R. W. Balluffi. Secondary grain-boundary dislocation-structures in gold and silver (001) twist boundaries revisited. *Philosophical Magazine a-Physics of Condensed Matter Structure Defects and Mechanical Properties*, 55(5):643–653, 1987.

[75] T. Schober and R. W. Balluffi. Quantitative observation of misfit dislocation arrays in low and high angle twist grain boundaries. *Philosophical Magazine*, 21(169):109, 1970.

[76] T. Y. Tan, S. L. Sass, and R. W. Balluffi. Detection of periodic structure of high-angle twist boundaries .2. high-resolution electron-microscopy study. *Philosophical Magazine*, 31(3):575–585, 1975.

[77] C. F. McFadden and A. J. Gellman. Metallic friction: the effect of molecular adsorbates. *Surface Science*, 409(2):171–182, 1998.

[78] J. S. Ko and A. J. Gellman. Friction anisotropy at ni(100)/ni(100) interfaces. *Langmuir*, 16(22):8343–8351, 2000.

[79] B. M. Dekoven and P. L. Hagans. Friction studies of clean and oxygen exposed fe surfaces in ultrahigh-vacuum. *Journal of Vacuum Science and Technology a-Vacuum Surfaces and Films*, 8(3):2393–2400, 1990. Part 2.

[80] J. Greenwood and J. H. Tripp. Elastic contact of rough spheres. *Journal of Applied Mechanics*, 34(1):153, 1967.

[81] J. Greenwood and J. Williams. Contact of nominally flat surfaces. *Proceedings of the Royal Society of London Series a-Mathematical and Physical Sciences*, 295(1442):300, 1966.

[82] R. W. Carpick and M. Salmeron. Scratching the surface: Fundamental investigations of tribology with atomic force microscopy. *Chemical Reviews*, 97(4):1163–1194, 1997.

[83] Udo D. Schwarz, Oliver Zwörner, Peter Köster, and Roland Wiesendanger. Quantitative analysis of the frictional properties of solid materials at low loads. i. carbon compounds. *Phys. Rev. B*, 56(11):6987–6996, Sep 1997.

[84] A. Berman, C. Drummond, and J. N. Israelachvili. *Tribology Letters*, 4:95, 1998.

[85] M. L. Gee, P. M. McGuiggan, J. N. Israelachvili, and A. M. Homola. Liquid to solid-like transitions of molecularly thin-films under shear. *Journal of Chemical Physics*, 93(3):1895–1906, 1990.

[86] J. Israelachvili, N. Maeda, K. J. Rosenberg, and M. Akbulut. Effects of sub-fingstrom (pico-scale) structure of surfaces on adhesion, friction, and bulk mechanical properties. *Journal of Materials Research*, 20(8):1952–1972, 2005.

[87] L. Bureau, C. Caroli, and T. Baumberger. Frictional dissipation and interfacial glass transition of polymeric solids. *Physical Review Letters*, 97(22), 2006.

[88] B. Joos and M. S. Duesbery. The peierls stress of dislocations: An analytic formula. *Physical Review Letters*, 78(2):266–269, 1997.

[89] A. I. Landau. The effect of dislocation inertia on the thermally activated low-temperature plasticity of materials .1. theory. *Physica Status Solidi a-Applied Research*, 61(2):555–563, 1980.

[90] D. J. Dingley and R. C. Pond. Interaction of crystal dislocations with grain-boundaries. *Acta Metallurgica*, 27(4):667–682, 1979.

[91] T. Gyalog and H. Thomas. Friction between atomically flat surfaces. *Europhysics Letters*, 37(3):195–200, 1997.

[92] M. Hirano, K. Shinjo, R. Kaneko, and Y. Murata. Anisotropy of frictional forces in muscovite mica. *Physical Review Letters*, 67(19):2642–2645, 1991.

[93] Y. Qi, Y. T. Cheng, T. Cagin, and W. A. Goddard. Friction anisotropy at ni(100)/(100) interfaces: Molecular dynamics studies. *Physical Review B*, 66(8), 2002.

[94] S. Aubry and P. Y. Ledaeron. The discrete frenkel-kontorova model and its extensions .1. exact results for the ground-states. *Physica D*, 8(3):381–422, 1983.

[95] K. Shinjo and M. Hirano. Dynamics of friction - superlubric state. *Surface Science*, 283(1-3):473–478, 1993.

[96] M. Hirano, K. Shinjo, R. Kaneko, and Y. Murata. Observation of superlubricity by scanning tunneling microscopy. *Physical Review Letters*, 78(8):1448–1451, 1997.

[97] R. H. Telling and M. I. Heggie. Stacking fault and dislocation glide on the basal plane of graphite. *Philos. Mag. Lett.*, 83(7):411–421, 2003.

[98] D. E. Soule and C. W. Nezbeda. Direct basal-plane shear in single-crystal graphite. *Journal of Applied Physics*, 39(11):5122, 1968.

[99] F. Ernst. Metal-oxide interfaces. *Materials Science and Engineering R-Reports*, 14(3):97–156, 1995.

[100] R. C. Pond and D. A. Smith. On the relative rotation of unconstrained polycrystals. *Scripta Metallurgica*, 11(1):77–79, 1977.

[101] Yinon Ashkenazy, R. S. Averback, and Karsten Albe. Nanocluster rotation on pt surfaces: Twist boundaries. *Physical Review B*, 64(20):205409, 2001.

[102] J. Y. Park, D. F. Ogletree, M. Salmeron, R. A. Ribeiro, P. C. Canfield, C. J. Jenks, and P. A. Thiel. High frictional anisotropy of periodic and aperiodic directions on a quasicrystal surface. *Science*, 309(5739):1354–1356, 2005.

[103] P. Gumbsch and H. Gao. Dislocations faster than the speed of sound. *Science*, 283(5404):965–968, 1999.

[104] M. I. Kaganov, Kravchen.Vy, and V. D. Natsik. Braking of dislocations in metals by electrons. *Uspekhi Fizicheskikh Nauk*, 111(4):655–682, 1973.

[105] N. P. Kobelev and Y. M. Soifer. Electronic damping of dislocations in lead. *Physica Status Solidi a-Applied Research*, 50(2):K185–K188, 1978.

[106] S.V. Kamat, J.P. Hirth, and B. Carnahan. In Jr. Barbee, T.W., editor, *MRS Symposia Proceedings*, volume 103 of *Multilayers: Synthesis, Properties, Nonelectronic Applications*, page 55, Pittsburgh, 1988.

[107] W. Mader. *Mater. Res. Soc. Sym. Proc.*, 82:403, 1987.

[108] W. Mader and D. Knauss. Equilibrium position of misfit dislocations at planar interfaces. *Acta Metallurgica et Materialia*, 40(Supplement 1):S207–S215, 1992.

[109] M. Kato and T. Mori. Internal friction of copper bicrystals with [001] twist boundaries. *Philos. Mag. A*, 68(5):939–949, 1993.

[110] J. S. Koehler. The nature of work-hardening. *Physical Review*, 86(1):52, 1952.

[111] F. C. Frank and W. T. Read. In *Symposium on Plastic Deformation of Crystalline Solids*, page 44, Carnegie Institute of Technology, Pittsburgh, 1950.

[112] Y. Enomoto and D. Tabor. The frictional anisotropy of diamond. *Proceedings of the Royal Society of London Series a-Mathematical Physical and Engineering Sciences*, 373(1755):405–417, 1981.

[113] C. M. Mancinelli and A. J. Gellman. Friction anisotropy at pd(100)/pd(100) interfaces. *Langmuir*, 20(5):1680–1687, 2004.

[114] P. M. McGuiggan and J. N. Israelachvili. Adhesion and short-range forces between surfaces 2 effects of surface lattice mismatch. *Journal of Materials Research*, 5(10):2232–2243, 1990.

[115] H. H. Gatzen and M. Beck. Investigations on the friction force anisotropy of the silicon lattice. *Wear*, 254(11):1122–1126, 2003.

[116] P. E. Sheehan and C. M. Lieber. Nanotribology and nanofabrication of moo3 structures by atomic force microscopy. *Science*, 272(5265):1158–1161, 1996.

[117] D. J. Diestler, E. Rajasekaran, and X. C. Zeng. Static frictional forces at crystalline interfaces. *Journal of Physical Chemistry B*, 101(25):4992–4997, 1997.

[118] I. L. Singer. Friction and energy-dissipation at the atomic-scale - a review. *Journal of Vacuum Science and Technology a-Vacuum Surfaces and Films*, 12(5):2605–2616, 1994.

[119] T. W. Scharf and I. L. Singer. Role of third bodies in friction behavior of diamond-like nanocomposite coatings studied by in situ tribometry. *Tribology Transactions*, 45(3):363–371, 2002.

[120] I. L. Singer, S. D. Dvorak, K. J. Wahl, and T. W. Scharf. Role of third bodies in friction and wear of protective coatings. *Journal of Vacuum Science and Technology A*, 21(5):S232–S240, 2003. Suppl. S.

[121] J. M. Martin, T. Le Mogne, M. Boehm, and C. Grossiord. Tribochemistry in the analytical uhv tribometer. *Tribology International*, 32(11):617–626, 1999.

[122] S. Fujisawa and T. Kizuka. Lateral displacement of an afm tip observed by in-situ tem/afm combined microscopy: The effect of the friction in afm. *Tribology Letters*, 15(2):163–168, 2003.

[123] A. M. Minor, S. A. Syed Asif, S. Zhiwei, E. A. Stach, E. Cyrankowski, T. Wyrobek, and O. L. Warren. A new view of the onset of plasticity during the nanoindentation of aluminum. *Nature Materials*, 5(9):697–702, 2006.

[124] M. W. Larsson, L. R. Wallenberg, A. I. Persson, and L. Samuelson. Probing of individual semiconductor nanowhiskers by tem-stm. *Microscopy and Microanalysis*, 10(1):41–46, 2004.

[125] J. Cumings and A. Zettl. Low-friction nanoscale linear bearing realized from multiwall carbon nanotubes. *Science*, 289(5479):602–604, 2000.

[126] T. Kuzumaki, H. Sawada, H. Ichinose, Y. Horiike, and T. Kizuka. Selective processing of individual carbon nanotubes using dual-nanomanipulator installed in transmission electron microscope. *Applied Physics Letters*, 79(27):4580–4582, 2001.

[127] M. Sveningsson, K. Hansen, K. Svensson, E. Olsson, and E. E. B. Campbell. Quantifying temperature-enhanced electron field emission from individual carbon nanotubes. *Physical Review B*, 72(8), 2005. 085429.

[128] J. Dundurs and T. Mura. Interaction between an edge dislocation and a circular inclusion. *Journal of the Mechanics and Physics of Solids*, 12(3):177–189, 1964.

[129] J. Dundurs and Spendeck.Gp. Behavior of an edge dislocation near a bimetallic interface. *Journal of Applied Physics*, 36(10):3353, 1965.

[130] O. Rohr. Bismuth - the new ecologically green metal for modern lubricating engineering. *Industrial Lubrication and Tribology*, 54(4):153–164, 2002.

[131] Y. B. Zhao, Z. J. Zhang, and H. X. Dang. A simple way to prepare bismuth nanoparticles. *Materials Letters*, 58(5):790–793, 2004.

[132] J. F. Zhou, Z. S. Wu, Z. J. Zhang, W. M. Liu, and Q. J. Xue. Tribological behavior and lubricating mechanism of cu nanoparticles in oil. *Tribology Letters*, 8(4):213–218, 2000.

[133] V. Rodrigues, T. Fuhrer, and D. Ugarte. Signature of atomic structure in the quantum conductance of gold nanowires. *Physical Review Letters*, 85(19):4124–4127, 2000.

[134] G. Rubio, N. Agrait, and S. Vieira. Atomic-sized metallic contacts: Mechanical properties and electronic transport. *Physical Review Letters*, 76(13):2302–2305, 1996.

[135] T. Kizuka, K. Yamada, S. Deguchi, M. Naruse, and N. Tanaka. Cross-sectional time-resolved high-resolution transmission electron microscopy of atomic-scale contact and noncontact-type scannings on gold surfaces. *Physical Review B*, 55(12):R7398–R7401, 1997.

[136] R. Holm. *Electric Contacts Handbook*. Springer-Verlag, Berlin, 1958.

[137] D. W. Pashley, M. H. Jacobs, M. J. Stowell, and T. J. Law. Growth + structure of gold + silver deposits formed by evaporation inside electron microscope. *Philosophical Magazine*, 10(103):127, 1964.

[138] F. M. Kimock and B. J. Knapp. Commercial applications of ion-beam deposited diamond-like carbon (dlc) coatings. *Surface and Coatings Technology*, 56(3):273–279, 1993.

[139] S. Veprek. The search for novel, superhard materials. *Journal of Vacuum Science and Technology A*, 17(5):2401–2420, 1999.

[140] A. Erdemir, O. L. Eryilmaz, and G. Fenske. Synthesis of diamondlike carbon films with superlow friction and wear properties. *Journal of Vacuum Science and Technology A*, 18(4):1987–1992, 2000. Part 2.

[141] C. Donnet and A. Erdemir. Solid lubricant coatings: recent developments and future trends. *Tribology Letters*, 17(3):389–397, 2004.

[142] C. Donnet and A. Grill. Friction control of diamond-like carbon coatings. *Surface and Coatings Technology*, 94-5(1-3):456–462, 1997.

[143] C. A. Freyman, Y. F. Chen, and Y. W. Chung. Synthesis of carbon films with ultra-low friction in dry and humid air. *Surface and Coatings Technology*, 201(1-2):164–167, 2006.

[144] Y. Liu, A. Erdemir, and E. I. Meletis. An investigation of the relationship between graphitization and frictional behavior of dlc coatings. *Surface Coatings Technology*, 86-7(1-3):564–568, 1996. Part 2.

[145] A. Erdemir and G. R. Fenske. Tribological performance of diamond and diamondlike carbon films at elevated temperatures. *Tribology Transactions*, 39(4):787–794, 1996.

[146] H. I. Kim and J. R. Lince. Direct visualization of sliding-induced tribofilm on au/mos2 nanocomposite coatings by c-afm. *Tribology Letters*, 25:Online First, 2007.